Study of Methylammonium Lead Triiodide Intrinsic Stability and Solid-Solution behaviour in Mixed Halide Perovskite Systems

by

Abdelrahman Mostafa Mohamed Sanad Askar

A thesis submitted in partial fulfillment of the requirements for the degree of

Master of Science

in

Microsystems and Nanodevices

Department of Electrical and Computer Engineering

University of Alberta

Abstract

Over the last nine years, a new class of materials named lead halide perovskite has made a paradigm shift in the field of optoelectronic solution-processable low-cost and high efficiency devices, with outstanding accomplishments especially in the ever growing field of renewable solar energy harvesting. With current state-of-the-art 22.7% efficiency for lab-scale perovskite solar cells, the expectations are high with the potentials of this "magic" material system in being a real driving force for next-generation low-cost and high-efficiency photovoltaics technology.

In order to make maximum use of any newly introduced material systems such as halide perovskites for real life applications, it is essential to carry out fundamental studies which enable better in-depth understanding of the basic material electrical, optical, thermal, mechanical, etc. properties. This understanding is crucial for such a new technology to be able to advance further into actual products in the market.

In this work, we tried to shed light on fundamental questions pertaining to important lead halide perovskite material characteristics. We studied the stability of methylammonium lead iodide ($MAPbI_3$) through identifying all possible decomposition products of $MAPbI_3$, which each has a unique fingerprint. Through systematic investigation of potential decomposition pathways under different conditions of humidity and/or heat,

we identified a comprehensive understanding of the intrinsic stability of $MAPbI_3$. We hypothesized that the lower stability observed in films is mainly due to the preparation protocols, and that the $MAPbI_3$ is more resilient than what was previously thought.

Also, we studied two of the main lead halide perovskite materials which are routinely used nowadays in the realization of high-efficiency and relatively-stable perovskite solar cells, namely methylamonium and formamidinium lead mixed halide perovskites. We explored the potential of a new synthetic route (mechanochemical synthesis) to prepare these materials with definitive control over stoichiometry. It has been reported earlier in the literature that these systems suffer from halide phase segregation, so we investigated this through adopting a suite of advanced characterization with atomic-scale probing capabilities which confirmed that these system behave like a solid-solution with atomic scale halide mixing.

The significance of the results presented here is vital for future research in this rapidly growing field as these results answer fundamental questions related to the perovskite materials intrinsic properties as well as elaborating on new up-scalable synthesis techniques.

Preface

In Chapter 1, the solar cell results presented are the sole work of Johannes Schlipf and colleagues at Technical University of Munich (TUM), my contribution was the synthesis and quality optimization of methylamonium lead iodide/bromide single crystals used for the fabrication of perovskite solar cells. This work has been published as: Top-Down Approaches Towards Single Crystal Perovskite Solar Cells, Johannes Schlipf, ***Abdelrahman M. Askar***, Florian Pantle, Benjamin D. Wiltshire, Anton Sura, Peter Schneider, Linus Huber, Karthik Shankar & Peter Müller-Buschbaum. *Scientific Reports* **8**, Article number: 4906 (**2018**).

The work presented in Chapters 2 & 3 are the output of a collaboration with Prof. Vladimir Michaelis and his group at the University of Alberta - Department of Chemistry (The Michaelis solid state NMR research group). All solid state NMR spectroscopy results have been exclusively acquired and analysed by Prof. Michaelis group. I was involved in the discussions of the results. Other than the NMR spectroscopy part, I was in charge of all the synthesis and all the experiments. In briefly, I have did all the synthesis of perovskite materials including single crystals, mixed halide perovskites prepared either by solvent synthesis or mechanochemical routes. Also, I run all the XRD measurements and was in charge of all the data analysis and the

same applies for optical measurements. Abhoy Karmakar helped with the Vegard's law analysis for some of the results. I have run all the stability experiments presented in Chapter 2 with help from Dr. Guy Bernard in some of the experiments.

Results presented in chapter 2 are parts of an extended study published as: Multinuclear Magnetic Resonance Tracking of Hydro, Thermal, and Hydrothermal Decomposition of $CH_3NH_3PbI_3$. ***Abdelrahman M. Askar***, Guy M. Bernard, Benjamin Wiltshire, Karthik Shankar, and Vladimir K. Michaelis, *J. Phys. Chem. C*, **2017**, 121 (2), 1013-1024.

Results presented in Chapter 3 are published with extended discussions as:

1. Mechanochemical Synthesis of Methylammonium Lead Mixed–Halide Perovskites: Unraveling the Solid-Solution Behavior Using Solid-State NMR. Abhoy Karmakar, ***Abdelrahman M Askar***, Guy M Bernard, Victor V Terskikh, Michelle Ha, Sahil Patel, Karthik Shankar, Vladimir K Michaelis, *Chem. Mater.*, **2018**, 30 (7), 2309–2321

2. Composition-Tunable Formamidinium Lead Mixed Halide Perovskites via Solvent-Free Mechanochemical Synthesis: Decoding the Pb Environments Using Solid-State NMR Spectroscopy. ***Abdelrahman M. Askar***, Abhoy Karmakar, Guy M. Bernard, Michelle Ha, Victor V. Terskikh, Benjamin D. Wiltshire, Sahil Patel, Jonathan Fleet, Karthik Shankar, and Vladimir K. Michaelis, *J. Phys. Chem. Lett.*, **2018**, 9 (10), 2671–2677

I actively participated and was involved in all discussions of the results presented in the above mentioned three papers, except for those related to the fine details of the NMR spectroscopy experiments and results not directly related to the discussions highlighted in this thesis. I was not involved in the acquisition of the NMR spectra, but rather

took part in the discussions. I was responsible for the write-up of all experimental and discussion sections which I was responsible for during the collaborative work. I helped also in the preparation of the introductions and background sections of the papers. I took part in the review process of the papers till published.

To my Family,

Contents

List of Tables

List of Figures

Chapter 1

Introduction

The quest for low-cost and high-efficiency renewable energy sources never stops. Solar energy harvesting stands out among other renewable technologies holding the promise to provide all our energy needs for today and tomorrow. Well-established silicon photovoltaics technology offers a reasonably priced solar cell solution nowadays with advances in manufacturing and large scale production. Nevertheless, it is highly desirable to find even lower-cost technologies with longer lifetimes and higher efficiencies.

Among the emerging technologies that have been under research and development for sometime now are organic photovoltaics,[3,4] dye-sensitized,[5–7] and quantum-dot solar cells.[8,9] Despite the intensive research efforts made in these technologies so far, all of these emerging technologies fall behind in efficiency even for small lab-scale solar cells when compared to silicon counterparts. In 2009, a whole new class of materials was proposed to be a potential competitor for next-generation low-cost and truly high-efficiency solar cells. Starting with reported power conversion efficiency (PCE) of 3.9% in 2009, solar cells based on lead halide perovskite (LHP) materials ramped quickly in efficiency within a few years only to achieve record PCE of 22.7% in 2017, which is comparable to best single junction monocrystalline silicon solar cell.[10]

So, should we expect to see perovskite solar cells (PSCs) on top of our roofs very soon? Maybe! Despite the remarkable achievements PSCs have made on efficiency scale, a few questions to be answered and some challenges to be solved by the research

community before we can see PSCs entering the market. On top of these questions is the stability concerns for PSCs. While vendors of silicon photovoltaics offer between 30-50 years of warranty for silicon solar cell modules, earlier PSCs literally died within few hours to few days of operation, nevertheless, lately the stability of PSCs have enhanced significantly with reports of more than a year with reasonable efficiency maintained.[11,12] This clearly shows how the field of PSCs is quickly progressing thanks to advanced research efforts worldwide. The next big challenge is large-scale manufacturing of high-efficiency (more than 22% PCE) of PSCs. Only lab-scale (less than 1 cm^2) PSCs have demonstrated record efficiencies so far, with significant drop in the efficiency when fabricating perovskite modules of reasonable effective cell area. Last but not least, the toxicity of lead in PSCs and the environmental considerations related to that. Although considerable work has been done to look for lead-free alternatives for PSCs, still record-high PCEs are only achieved with Pb-containing PSCs. Overcoming above-mentioned challenges would no doubt pave the way for PSCs into markets in the near future.

In this chapter, we will give an overview of the electrical & optical properties of LHP materials that are relevant to solar cell applications. Also, the perovskite single crystals (SCs) will be introduced as part of the work done through the course of this thesis. Towards the end of this chapter, the main focus of this thesis is given, which is discussed in details in Chapters 2 & 3.

1.1 Lead-halide perovskites: A revisited material system with unprecedented intrinsic optoelectronic properties

Originally, ***Perovskite*** is the name for one of the crystal structures and is given to any material that adopts the same crystal structure as for $CaTiO_3$, with a general chemical formula ABX_3. The mineral was discovered in the Ural Mountains of Russia by Gustav Rose in 1839 and is named after Russian mineralogist Lev Perovski (1792–1856). Traditionally, most of the perovskites studied till recently were oxide-based ones, nev-

ertheless, also halide-based perovskites were as well investigated with reports dating back to 1980s and even earlier.[13–15] It was not until 2009 when methylamonium lead tri-iodide ($MAPbI_3$) was applied as the light harvesting layer in a dye-sensitized solar cell structure which sparked the renewed interest in this material system since then.[16]

Numerous derivatives of the parent compound ($MAPbI_3$) have been studied so far, through replacing/mixing each one of the elemental constituents of $MAPbI_3$. For instance, MA^+ cations have been replaced/mixed with either organic and/or inorganic cations such as formamidinium (FA^+), guanidinium, K, Cs, and Rb. The same for lead which has been replaced/mixed with different elements; mainly Sn and Sb. For the halide component; all Cl, Br, and I have been consistently investigated. Although $MAPbI_3$ adopts 3D crystal structure, some derivatives adopt 2D, and 0D crystal structures which shows the versatility and flexibility of this material system.

In the following, we will focus only on $MAPbX_3$ and $FAPbX_3$ (X: Cl, Br, and I) which have been studied throughout the course of this thesis.

1.1.1 Distinct Electrical & Optical Properties of LHPs

One of the most amazing and compelling attributes of LHPs that they combined a suite of optoelectronic properties that make them in theory an ideal choice for low-cost and high-efficiency next-generation solar cells. This comprises of tunable direct bandgap, long charge carrier diffusion lengths, high electron and hole mobilities, extended carrier lifetimes, low exciton binding energy, high photoluminescence quantum yield and an extraordinarily-low trap-state density.[1] These properties combined are essential for active solar cell materials to achieve high-efficiency performance. In addition, LHPs are solution-processable which is another striking attribute of this material system because it has been always the case that solution-processable materials suffer from some degree of disorder limiting their performance; nevertheless, LHPs showed a sort of immunity to these disorders and achieved record performance along the years of

[1] An exhaustive review of these properties can be found in this paper: The Electrical and Optical Properties of Organometal Halide Perovskites Relevant to Optoelectronic Performance, Valerio Adinolfi, Wei Peng, Grant Walters, Osman M. Bakr, Edward H. Sargent. *Advanced Materials*, **2018**, 30 (1), 1700764

research and development.[17–19] It is worth mentioning here that both electrical and optical properties of LHP materials can differ significantly based on the quality of the perovskite material being tested (thin films or single crystals) and the method used to extract these figures. Over the years, the quality of perovskite materials (especially thin films used in solar cells) got improved substantially, and so are the optoelectronic properties of these materials. Next we will highlight some of these characteristics.

Starting with carrier diffusion lengths, reported numbers kept increasing from well below 1 µm to more than 10 µm for perovskite thin films with improved film qualities and larger grain sizes. Also, extracted charge carrier mobilities exceeding 10 $cm^2V^{-1}s^{-1}$ have been achieved for perovskite films, which is remarkable for a solution-processable material. In addition, carrier lifetimes in excess of 1 µs have been measured based on photoluminescence decay. Another attribute is the trap density which is a direct indication of the defects in the material. There has been a dispute regarding the actual values, but numbers around 10^{12} - 10^{13} cm^{-3} have been reported, which is impressive for a solution-processable material. Finally, exciton binding energies as low as 20-30 meV were measured at room temperature for perovskite thin films, which is striking because such low binding energies are similar to those reported for inorganic semiconductors such as silicon.

1.2 Perovskite Single Crystals: Optimum Material Quality & Platform for Optoelectronic Applications

In order to extract the intrinsic properties of a semiconductor material such as carrier lifetime, diffusion length, etc., it is highly desirable to obtain single crystals of the material, which are free from grain boundaries dominating in thin films and have minimum trap-state density possible. The successful synthesis of LHP single crystals enabled in-depth understanding of the intriguing properties of these materials and exceptional figures of merit were extracted for these properties, which motivated the research community to work extensively in order to achieve perovskite thin films with

qualities that approach those for single crystals.[20]

Over the last four years, many techniques have been proposed to synthesize perovskite single crystals with mm to cm scale, with a current library of tens of those single crystals available for fundamentals studies and innovative applications.[21–23] (see Figure 1.1)

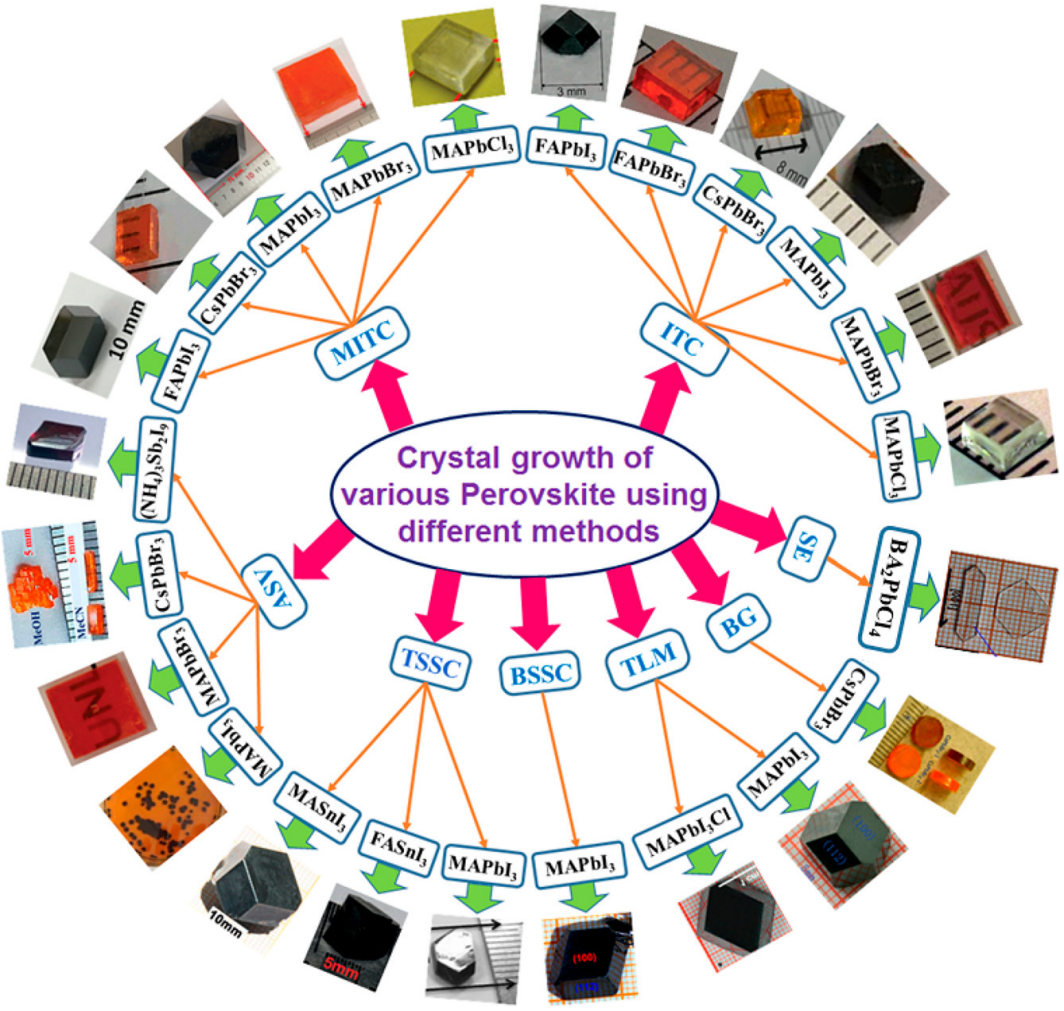

Figure 1.1: Illustration of different halide based perovskites crystals grown by various techniques. Reproduced with permission from ref 21. Copyright American Chemical Society

Over the course of this work, a method called Inverse Temperature Crystallization (ITC)[24,25] had been adopted due to its simplicity to synthesize MA/FAPbX$_3$ single crystals with mm sizes (see Figure 1.2). All MAPbX$_3$ (X: Cl, Br, and I) as well as FAPbX$_3$ (X: Br and I) SCs were synthesized using ITC (Experimental details are available in Appendix A & B.) As a proof-of-concept, MAPbBr$_3$ and MAPbI$_3$ were tested for fabricating solar cells. The synthesis of the SCs was optimized as part of this

thesis to obtain the highest quality SCs with reasonable sizes to facilitate the realization of solar cell devices. All work following SC synthesis has been done exclusively by our collaborators at Technical University of Munich (TUM) and this work has been published in Scientific Reports.[26] An example of solar cell characteristics for $MAPbX_3$ SC-based device is shown in Figure 1.3.

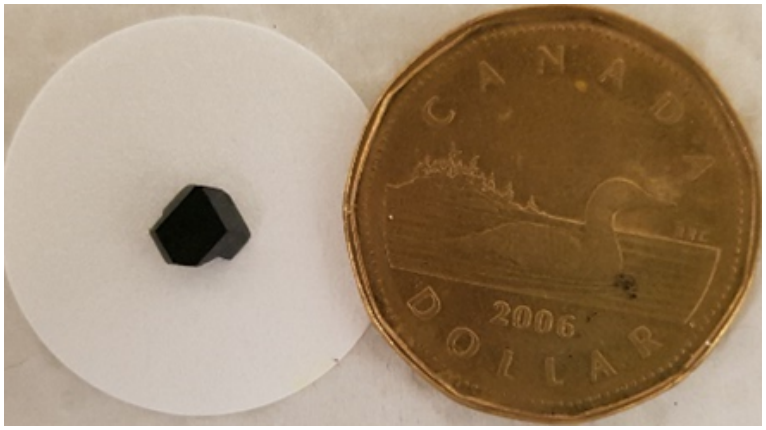

Figure 1.2: Example of $MAPbI_3$ SC synthesized through ITC method.

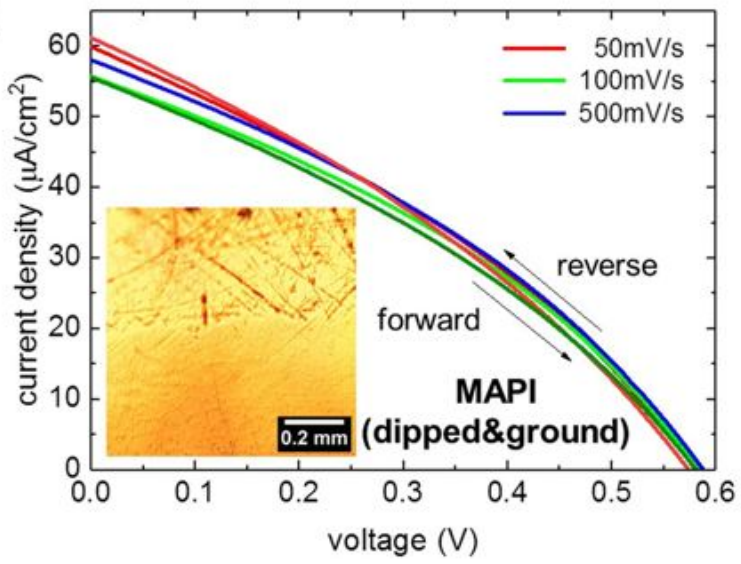

Figure 1.3: JV curves of a device fabricated from a dipped and ground $MAPbI_3$ crystal with bias sweep in forward and reverse direction at various speeds hardly exhibit any hysteresis. In the optical microscopy image (inset) shows a crystal surface after coarse manual grinding (upper part) as opposed to machined grinding (lower part). Reproduced with permission from Ref 26. Copyright Nature Publishing Group.

Thesis Focus

The focus of this thesis is two-fold; first one is to understand the intrinsic stability properties of $MAPbI_3$ and its degradation mechanisms irrespective of the material preparation techniques. This is covered in detail in Chapter 2. Second, we wanted to understand the true nature of halide mixing at atomic-level in mixed halide perovskite materials and to investigate the full potential of applying mechanochemical synthesis technique in preparing this exciting category of materials which is relevant to high-efficiency and stable various optoelectronic perovskite-based devices. This is covered in Chapter 3 with emphasis on 2 systems; namely, $MAPbX_3$ and $FAPbX_3$. Finally, we give a conclusion and an outlook for potential future research directions.

Chapter 2

Tracking of Hydro, Thermal, and Hydrothermal Decomposition of $CH_3NH_3PbI_3$

In this chapter, the work done on studying the intrinsic stability of $CH_3NH_3PbI_3$ along with tracking the decomposition pathways under different environments is presented.[1]

2.1 Abstract

An NMR investigation of methylammonium lead iodide, the leading member of the hybrid organic−inorganic perovskite class of materials, and of its putative decomposition products as a result of exposure to heat and humidity, has been undertaken. We show that the ^{207}Pb NMR spectra of the compound of interest and of the proposed lead containing decomposition products, $CH_3NH_3PbI_3{\cdot}H_2O$, $(CH_3NH_3)_4PbI_6{\cdot}2H_2O$, and PbI_2, have distinctive chemical shifts spanning over 1400 ppm, making ^{207}Pb NMR an ideal tool for investigating this material. As reported in many investigations of $CH_3NH_3PbI_3$ on films, the bulk material hydrates in the presence of high relative humidity (approx-

[1] An extended version of this chapter has been published as: Abdelrahman M. Askar, Guy M. Bernard, Benjamin Wiltshire, Karthik Shankar, and Vladimir K. Michaelis, *J. Phys. Chem. C*, **2017**, 121 (2), 1013-1024

imately 80%), yielding the monohydrated perovskite $CH_3NH_3PbI_3{\cdot}H_2O$. This reaction is reversible by heating the sample to 341 K. We show that neither $(CH_3NH_3)_4PbI_6{\cdot}2H_2O$ nor PbI_2 is observed as a decomposition product and that, in contrast to many studies on $CH_3NH_3PbI_3$ films, the bulk material does not decompose or degrade beyond $CH_3NH_3PbI_3{\cdot}H_2O$ upon prolonged exposure to humidity at ambient temperature. However, exposing $CH_3NH_3PbI_3$ concurrently to heat and humidity, or directly exposing it to liquid water, leads to the irreversible formation of PbI_2. In spite of its absence among the decomposition products, the response of $(CH_3NH_3)_4PbI_6{\cdot}2H_2O$ to heat was also investigated. It is stable at temperatures below 336 K but then rapidly dehydrates, first to $CH_3NH_3PbI_3{\cdot}H_2O$ and then to $CH_3NH_3PbI_3$. The higher stability of the bulk material as reported here is a promising advance, since stability is a major concern in the development of commercial applications for this material.

2.2 Introduction

The sensitivity of $CH_3NH_3PbI_3$ ($MAPbI_3$) to moisture was discovered in the early stages of PSC development, where exposure of the PSC to a relative humidity (RH) of 35% led to a more than 50% degradation in the PCE of $MAPbI_3$ solar cells within a few days. *Leguy et al.* proposed the following equation to describe the reaction of $MAPbI_3$ with humidity:[27]

$$4MAPbI_3 + 4H_2O \rightleftharpoons 4[MAPbI_3{\cdot}H_2O] \rightleftharpoons (MA)_4PbI_6{\cdot}2H_2O + PbI_2 + 2H_2O \quad \text{..... Eq. 1}$$

These authors suggested that an excess of water may lead to an irreversible degradation product:

$$(MA)_4PbI_6{\cdot}2H_2O \xrightarrow{H_2O} 4MAI + PbI_2 + 2H_2O \quad \text{..... Eq. 2}$$

Interestingly, recent studies showed a counter effect, where preparation of the PSC under moderate RH improved PCE.[28–31]

Elucidating the exact degradation mechanisms and routes upon exposure of perovskite materials (especially $MAPbI_3$) to humidity has been the focus of many recent studies,

both experimentally and theoretically.[11,29,32–38] Different analytical techniques have been applied in these investigations, including in situ and time-resolved powder and single-crystal X-ray diffraction (XRD),[28,39–41] optical absorption,[28] and spectroscopic ellipsometry.[42]

Due to the different humidity conditions being examined (e.g., with/without light, with/without heat, varying humidity levels, etc.) as well as the different ways the perovskite films are prepared in these studies and the varying structures of the devices under investigation, the results are ambiguous, and different degradation pathways of the perovskite materials have been proposed.

For instance, earlier studies suggested that solar cell performance degraded as a consequence of the slow decomposition of $MAPbI_3$ to PbI_2 in addition to MAI or CH_3NH_2 plus HI.[43–46] Recently, an intermediate byproduct of $MAPbI_3$ decomposition, $(MA)_4PbI_6 \cdot 2H_2O$[13] (i.e., the perovskite dihydrate), was identified by Kamat and co-workers[47] after exposure of an $MAPbI_3$ film to high RH(90%) for several days in the dark, but these authors did not observe PbI_2. Using in situ grazing incidence XRD (GIXRD), Kelly et al.[37] noticed the formation of new peaks in the GIXRD pattern during the decomposition of $MAPbI_3$ at high RH (80%); these peaks could not be associated with either $MAPbI_3$ or PbI_2 and thus were attributed to the formation of $(MA)_4PbI_6 \cdot 2H_2O$. The conclusion in these earlier studies of the presence of the perovskite dihydrate was based on comparisons between the XRD pattern of the decomposition product they measured and either the calculated pattern of the dihydrate or the pattern of a synthesized perovskite hydrate, assumed to be the dihydrate. This decomposition product was later confirmed to in fact be the monohydrate perovskite ($CH_3NH_3PbI_3 \cdot H_2O$) by Leguy et al.[27] Other studies have confirmed the formation of the monohydrate as an intermediate decomposition product, but it is unclear whether this is the final decomposition product or whether the formation of the monohydrate is followed by formation of the dihydrate, and finally of PbI_2.[27,33–35,42]

These studies focused mainly on either *in* or *ex situ* investigations of the degradation of the perovskite film, prepared by various techniques such as solution-processing or co-evaporation, with the $MAPbI_3$ as the light harvesting layer in different solar cell architectures (i.e., having the perovskite layer deposited on some electron or hole

transport layer). The varying techniques explain the different conclusions reached by the investigators but unfortunately hinder the determination of the intrinsic interaction mechanisms between the perovskite material and H_2O molecules in a humid environment.

The logic of investigating the material in its operating architecture is indisputable, but a detailed study of the bulk properties of the compounds of interest informs on the ambiguities inherent in the earlier studies and guides future developments. The Kamat group[38] recently published a detailed review of spectroscopic and structural techniques that can be employed to monitor the response of perovskites exposed to moisture.

Here, we report a solid-state ^{207}Pb nuclear magnetic resonance investigation of bulk samples of $MAPbI_3$ and its proposed decomposition products. Solid-state nuclear magnetic resonance (NMR) spectroscopy, which probes the local chemical structure in a nondestructive manner, is ideal to identify changes within molecular and periodic solids that affect the structure, composition, and optoelectronic properties of these next generation photovoltaic materials. ^{207}Pb nuclei have reasonably receptive I = 1/2 nuclear spin, with a moderate resonance frequency (20.92%), a natural abundance of 22.1%, and one of the largest known NMR chemical shift ranges, approximately 17,000 ppm,[48] making it extremely sensitive to subtle changes within the local Pb chemical and coordination environment.[48–50]

In the work presented here, we characterize and highlight the distinct differences between $MAPbI_3$ and the three proposed Pb-based decomposition products occurring as a consequence of exposure of the former to humid or thermal environments, or both, in the dark (Scheme 3.1). Our goal is to elucidate the conditions leading to different decomposition pathways, to identify intermediate and final degradation products, and to investigate conditions under which $MAPbI_3$ may be recovered from these products. We show that solid-state ^{207}Pb NMR spectroscopy is ideally suited to monitor environmental effects on $MAPbI_3$ and its decomposition products. The results of these measurements, performed on bulk samples, are compared to those obtained on thin-film samples.

Scheme 2.1 Degradation Reaction Pathway of $MAPbI_3$ into Three Different Pseudo-Octahedral Pb-I Crystalline Solids

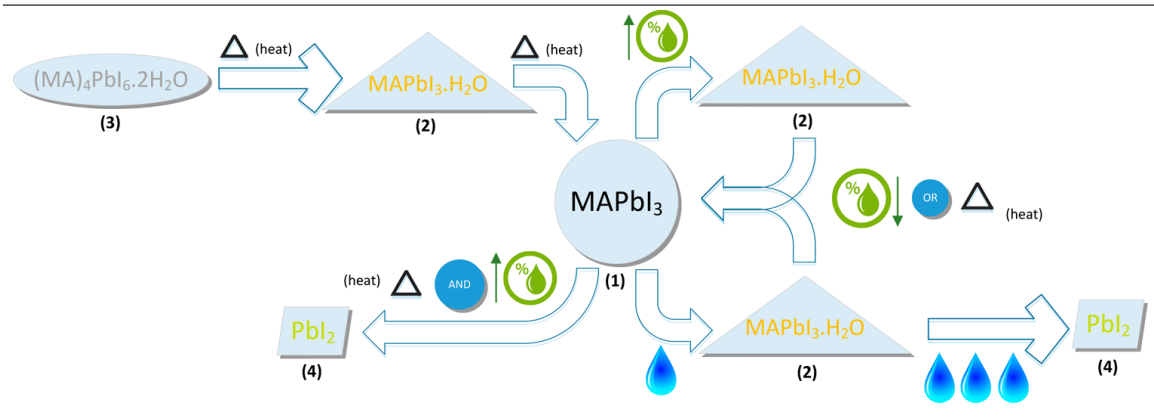

Note: Experimental details are available in Appendix A.

2.3 Results & Discussions

2.3.1 NMR Spectra of $MAPbI_3$ and Related Products

To investigate $MAPbI_3$ and proposed decomposition products resulting from its exposure to varying potential atmospheric conditions, ^{207}Pb NMR spectra of lab-synthesized stationary samples of $MAPbI_3$, $MAPbI_3{\cdot}H_2O$ (i.e., the monohydrate), $(MA)_4PbI_6{\cdot}2H_2O$ (i.e., the dihydrate), and PbI_2 were acquired, as shown in Figure 2.1. These spectra are notable for the distinct chemical shifts of the starting compound and its possible decomposition products. The range of chemical shifts (in excess of 1400 ppm) is a reflection of the sensitivity of the ^{207}Pb nucleus to its local environment and demonstrates the utility of NMR to characterize these types of materials. Dybowski and co-workers[51] reported a similar chemical shift value for PbI_2; values of 1430 and 1423 ppm were recently reported for $MAPbI_3$ by Roiland et al.[52] and by Vela and co-workers,[53] respectively. The slight difference in these chemical shift values compared to our value is probably a reflection of the extreme sensitivity of ^{207}Pb to temperature.

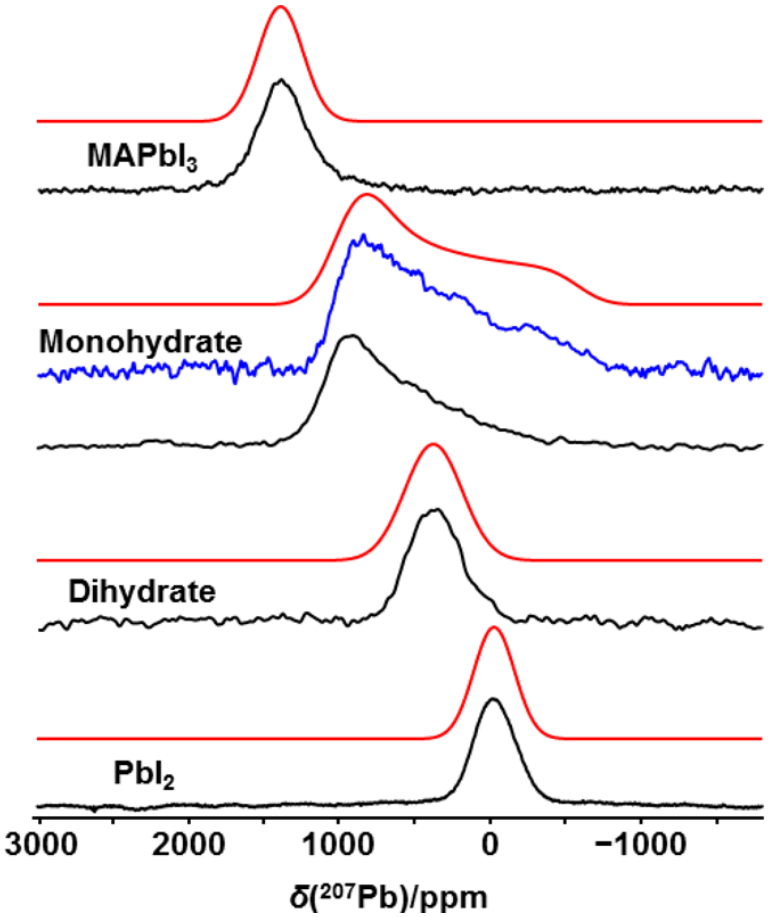

Figure 2.1: Simulated (red traces) and experimental ^{207}Pb NMR spectra of non-spinning samples of $MAPbI_3$, the monohydrate, the dihydrate, and PbI_2, acquired at 294 K at 7.05 T. The blue trace indicates the skyline projection of experimental spectra for the monohydrate acquired with three spectrometer frequency offsets; all other spectra were acquired with a single frequency offset.

2.3.2 Powder X-ray Diffraction.

Figure 2.2 shows experimental XRD patterns obtained in this work. The simulations, based on the reported structures for $MAPbI_3$,[54] PbI_2 (PDF 00-007-0235), the monohydrate,[55] or the dihydrate,[56] confirm that the desired products have been obtained. As for the ^{207}Pb NMR spectra, distinctive powder XRD patterns are obtained for the four compounds.

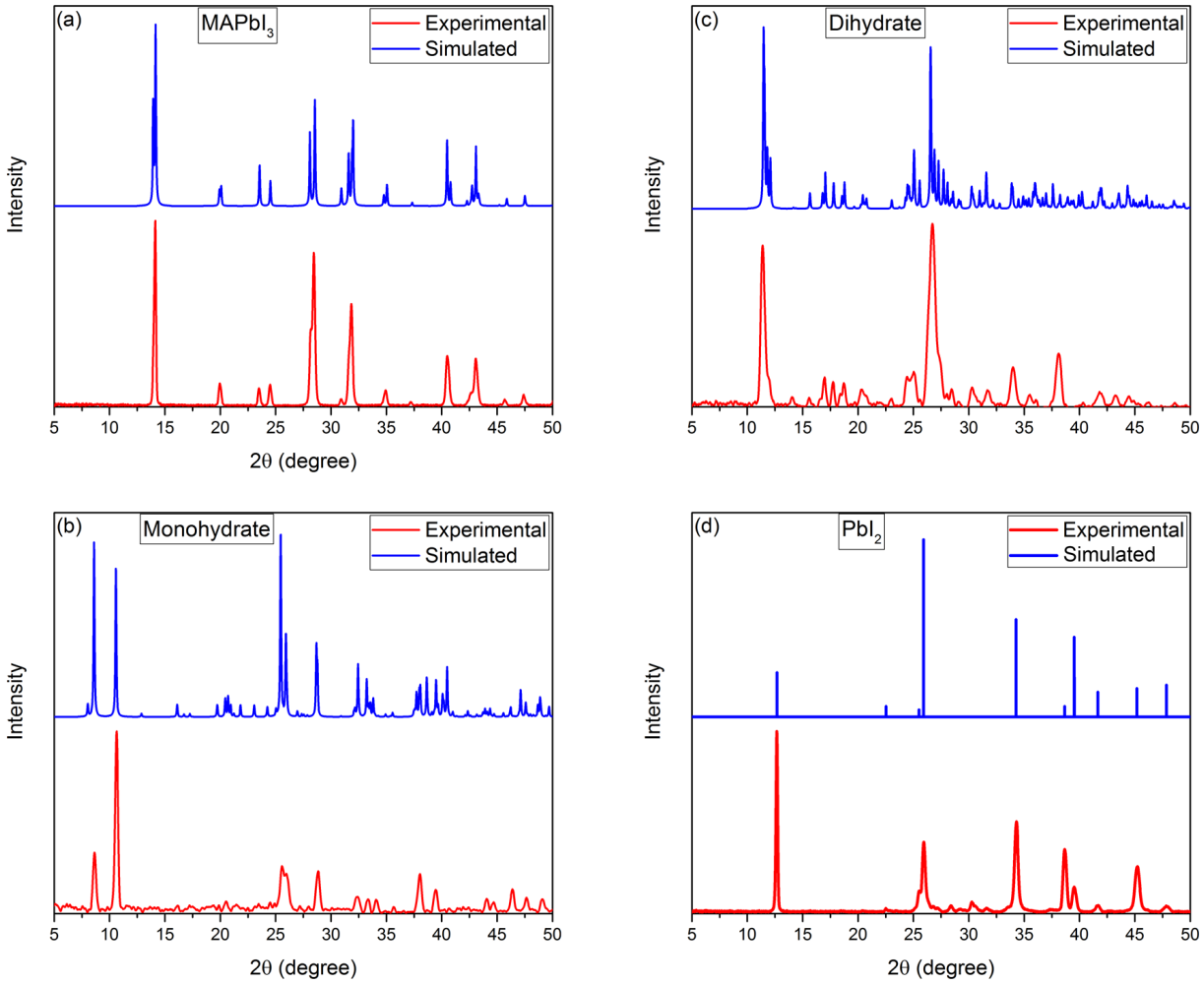

Figure 2.2: Experimental and simulated powder X-ray diffraction patterns for crystalline $MAPbI_3$ (a), the monohydrate (b), the dihydrate (c), and PbI_2

2.3.3 Response of $MAPbI_3$ to Humidity at Ambient Temperature.

To investigate the effect of humidity on $MAPbI_3$, approximately 1.0 g of the sample was placed in a humidity cell operating at room temperature, at approximately 80% RH. In the course of 1 week, the sample turned from the black color of $MAPbI_3$ to a yellow crystalline powder (see Figure A.2). Figure 2.3 illustrates ^{207}Pb NMR spectra of stationary samples extracted from the humidity cell at the indicated times, ranging from 3 h to 3 weeks; a spectrum of $MAPbI_3$ (i.e., t = 0) is included for comparison. These spectra demonstrate that $MAPbI_3$ is quickly affected by humidity; approximately 55% of the total signal has shifted to an asymmetric peak after exposure to 80% RH for 3 h. After 24 h, this peak had grown to 80% of the total intensity, after

3 days only a trace of the peak attributed to $MAPbI_3$ remained, and finally, after 1 week, only the asymmetric peak remained. As seen from the spectrum of the sample collected after 21 days, there were no further changes once the product yielding the asymmetric peak was obtained.

Comparison of the ^{207}Pb NMR spectra shown in the upper traces of Figure 2.3 with those shown in Figure 2.1 indicates that the product of exposure of $MAPbI_3$ to high humidity is the monohydrate, with no indication that any further decomposition occurs.

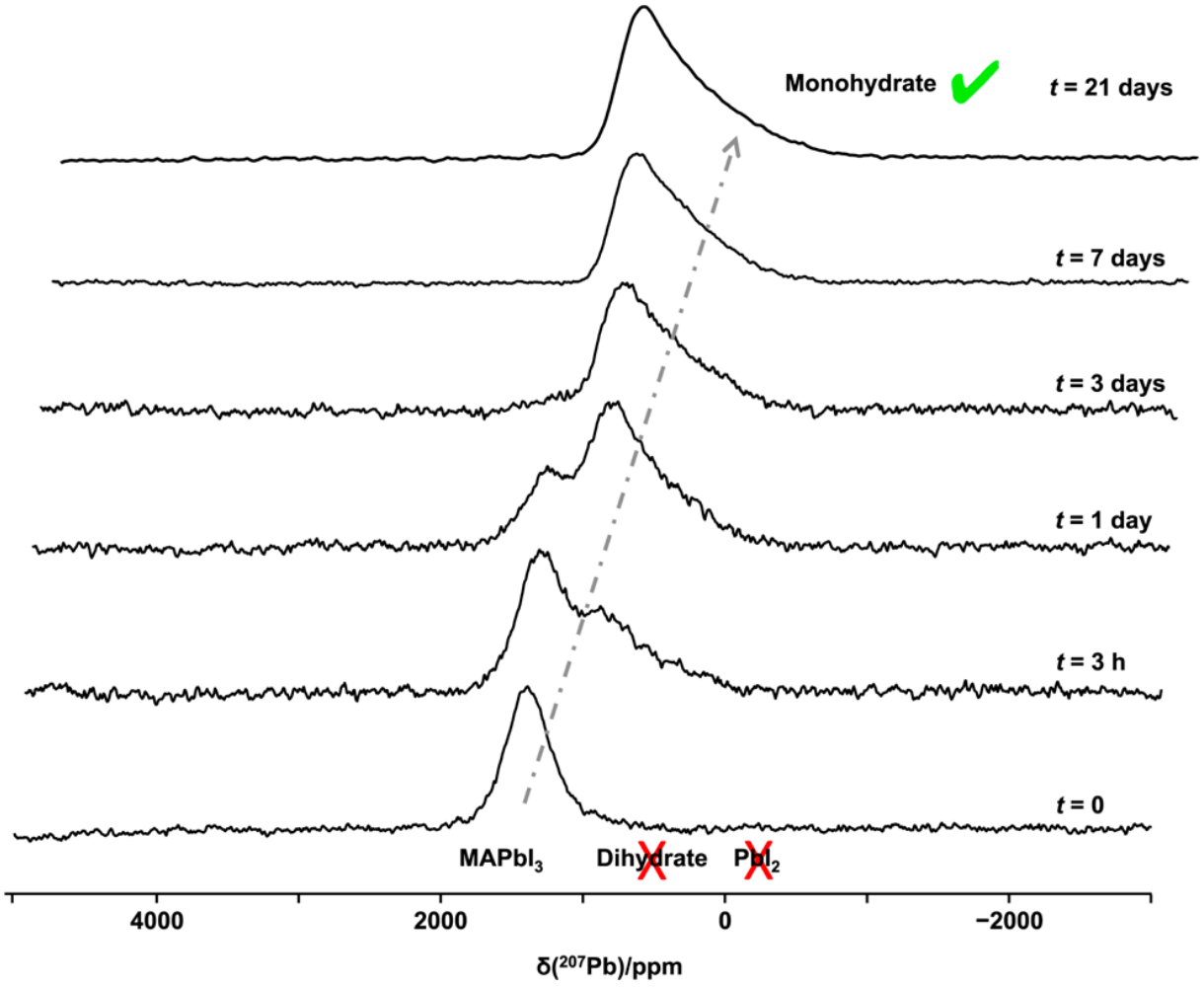

Figure 2.3: ^{207}Pb NMR spectra of stationary samples acquired at the indicated times after the start of humidification at 80% at 293 ± 1 K. Spectra were acquired at 7.05 T.

A powder XRD pattern obtained for the t = 21 day sample, simulated using the single-crystal XRD data for the monohydrate (see Figure 2.4),[55] confirms that the product is the monohydrate; as for the ^{207}Pb NMR spectra, there is no indication from this

XRD pattern that either the dihydrate or PbI_2 are decomposition products.

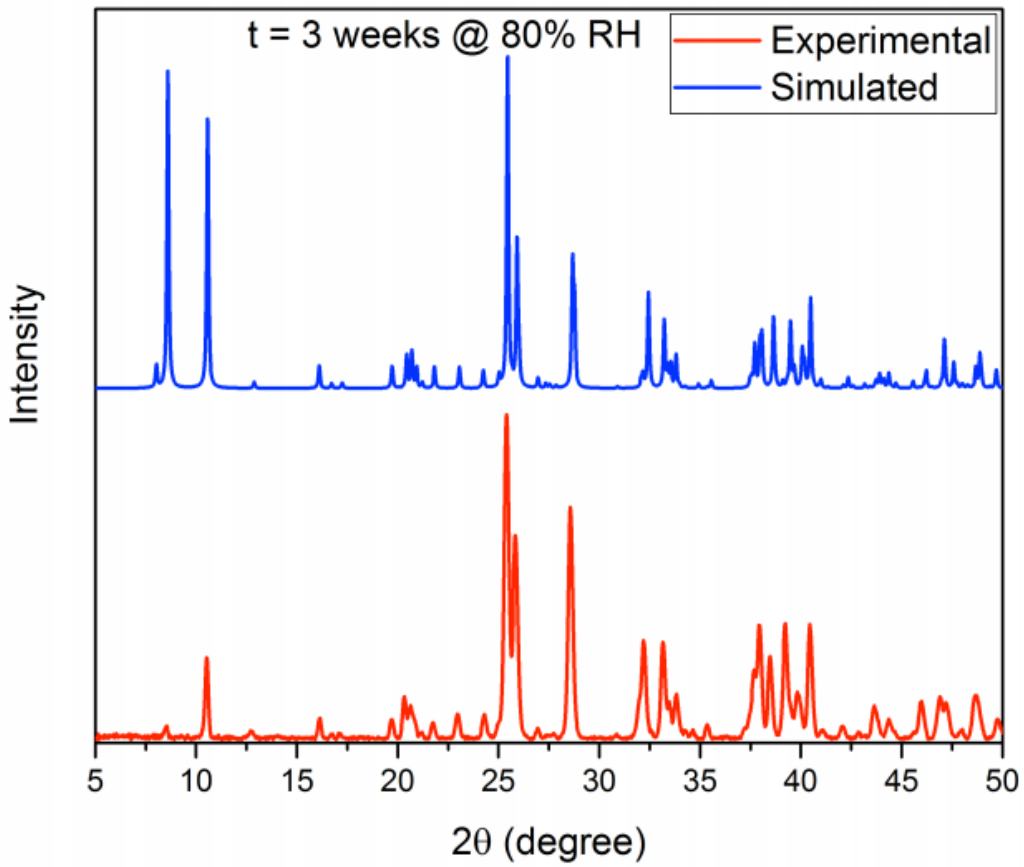

Figure 2.4: XRD pattern of $MAPbI_3$ placed in the humidity cell at 80% RH for 3 weeks and simulated pattern of the monohydrate. The simulated pattern is based on the reported single crystal data.

The response of the monohydrate to elevated temperatures was investigated via NMR spectroscopy. Figure 2.5 illustrates ^{207}Pb NMR spectra of a stationary sample of the monohydrate acquired in the 293-341 K temperature range. Because of possible dehydration during the 2 h time period needed to acquire the individual spectra shown in this figure, subspectra were acquired in 30 min time blocks under identical conditions and the resulting free induction decays were summed prior to processing. There was no variation in the subspectra acquired for a given temperature up to and including 313 K, indicating that dehydration did not occur at or below this temperature.

However, as seen in Figure A.4, at 324 K, the intensity of the peak attributed to the monohydrate diminished significantly in the course of the 2 h required to acquire the total spectrum, suggesting dehydration of the monohydrate. The peak at 1380 ppm arising from $MAPbI_3$ was not immediately detected, although, as seen in Figure 2.5,

it was observed for a spectrum acquired at 341 K.

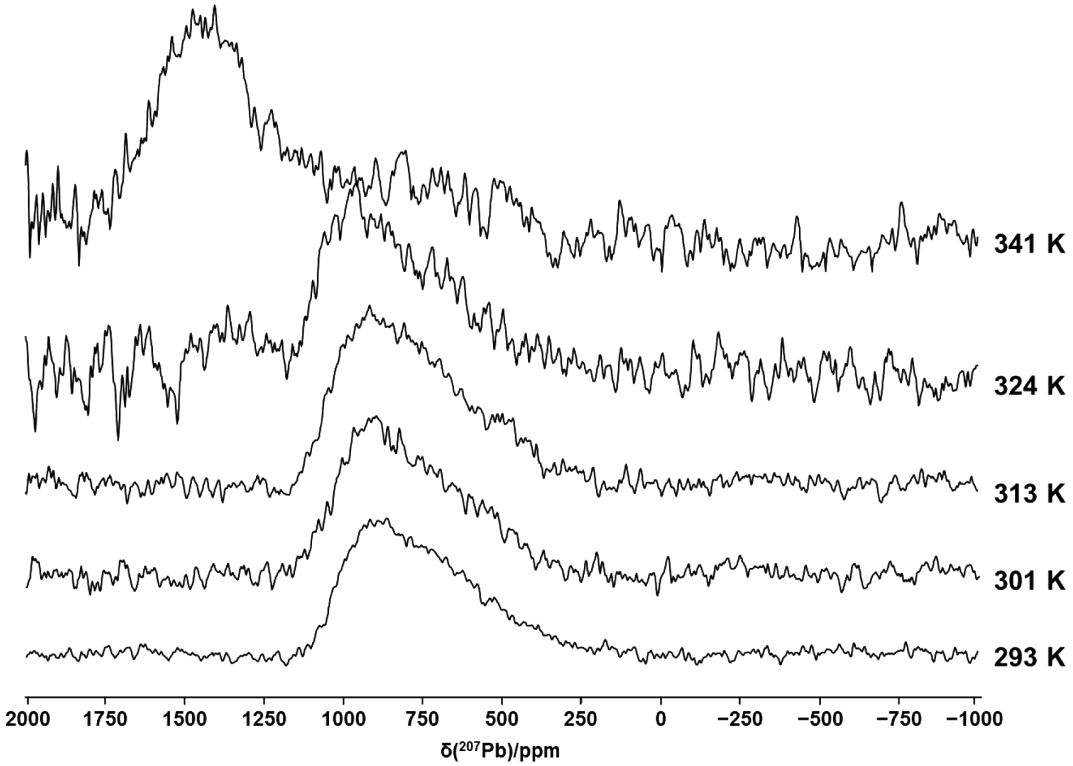

Figure 2.5: ^{207}Pb NMR spectra of a stationary sample of $MAPbI_3{\cdot}H_2O$ acquired at 11.75 T at the indicated temperatures. Each spectrum shown here is the sum of four subspectra acquired under the same conditions. The spectrum acquired at 324 K is noisier because of dehydration of the monohydrate (see text).

Spectra shown in Figure 2.5 clearly indicate that $MAPbI_3$ can indeed be recovered from the monohydrate with moderate heating. To further verify that $MAPbI_3$ had been recovered, ^{207}Pb NMR spectra of the sample were acquired at 7.05 T (see Figure A.5). These spectra are virtually identical to those for $MAPbI_3$, also shown in this figure.

When the monohydrate was first synthesized according to literature methods, it dehydrated under ambient conditions in a period of minutes, turning from yellow to black if exposed to air, unless stored in a sealed container. However, in the course of our investigations, we observed that the monohydrate obtained by placing a finely ground $MAPbI_3$ sample in the humidity cell at 80% RH for a long period of time (3 weeks) did not dehydrate as rapidly.

To investigate, the sample was exposed to the atmosphere by leaving it in an open beaker for over 4 h. There was no indication of dehumidification (i.e., the sample re-

mained yellow rather than turning black). However, when placed in an oven at 373 K, the sample turned black in less than 30 min, indicating that $MAPbI_3$ had been recovered. The XRD pattern for this three-week sample obtained prior to exposure to the atmosphere or to high temperatures, shown in Figure 2.4, indicates high crystallinity, which may explain why it is more stable and less vulnerable to dehydration.

Several of the preceding observations on the response of bulk $MAPbI_3$ to high relative humidity have also been reported for the sample on films. Berger and co-workers,[34] Leguy et al.,[27] and Zhao et al.[57] reported the formation of the monohydrate following exposure of $MAPbI_3$ films to 80% relative humidity, while Yang et al. described the product of humidification as the dihydrate "or a very closely related hydrate".[37] These groups all reported that $MAPbI_3$ could be recovered from the monohydrate. However, contrary to our observations, Berger and co-workers found that long-term (i.e., $\geq$6 days) exposure of the film to RH = 80% leads to the formation of the dihydrate and also detected the presence of PbI_2,[34] as did Zhao et al.[57] who also reported the formation of MAI (vide infra). Likewise, Leguy et al.[27] reported the dihydrate as a decomposition product of high humidity, but only traces of PbI_2 were detected despite predictions based on Eq. 2. The latter authors speculate that PbI_2 may be in an amorphous or nanocrystalline phase and thus difficult to detect via XRD.

The sensitivity of $MAPbI_3$ to high RH leads one to question whether the sample is also sensitive to lower RH levels. To investigate, a sample of $MAPbI_3$ was placed in the humidity cell in a 40% RH environment at 293 K for 11 days. The compound remained black, and its ^{207}Pb NMR spectra (Figure A.6) were very similar to those for $MAPbI_3$, indicating that bulk $MAPbI_3$ is stable at this level of humidity. This is similar to the observations of Wang and Chen, who found that at 40% RH a $MAPbI_3$ solar cell (with no capsulation) remained mostly unchanged for 100 days, with no evidence of the decomposition of the $MAPbI_3$ to a hydrate or to PbI_2. These authors reported that the stability of $MAPbI_3$ depends greatly on the purity and morphology of the film. Berger and co-workers[34] also found that $MAPbI_3$ is unaffected for RH $\leq$ 50%. In contrast, Shirayama and co-workers[42] recently investigated thin layers of $MAPbI_3$ on film, prepared by a laser evaporation technique, and found that, at 40% RH, the sample degraded in 1 day through the formation of both PbI_2 and the dihydrate.

2.3.4 Response of $MAPbI_3$ to Direct Exposure to H_2O(l) at Ambient Temperature

In their investigation of $MAPbI_3$, Leguy et al.[27] reported that exposure to H_2O(l) led to the irreversible formation of PbI_2; intermediate products (i.e., the monohydrate or the dihydrate) were not observed. These authors undertook their measurements on thin films. To determine whether the same holds true for the fine powders investigated in this work, 50 µL of H_2O(l) was added to approximately 200 mg of $MAPbI_3$. Comparison of the ^{207}Pb NMR spectra before and after addition of the H_2O (parts a and b of Figure 2.6, respectively) demonstrates that the monohydrate is obtained under these conditions, contrary to the observations of Leguy et al.[27] Considering the low stability of the monohydrate, the sample was packed into an NMR rotor immediately following the addition of H_2O(l). Following the acquisition of the spectrum shown in Figure 2.6b, the sample was removed from the rotor and placed in a Petri dish to which a further 200 µL of H_2O(l) was added. To ensure that the sample was dry, it was allowed to stand overnight under ambient conditions before it was packed; the spectrum obtained from this sample, which shows that PbI_2 is indeed obtained after exposure to a sufficient amount of H_2O(l), is shown in Figure 2.6c. To verify that the peak at -27 ppm is not due to a previously undetected hydration product, the sample was then placed in a Petri dish and dried for 3 h at 343 K (above the $MAPI_3$ tetragonal-cubic phase transition). The spectrum, shown in Figure 2.6d, is unchanged, consistent with the formation of PbI_2. The ratio of $MAPbI_3$:PbI_2 is approximately 2:1, although this value is no doubt dependent on initial conditions. Note that the ease with which the monohydrate was initially formed and its rapid dehydration suggest that it is almost certainly an intermediate product between $MAPbI_3$ and PbI_2 such that, depending on how soon after exposure to H_2O(l) the spectrum is acquired, a spectrum with contributions from only the monohydrate and PbI_2, or one with contributions from all three compounds, might be obtained. However, we saw no evidence for the dihydrate in this series of measurements.

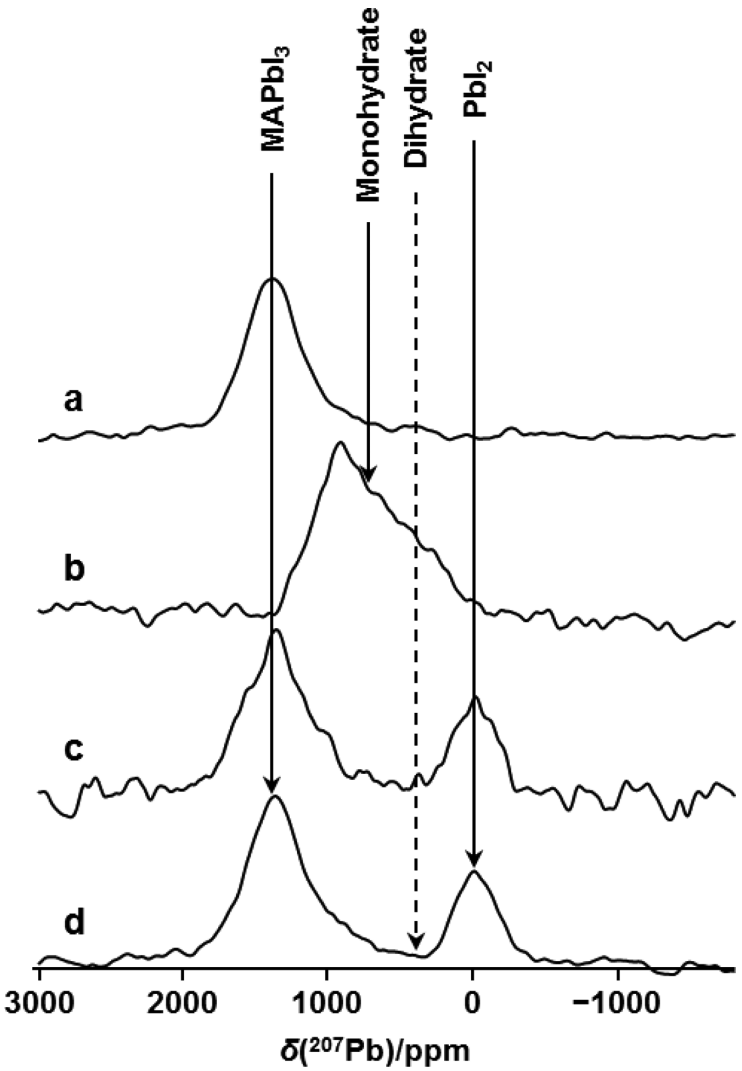

Figure 2.6: ^{207}Pb NMR spectra of (a) $MAPbI_3$, (b) the sample from part a following the addition of 50 µL of H_2O, (c) the sample from part b following the addition of a further 200 µL of H_2O, and (d) the sample from part c after it was heated at 343 K for 3 h. The solid lines indicate the chemical shifts of identified compounds, while the dotted line is that for a proposed decomposition product that was not observed. Spectra were acquired at 7.05 T and 294 K.

2.3.5 Response of $MAPbI_3$ to Humidity at Elevated Temperatures.

Understanding the response of $MAPbI_3$ to elevated temperatures is an important consideration if it is to be used in solar cells, since the absorbed light energy elevates the temperature of the apparatus to above 350 K.[43] In fact, damp-heat testing is an important component of commercial solar panel design.[37] Although $MAPbI_3$ transitions from the tetragonal to the cubic phase at 326.6 K,[58,59] there is no significant chemical shift effect due to this transition. Thus, significant changes to the ^{207}Pb NMR chemical

shifts at elevated temperatures indicate a response to environmental conditions, rather than merely being a consequence of the phase transition. To investigate the response of $MAPbI_3$ to elevated temperatures and humidity, a powder sample was placed in a Petri dish on a hot plate inside the humidity cell with the temperature of the hot plate maintained at 358 ± 3 K and the humidity of the cell maintained at 45 ± 5%. The presence of the hot plate within the cell increased the surrounding air temperature to 308 ± 2 K. Samples were extracted after 0, 3, and 24 h, as well as 8 days. The sample was sealed within a zirconia NMR rotor immediately after extraction from the humidity cell, although it was not always possible to immediately acquire the NMR spectra; there was no indication that the sample degraded over time once packed.

Figure 2.7 illustrates the ^{207}Pb NMR spectra of these samples. After 3 h, decomposition products, if present, are not detected. However, after 24 h, a ^{207}Pb NMR peak at the position expected for PbI_2 is detected; this peak contributes approximately 30% of the total intensity. The process of decomposition under these conditions proceeds at a slow pace; after 8 days, PbI_2 contributes approximately 55% of the total NMR signal. The process is expected to continue until only PbI_2 remains, although this would take several weeks under the conditions described here. If any monohydrate or dihydrate was produced during this process, their ^{207}Pb NMR signal was of insufficient intensity to be detected. In their investigation of encapsulated $MAPbI_3$ solar cells, Han et al.[43] also found that PbI_2 was a decomposition product of the sample placed under similar conditions of heat and humidity, though, in this case, the Ag layer forming part of the solar cell may have been a factor.

This series of measurements demonstrates that, under moderately elevated temperatures and a humid environment, $MAPbI_3$ slowly decomposes to PbI_2. The process is slow, but since it is irreversible, it is a serious concern for solar cell engineers.

2.3.6 Response of $MAPbI_3$ to Elevated Temperatures.

To ascertain that both heat and humidity are required to drive the decomposition of $MAPbI_3$ to PbI_2, we also studied the effect of exposing $MAPbI_3$ to an elevated temperature in a dry environment. A fine $MAPbI_3$ powder sample was placed in a

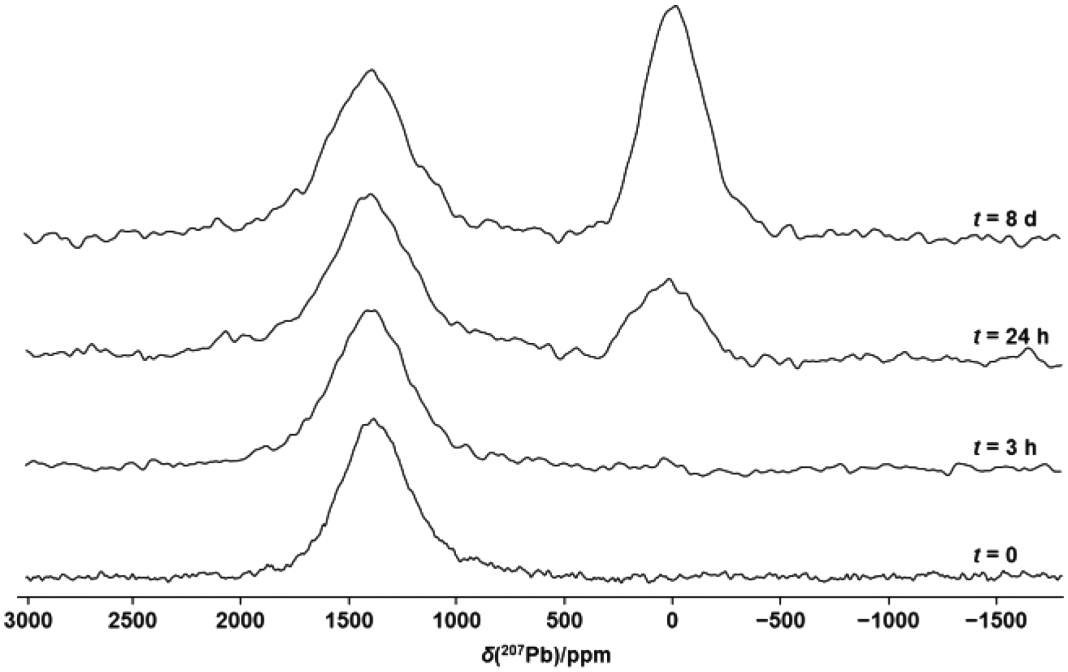

Figure 2.7: ^{207}Pb NMR spectra of stationary samples of $MAPbI_3$ (1385 ppm) and its product PbI_2 (-27 ppm) following exposure to heat (358 K) and 45% RH. Spectra were acquired at 293 K at 7.05 T.

furnace at 378 K for 4 days and then packed into an NMR rotor immediately after removal from the furnace. Comparison of the ^{207}Pb NMR spectra of the product with those for $MAPbI_3$ (see Figure A.7) indicates that the product remains $MAPbI_3$, with no indication of PbI_2. In their study of encapsulated $MAPbI_3$ solar cells discussed above, Han et al.[43] did find some degradation of the solar cell performance when exposed to elevated temperatures and low (10%) humidity, although the degradation was not as extreme as when both heat and humidity were present.

2.3.7 Response of the Dihydrate to Elevated Temperatures

The dihydrate has been proposed as the second step in the decomposition of $MAPbI_3$ to PbI_2 (eq 1),[27] and as for the monohydrate, this step is thought to be reversible. Hence, ^{207}Pb NMR spectra of a stationary dihydrate sample, prepared as outlined above, were acquired at elevated temperatures to determine if $MAPbI_3$ can be recovered from the dihydrate and whether the monohydrate is an intermediate step in this recovery. Spectra (not shown) acquired at 301 and 313 K were virtually identical to that for the dihydrate shown in Figure 2.1. Obtaining these ^{207}Pb NMR spectra was hampered by

the limited sample volume (approximately 85 mg, or 1/3 of the 4 mm NMR rotor), by the fact that, following the onset of dehydration, it proceeds quickly, and by the difficulties in obtaining variable temperature NMR data as discussed above; thus, the spectra we obtained had a low signal/noise ratio. Nevertheless, as seen in Figure 2.8, we are able to follow the dehydration process via ^{207}Pb NMR spectroscopy. A spectrum acquired at 324 K (Figure 2.8a) is virtually identical to that obtained for the dihydrate at room temperature (Figure 2.1). However, by the time the next spectrum was acquired, approximately 15 min after the temperature had stabilized at 336 K, a broad peak, covering the frequency range seen for the monohydrate and the dihydrate, was observed (Figure 2.8b; a comparison with those for the monohydrate and dihydrate is shown in the inset), suggesting that part of the sample was dehydrating such that the monohydrate was obtained. During acquisition of the four subsequent spectra (Figure 2.8c-f), each of which took 15 min, first the signal at the position of the dihydrate was lost, and by the last spectrum, virtually all the signal attributed to the monohydrate was also lost. The loss of the signal attributed to the monohydrate is unsurprising, since it was also lost when the monohydrate was heated at 324 K (see Figure 2.8). As discussed above, detecting $MAPbI_3$ at 11.75 T proved challenging. Nevertheless, a spectrum obtained the following day at 7.05 T (Figure 2.8g) confirmed that $MAPbI_3$ had been recovered. The dihydrate was not observed in any of our experiments as a degradation product of $MAPbI_3$, which is not surprising, since, to the best of our knowledge, the only way to prepare the pure dihydrate requires an excess of the MAI, which is how the sample used here was synthesized.[1] Starting with pure $MAPbI_3$ with a 1:1 molar ratio of MAI:PbI_2, it is unlikely that the dihydrate would form.

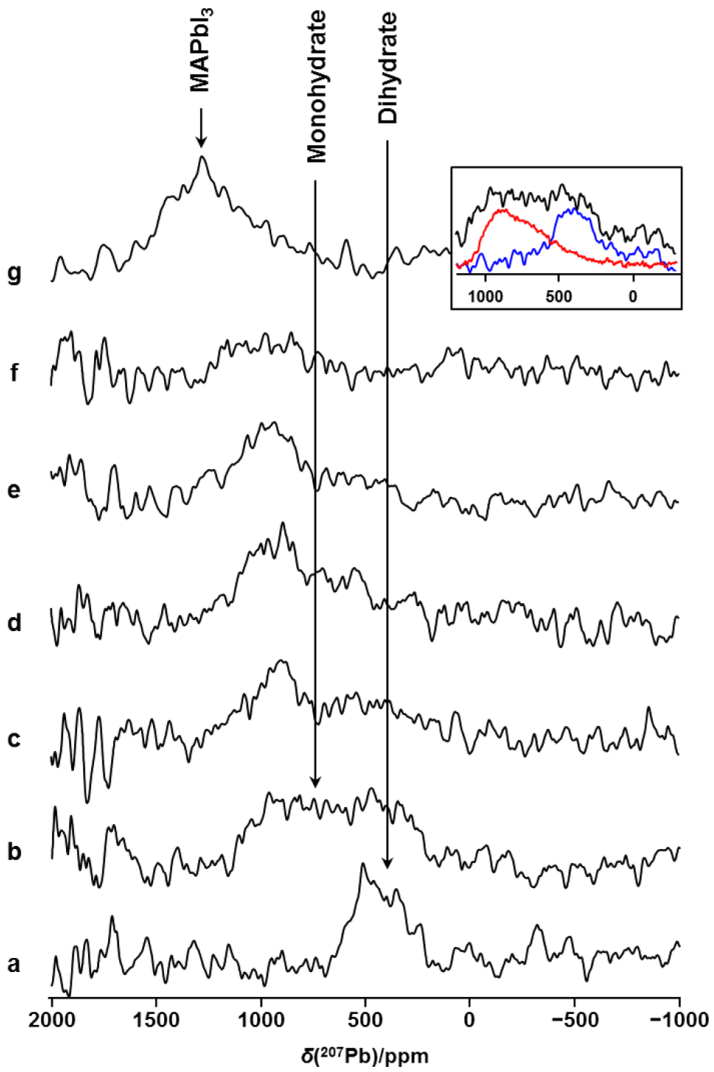

Figure 2.8: ^{207}Pb NMR spectra illustrating the response of the dihydrate[1] to elevated temperatures: (a) a spectrum acquired at 324 K; (b-f) a series of spectra acquired at 336 K in 15 min increments. These spectra are of stationary samples, acquired at 11.75 T; the noise to high frequency is attributed to interference from a local FM radio station. In part g, a spectrum of the stationary sample acquired on the following day at 7.05 T at 294 K is shown. In the inset, the spectrum shown in part b is compared to the spectra for the monohydrate (red) and the dihydrate (blue).

Table 2.1: Summary of $MAPbI_3$ Degradation Products under Humidity and Thermal Treatments[a]

Products	***$MAPbI_3$***	***Monohydrate***	***Dihydrate***	***PbI_2***
I	X	X		
II	X			
III	X	X		
IV		X		
V	X			X
VI	X			X
VII	X	X	X	
VIII	X			X
IX	X			

[a]Products: (**I**) $MAPbI_3$ placed in a humidity chamber at 80% RH over a period of up to 21 days at 293 K. (**II**) $MAPbI_3$ cycling between the tetragonal and cubic phases of $MAPbI_3$ (*in situ* NMR). (**III**) Monohydrate from I (t = 7 days) heated to 341 K and then back to 293 K, i.e., the monohydrate dehydrated back to $MAPbI_3$ (*in situ* NMR). (IV) 50 µL of H_2O(l) added to $MAPbI_3$. (V) 200 µL added to the product of **IV**; sample allowed to dry under ambient conditions overnight. (**VI**) Sample from **V**, placed in a furnace at 343 K for 4 h. (**VII**) The synthesized dihydrate, heated through the tetragonal and cubic phase transition for $MAPbI_3$, forming the monohydrate and then $MAPbI_3$ (*in situ* NMR). (**VIII**) $MAPbI_3$ placed on a hot plate at 358 K and 45% humidity. (**IX**) $MAPbI_3$ placed in an oven at 378 K for 4 days and then packed in an NMR rotor and spectra acquired at room temperature.

2.4 Conclusion

We have presented a solid-state NMR study of $MAPbI_3$ and of its proposed decomposition products: the monohydrate and dihydrate derivatives of the compounds as well as PbI_2. We have demonstrated that ^{207}Pb NMR spectroscopy is a sensitive technique to distinguish which of these products, if any, have been obtained. A significant conclusion of our investigations is that exposure of bulk samples of $MAPbI_3$ to high humidity under ambient temperature conditions leads to the formation of the mono-

hydrate but not to other decomposition products. This is in contrast to many studies of $MAPbI_3$ on films; since the $MAPbI_3$ is easily recovered from the monohydrate, this is an important observation. However, exposure to both heat and humidity, or to excess H_2O(l), does lead to an irreversible decomposition, with PbI_2 as the main solid product. The varying observations discussed in this section and summarized in Table 2.1 and Scheme 1 demonstrate the high sensitivity of $MAPbI_3$ to subtle differences in conditions or in the preparation of the sample. On the basis of our observations, equations 3, 4, and 5 are proposed to describe the sensitivity of $MAPbI_3$ to humidity, heat, or water:

$$CH_3NH_3PbI_3\ (s) + H_2O\ (g) \rightleftharpoons CH_3NH_3PbI_3{\cdot}H_2O\ (s) \quad \text{..... Eq. 3}$$

$$CH_3NH_3PbI_3\ (s) \xrightarrow{H_2O\ (g),\ \Delta} CH_3NH_3\ (g) + HI\ (g) + PbI_2\ (s) + H_2O \quad \text{..... Eq. 4}$$

$$CH_3NH_3PbI_3\ (s), \text{in excess} + H_2O\ (l) \rightleftharpoons CH_3NH_3PbI_3{\cdot}H_2O\ (s) \xrightarrow{H_2O\ (l)} CH_3NH_3I\ (aq) + PbI_2\ (s) + H_2O\ (l) \quad \text{..... Eq. 5}$$

In the work discussed here, heat was used to recover $MAPbI_3$ from the monohydrate. However, the monohydrate dehydrates spontaneously under ambient conditions, albeit slowly if we are dealing with samples that were annealed (294 K) within the humidifying chamber over prolonged periods of time. XRD data (Figure 2.4) suggest that this increases the degree of crystallinity; the diffraction peaks narrow considerably for the finely ground samples discussed above.

Sample stability is a critical consideration for solar cell engineers. Our study suggests that the bulk material is much more stable than thin films. We hope that the information provided here may serve as a guide in ongoing efforts to understand the intrinsic stability of $MAPbI_3$ and its use in the design and fabrication of these promising commercial hybrid organic-inorganic perovskite solar cells.

Chapter 3

Mechanochemical Synthesis of Mixed Halide Perovskites

In this chapter, the work done on studying the solid-solution behaviour in mixed-halide lead perovskites (MHPs) is presented,[1] with focus on the novel mechanochemical synthesis approach. The material system under consideration in this chapter has the general formula $APbX_3$, where A is either methylammonium (MA) cation or formamidinium (FA) cation, X is either a single halide (i.e. Cl, Br, or I) or mixed halides (e.g. $Cl_{0.5}Br_{0.5}$).

3.1 Abstract

Mixed-halide lead perovskite (MHP) materials are rapidly advancing as next-generation high-efficiency perovskite solar cells due to enhanced stability and bandgap tunability. In this work, we demonstrate the ability to readily and stoichiometrically tune the

[1] An extended version of this chapter has been published in 2 separate papers as follows:

Abhoy Karmakar, ***Abdelrahman M Askar***, Guy M Bernard, Victor V Terskikh, Michelle Ha, Sahil Patel, Karthik Shankar, Vladimir K Michaelis, *Chem. Mater.*, **2018**, 30 (7), 2309–2321

Abdelrahman M. Askar, Abhoy Karmakar, Guy M. Bernard, Michelle Ha, Victor V. Terskikh, Benjamin D. Wiltshire, Sahil Patel, Jonathan Fleet, Karthik Shankar, and Vladimir K. Michaelis, *J. Phys. Chem. Lett.*, **2018**, 9 (10), 2671–2677

halide composition in MA- & FA-based MHPs using a mechanochemical synthesis approach. Using this solvent-free protocol we are able to prepare domain-free MHP solid solutions with randomly distributed halide ions about the Pb centre. In MA-MHPs, up to seven distinct $[PbCl_xBr_{6-x}]^{4-}$ environments are identified, based on the ^{207}Pb NMR chemical shifts, which are also sensitive to the changes in the lattice constants (obtained from powder X-ray diffraction used for long-range crystallinity characterization) resulting from the substitution of Br by Cl, along with bandgap obtained from reflectance measurements through Tauc Plots; both obeying Vegard's law. For FA-MHPs, similar results were obtained; nevertheless, we achieved compositions not previously accessible through the solvent synthesis (SS) technique.

We demonstrate a straightforward and rapid synthetic approach to forming highly tunable stoichiometric MHP solid solutions while avoiding the traditional solution synthesis method by redirecting the thermodynamically driven compositions. The solvent-free mechanochemical synthesis approach is also compared to traditional solvent synthesis, revealing identical solid-solution behaviour; however, the mechanochemical approach offers superior control over the stoichiometry of the final mixed-halide composition, which is essential for device engineering. Our results pave the way for advanced methods in atomic-level structural understanding while offering a one-pot synthetic approach to prepare MHPs.

3.2 Introduction

A particularly promising area of research in the renaissance of metal halide perovskite has been on mixed-halide perovskites (MHPs) of the type ABX_3, where A = $CH_3NH_3^+$ (MA) or $CH(NH_2)_2^+$ (FA), B = Pb^{2+}, and X = Cl^-, Br^-, and I^-.[60] One advantage that MHPs offer is the bandgap tunability made possible through the halide composition, which is important for applications such as tandem solar cells and light emitting diodes (LEDs).[61] Additionally, MHPs offer enhanced stability against moisture, and thus their use to achieve more stable and higher-performing PSCs is becoming routine.[62,63]

MHPs possess an intriguing range of properties stemming from the degrees of freedom

in their synthesis due to the relatively easy reversible-halide exchange both in solution and between gas and solid phases.[64,65] Nevertheless, challenges with MHPs have also been reported. In particular, the consequences of halide ion mobility on the device performance[66–68] and of phase segregation due to photoinduced halide ion migration[69–72] must be considered. This has been the case in particular for MA-MHPs, where most of the studies on photo-induced halide ion migration have been carried out on this material system.

On the other hand, FA-based perovskites have shown superior optoelectronic properties such as extended carrier diffusion lengths and lifetimes when compared to their MA-containing analogues, both in polycrystalline and single-crystal forms.[73–76] Moreover, $FAPb(Br_xI_{1-x})_3$, where $0 < x < 1$, has been the focus of research efforts exploring the tunable bandgap and charge carrier dynamics for applications in tandem solar cells and LEDs.[63,75,77,78] In some of these studies it was reported that when $0.3 < x < 0.5$, no crystalline phase can be achieved using traditional solvent synthesis (SS) techniques, but rather an amorphous phase is obtained, which has been attributed to a phase transition from a trigonal ($x < 0.3$) to a cubic ($x > 0.5$) structure. Nevertheless, high-resolution neutron powder diffraction data suggests that α-$FAPbI_3$ ($x = 0$) adopts the cubic (Pm-3m) perovskite unit cell at room temperature[79] rather than the trigonal structure reported for high-temperature solution-deposited α-$FAPbI_3$ films.[80,81] This is in agreement with observations based on single-crystal or powder X-ray diffraction (pXRD) analyses of α-$FAPbI_3$ prepared by the inverse temperature crystallization (ITC) technique.[24] Aside from $FAPb(Br_xI_{1-x})_3$ MHPs, $FAPbCl_3$ and $FAPb(Cl_xBr_{1-x})_3$ have rarely been studied; the few studies have focused on nanoparticles.[82–86]

Traditionally, perovskite materials are synthesized using solvent synthesis (SS) routes, but recently a mechanochemical synthesis (MCS) technique has been proposed as a solvent-free and scalable method to prepare halide perovskite materials. This methodology shows enhanced material properties, achieving similar or better solar cell device performance when compared to SS-prepared devices, along with great flexibility in tuning the dimensionality (3D, 2D, or 0D) of the prepared perovskite materials.[87–92] For instance, preparing $CH_3NH_3PbI_3$ PSCs by MCS leads to a reduction in the inter-

facial trap density in fabricated PSCs in comparison to the same compound prepared through standard solvent synthesis.[93] Recently, MCS was used to prepare complex mixed cation (Cs, Rb, FA, in addition to MA) lead halide perovskite materials used in the highest performing and most stable PSCs reported to date, revealing similar structural properties to the corresponding perovskite materials prepared by traditional two-step casting techniques.[94]

MCS has been successfully utilized for a long time in other material systems, including metal-organic frameworks (MOFs),[95–97] polymorphs in drug design,[98–100] and composite/metal oxide nanomaterials.[101,102]

The high mobility of halide ions in halide perovskites prompted us to investigate the potential of MCS in the synthesis of $APb(X_xX'_{1-x})_3$ (A = MA or FA , X and X' = Cl^- and Br^- or Br^- and I^-) MHPs for the first time from their parent $APbX_3$ compounds and to examine at the atomic scale the true halide mixing in the products. The techniques used for the application of MCS (Schemes 4.1 & 4.2) were manual hand grinding (HG) using a mortar and pestle and a ball milling (BM) method.

Solid-state nuclear magnetic resonance (NMR) spectroscopy is a highly sensitive tool for identifying atomic-level chemical structure and dynamics. With the ^{207}Pb nucleus exhibiting a large chemical shift range of nearly 20,000 ppm, ^{207}Pb NMR spectroscopy is ideal for the study of the Pb chemical environment.[53,103–108] Hence, the technique is applied in our investigation of MCS MA- & FA-MHPs. To complement NMR spectroscopy and to gain useful insights on the long-range order (crystallinity) in the MHPs, powder X-ray diffraction is used. In addition, reflectance measurements were utilized to gain information pertaining to optical bandgaps in MHPs.

In this work, we explore the MCS route to synthesize MA- & FA-based MHPs and probe their long- and short-range chemical structure using pXRD and ^{207}Pb NMR spectroscopy, respectively. In addition, their optical properties are explored using reflectance measurements. We find that MCS is an effective way to prepare MHPs solid solutions with random halide arrangements about the Pb centre, avoiding phase-segregated domains along with superior control over halide stoichiometry, including compositions not previously accessible using traditional SS methods. We also com-

pare samples of the same/similar composition (by synthetic loading or final product composition) prepared by SS and MCS.

$MAPbI_3$ prepared using the MCS method has been shown to yield a product with superior solar cell performance and characteristics (e.g. larger crystalline grains, less current-voltage hysteresis, and reduced interfacial trap density) compared to the corresponding product prepared via SS;[87,93] thus, we demonstrate that the MCS route described herein for the more commonly used MHPs is a very promising technique as an efficient strategy for commercializing these systems for a wide variety of photovoltaic and optoelectronic applications.

Note: Experimental details are available in Appendix B.

3.3 Results & Discussions

Schemes 3.1 & 3.2 show schematics of the MCS process used to prepare the MA- and FA-based MHPs, respectively. For MA-MHPs, the focus was mainly on Cl/Br mixtures, i.e., $MAPb(Cl_xBr_{1-x})_3$, which was prepared by HG as well as BM (See Appendix B for details) and the results from both method were compared to each others. On the other hand, for FA-MHPs $FAPb(Cl_xBr_{1-x})_3$ was prepared by HG, while $MAPb(Br_xI_{1-x})_3$ was prepared by BM (*vide infra*) starting with their respective parent perovskites, $FAPbX_3$. For each series, three MHPs (x = 0.25, 0.5, 0.75) were synthesized.

Scheme 3.1 MCS Process for the Preparation of MA-MHPs. In the HG method, parent compounds are mixed in the required molar ratio using a mortar and pestle and the HG process continues for 1-2 h to obtain a uniform single-phase product. In MCS-BM, a similar approach is used, but instead of the HG process, an automated BM system is used for 1 h

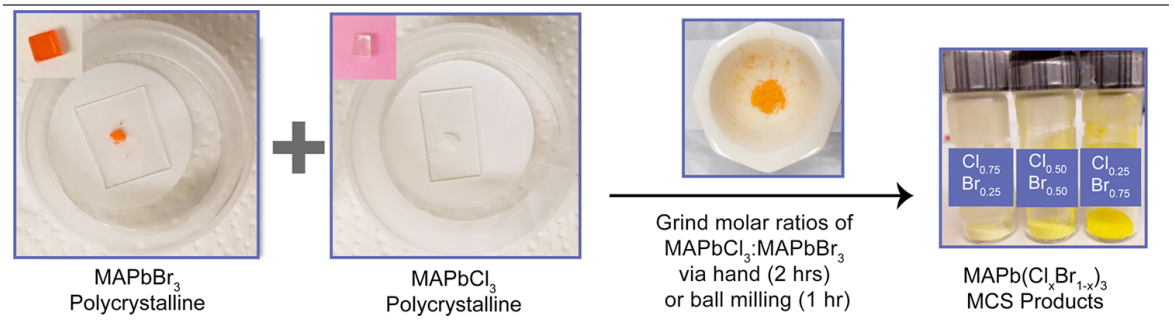

Scheme 3.2 MCS Preparation of FA-MHPs along with Crystal Structure Diagram Highlighting the $[PbX_xX'_{6-x}]^{4-}$ Octahedral Configurations and the Normalized Reflectance Spectra for the Parent $FAPbX_3$ and the MHPs (HG-$FAPb(Cl_{0.5}Br_{0.5})_3$ and BM-$FAPb(Br_{0.5}I_{0.5})_3$)

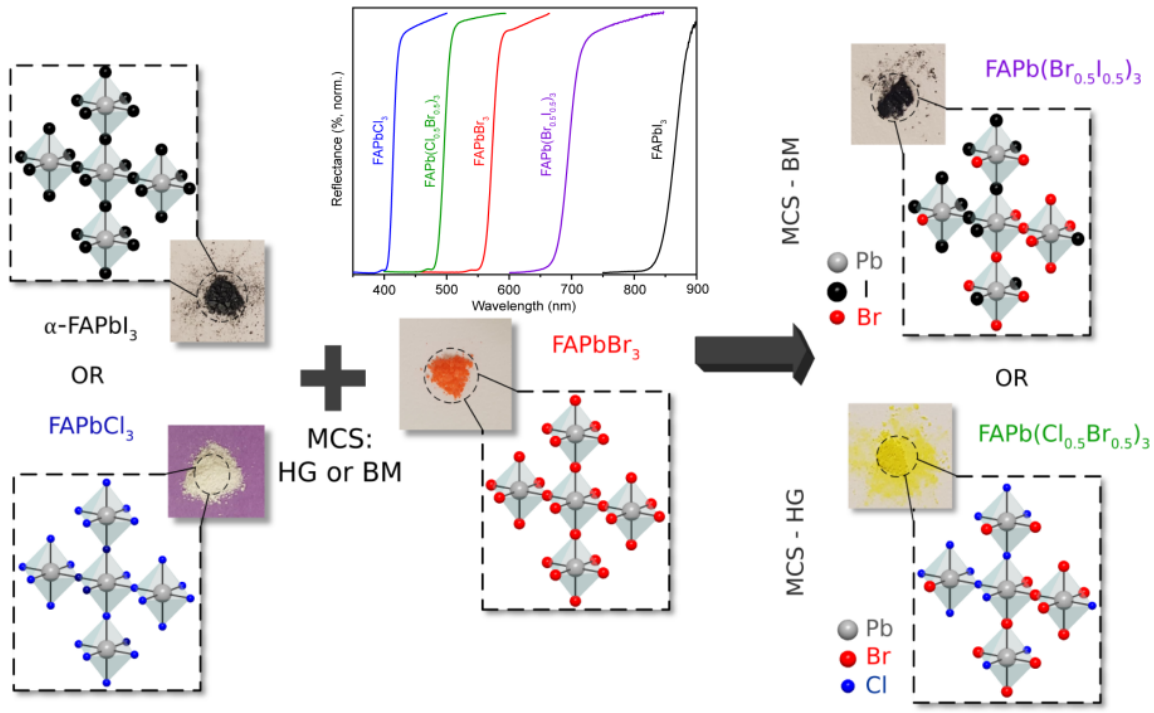

3.3.1 MCS of MA-MHPs

Figure B.2 shows ^{207}Pb NMR spectra of $MAPb(Cl_{0.5}Br_{0.5})_3$ prepared using the MCS-BM (Figure B.2a), MCS-HG (Figure B.2b), and SS (Figure B.2c) approaches, acquired at magnetic field strengths ranging from 7.05 to 21.1 T. The ^{207}Pb NMR spectra exhibit multiple sites, regardless of synthetic approach, illustrating the complex short-range Pb structure present in these otherwise simple primitive cubic crystalline solids (Pm-3m space group).[109] The resolution achieved at higher magnetic field strengths suggests distinct local Pb chemical environments with a potential to assign the various arrangements of halide ions within the MHPs qualitatively and quantitatively. This initial finding suggests that each $[PbX_xX'_{6-x}]^{4-}$ unit bears distinct NMR chemical shifts for the various Pb-halide octahedral arrangements demonstrating a binomial-like distribution characteristic of solid solution random halide mixing behaviour.

To date, most of the hybrid perovskite studies have relied extensively on diffraction-

based approaches.[110,111] Solid-state NMR spectroscopy, however, is rapidly emerging as an extremely informative analytical structural tool in characterizing both local structure and dynamics within photovoltaic perovskite materials.[53,94,104,112,113]

The observed ^{207}Pb NMR results (i.e., broad peaks and chemical shift distributions) for the BM, HG, and SS samples discussed above warranted further investigation to assess and interpret the local atomic structure.

MAPb(Cl_xBr_{1-x})$_3$ Hand Ground Mechanochemical Synthesis.

To unravel the complex nature of anion mixing about the Pb centre of the MHPs prepared with the SS and MCS methods, a series of standards of various $MAPbCl_3$/$MAPbBr_3$ molar ratios (100/0, 95/5, 83/17, 75/25, 50/50, 25/75, 5/95, and 0/100) were synthesized using the inverse temperature crystallization (parent compounds)[25,114] and MCS-HG (MHPs) methods and analysed by ^{207}Pb NMR spectroscopy to assess the changes in the first coordination sphere about the Pb nuclei.

At dopant level halide substitutions (i.e., $<5\%$), the halide ion transitions into the lattice replacing a Br for Cl (or Cl for Br) and immediately affects the lattice parameters (vide infra) of the solid-solution and the corresponding $\delta_{cs}(^{207}Pb)$ chemical shifts of $[PbBr_6]^{4-}$ or $[PbCl_6]^{4-}$, reflecting the sensitivity of ^{207}Pb NMR spectroscopy to changes within the material. Thus, it is not surprising that the chemical shift of a slightly Br-doped material is greater than that for the pure parent material ($MAPbCl_3$) since the ^{207}Pb resonance of the $MAPbBr_3$ parent complex appears at a higher chemical shift. Accounting for the 5% dopant concentration and for the coordination number of Pb (i.e., 6), 26.5% of the Pb centres are directly coordinated to a Br (or Cl) dopant within their octahedra. Fitting the peak areas of the ^{207}Pb NMR spectra for $MAPb(Cl_{0.05}Br_{0.95})_3$ and for $MAPb(Cl_{0.95}Br_{0.05})_3$, respectively, yielded ratios of 0.72:0.28 ($\pm$0.05) and 0.28:0.72 ($\pm$0.02) for the $[PbBr_6]^{4-}$ and $[PbCl_1Br_5]^{4-}$ units of the former and for the $[PbCl_5Br_1]^{4-}$ and $[PbCl_6]^{4-}$ units of the latter. Therefore, the lower frequency resonance in the ^{207}Pb NMR spectrum for $MAPb(Cl_{0.05}Br_{0.95})_3$ is assigned to a $[PbClBr_5]^{4-}$ local six-coordinate environment; likewise, the higher-frequency resonance observed in $MAPb(Cl_{0.95}Br_{0.05})_3$ is assigned to $[PbCl_5Br_1]^{4-}$.

As Cl replaces Br, the ^{207}Pb spectra break into additional resonances due to the formation of new Pb-X bonds whereby peak maxima shift to lower chemical shifts toward that for the parent compound, $MAPbCl_3$ (Figure 3.1a). These spectra demonstrate the sensitivity of ^{207}Pb NMR spectroscopy, as exemplified by the extremely large chemical shift range (∼17,000 ppm) for this nucleus,[105] to the halide environment about the Pb centre in these samples.[103,115]

The XRD patterns (Figure 3.1c) for all MCS-HG samples confirm that these consist of a single phase that adopts the cubic Pm-3m perovskite structure, with diffraction peak positions shifting to higher 2θ values with increasing Cl content. Substituting the chlorine anion (r = 167 pm) with a larger bromine anion (r = 182 pm) increases the lattice parameter, linearly obeying Vegard's law describing solid solution behavior, as shown in Figure 3.1d.[116] The MCS-HG synthesis method shows a single cutoff energy in the DR spectra (Figure B.1), which corresponds systematically to an increase in the bandgap energy from pure $MAPbBr_3$ to pure $MAPbCl_3$ (Figure 3.1d).

The results summarized in Figure 3.1 are those for a material with very fluid properties whose chemical structure can readily be adapted to randomly accommodate any mixture of halide anions using an MCS method. A systematic shift in the bandgap as halide substitution occurs supports the conclusion that these materials exhibit solid-solution behaviour, readily adjusting their local ($[PbX_xX'_{6-x}]^{4-}$) and long-range (lattice constant) structure as Cl is replaced by Br.

Careful analysis of multiple-field NMR spectra (Figure B.2), as well as XRD, energy dispersive X-ray (EDX), and DR data, indicate that both the MCS-HG and SS methods create a pure, single-phase crystalline solid. The relative populations of $[PbX_xX'_{6-x}]^{4-}$ chemical environments obtained using these methods, while somewhat different, behave similarly as the halide distribution changes from Br- to Cl-rich species.

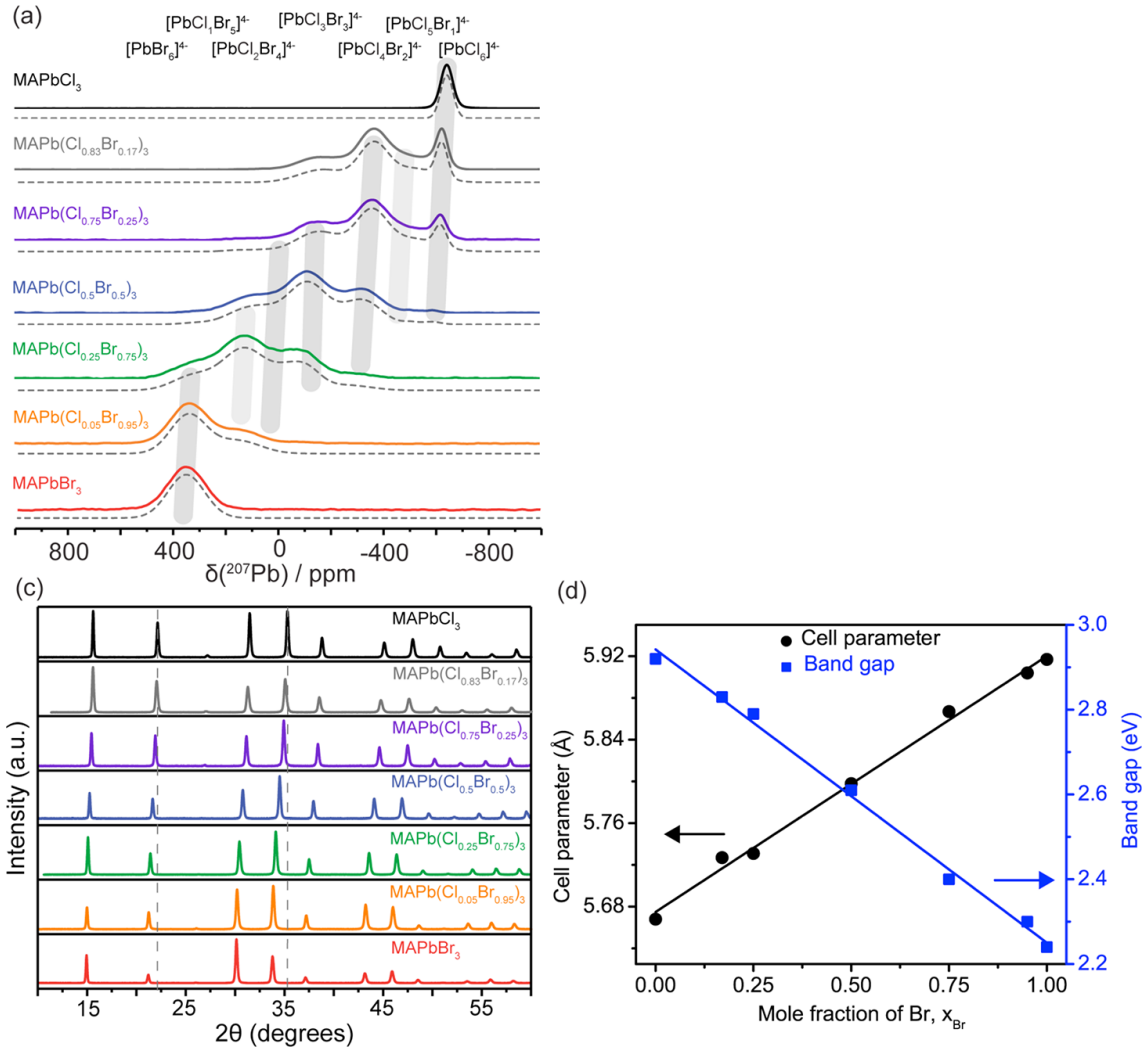

Figure 3.1: Nonspinning ^{207}Pb NMR spectra (11.7 T) of MCS-HG MHPs and their parent compounds (a). The assignment of the NMR peaks is shown at the top (the shaded areas are guides to the eye to identify specific NMR sites in the various spectra, and the dashed lines indicate simulated spectra). Powder X-ray diffraction data (c). Dotted lines are guides to the eye. A plot of cell parameter ($R^2 = 0.994$) and experimentally determined bandgaps extracted from Tauc plots ($R^2 = 0.994$) vs Br mole fraction for the MHP series (d).

Closer examination of the Cl/Br concentrations in the SS sample as determined by EDX reveals that the targeted $MAPb(Cl_{0.5}Br_{0.5})_3$ composition is in fact $MAPb(Cl_{0.58}Br_{0.42})_3$. The non-stoichiometric product obtained with the SS approach is nevertheless consistent with a binomial-like distribution (not shown here) once accounting for the new composition, with the expected chlorine-rich lead octahedra (i.e., $[PbCl_6]^{4-}$, $[PbCl_5Br_1]^{4-}$, $[PbCl_4Br_2]^{4-}$, and $[PbCl_3Br_3]^{4-}$) chemical environments (Figure B.2 b,c) over other halide mixing combinations. Likewise, the sample prepared by the SS method follows Vegard's law, with the lattice constants correlating to the final stoichiometry (see

Figure B.3 for the XRD pattern of this MHP prepared using the SS method). As for the sample prepared by MCS, there is no indication of phase-separated domains or amorphous structure in the experimental data. In a two-component mixture of $MAPbCl_3$ and $MAPbBr_3$ subjected to MCS, the thermodynamics are different from those in the three-component mixture resulting from SS (i.e., $MAPbCl_3$, $MAPbBr_3$, and the solvent). The former yields a stoichiometric final product while the latter yields a Cl-rich final product due to the altered driving forces for SS (i.e., nucleation and growth) compared to the high-energy MCS method.[38,117,118]

$MAPb(Cl_xBr_{1-x})_3$ Ball Milling Mechanochemical Synthesis.

Figure 3.2 shows powder XRD and nonspinning NMR spectra, as well as Tauc plots for the $MAPb(Cl_{0.5}Br_{0.5})_3$ sample prepared using solvent synthesis, hand grinding, and ball milling, illustrating the impact of these synthetic approaches on structural and physical properties. Powder XRD data for the samples indicate that the same crystal structure is obtained in all three cases, but the diffraction line widths indicate that the MCS-BM method yields products that produce broader lines (Figure 3.2a). The SS and HG samples indicate random distributions of halide environments about the octahedral Pb position $[PbCl_xBr_{6-x}]^{4-}$, with the resonance centered at -100 ppm being attributed to the $[PbCl_3Br_3]^{4-}$ chemical environment, *vide supra*. At low magnetic fields, the ^{207}Pb NMR spectrum of the BM sample is featureless (Figures B.2, 3.2b, and B.10), appearing Gaussian-like in shape, with evidence of multiple Pb octahedral environments only emerging from higher-field ^{207}Pb NMR data (21.1 T, Figure B.2a). As for the SS and HG samples, the solid-solution behavior is preserved for the BM samples. However, the high-energy milling process introduces short-range structural disorder in the otherwise well-ordered cubic environment. This creates a distribution of Pb-X distances and angles and thus leads to local disorder at the Pb sites, as is evident from the observed line widths that indicate a distribution of ^{207}Pb chemical shifts, while XRD data indicates that long-range periodic crystallinity is maintained (Figure 3.2a). The increase in line width of the powder XRD pattern and the amorphization of the well-defined microscopic crystalline solids as observed in field emission scanning electron microscopy, FESEM (Figures B.11 and B.12), as well as the impact on the

MA cation as indicated by ^{1}H and ^{13}C NMR spectroscopy (not shown here) further support the conclusion of local structural disorder determined from the ^{207}Pb NMR spectra.

To examine how the local disorder evolved over time, we obtained ^{207}Pb NMR spectra of samples of $MAPb(Cl_{0.75}Br_{0.25})_3$ prepared with 5 min and with 1 h of BM (Figures B.4 & B.5); these spectra confirm that the halide ions quickly begin to mix, already forming a highly ordered random solid solution after 5 min of BM. After 1 h of further high-energy milling, a degradation of the local octahedral structure occurs, and the $[PbCl_xBr_{6-x}]^{4-}$ octahedra exhibit short-range local disorder (NMR data) within an otherwise preserved hierarchical periodic crystalline solid framework (XRD data).

The impact of these synthetic approaches and corresponding structural changes on their optical responses were analyzed using DR[119] data (Figure B.6); these results indicate similar optical bandgaps for all three $MAPb(Cl_{0.5}Br_{0.5})_3$ samples, but preparing the MHP via the MCS route reduces the bandgap energy by 0.039 eV when compared to the SS technique (2.605 eV for HG vs 2.644 eV for SS). This change is attributed to the fact that the stoichiometry is preserved when using the MCS approach, as determined by the EDX analysis (Table B.1), which indicates that a 1.04:1.0 Cl/Br ratio is obtained for the HG samples (1.09:1 Cl/Br for MCS-BM), while a 1.39:1.0 Cl/ Br ratio (i.e., a chlorine-rich solid solution) is obtained for the SS sample, despite the 1:1 synthetic molar ratio of the starting reagents for the preparation of all samples. The MCS approach clearly provides superior ease and control of the composition of the solid solution compared to the SS approach, where the final solid product is driven thermodynamically, requiring one to adjust reactant concentrations in order to achieve a 1:1 synthetic molar ratio. Hence, these results demonstrate that this new solvent-free approach allows one to obtain a homogeneous solid solution using low- (HG) or high-energy (BM) mechanical force chemical synthesis.

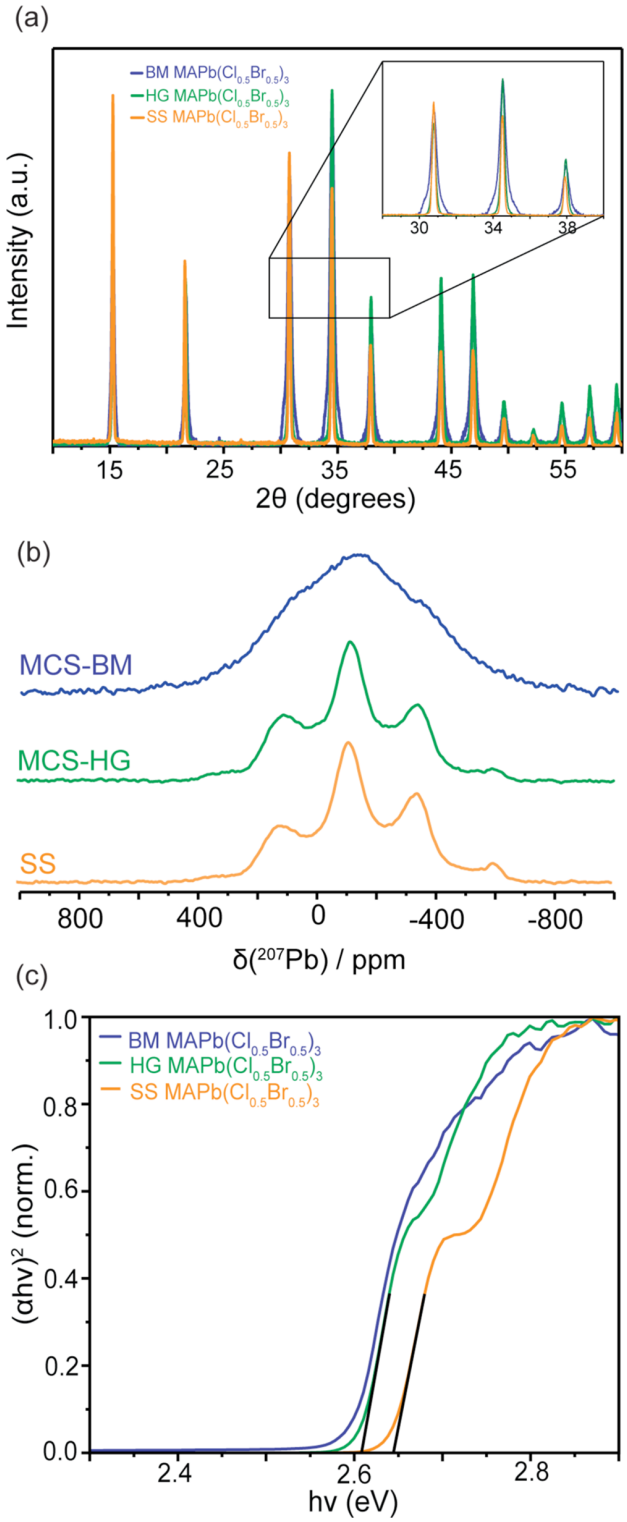

Figure 3.2: Comparison of data for the $MAPb(Cl_{0.50}Br_{0.50})_3$ MHP prepared using three distinct synthetic approaches: solvent synthesis and mechanochemical synthesis via hand grinding or ball milling. Powder XRD diffraction patterns (a), nonspinning ^{207}Pb NMR spectra, B_o = 21.1 T (b), and Tauc plots (c). The straight black lines indicate the bandgap energies at the intersection with the abscissa.

$MAPb(Br_xI_{1-x})_3$ Mechanochemical Synthesis.

To further investigate the application of the MCS synthetic approach, a 1:1 molar mixture of $MAPbBr_3$ and $MAPbI_3$ was prepared. To determine if the transition from phase-separated parent compounds to a randomly mixed solid solution can be visualized, a sample that was manually hand ground over a period of 2 h was characterized by NMR spectroscopy and by XRD, after 1 and 2 h of hand grinding (Figure 3.3). The halide ions begin to exchange, immediately forming a solid solution, and after 1 h of hand grinding, the sample is almost randomly mixed, although XRD and NMR data indicate some of the parent compounds also remain. HG for an additional hour completes the random ordering of the local $[PbBr_xI_{6-x}]^{4-}$ octahedra improving the quality of the solid solution as seen by the narrow diffraction peaks in the XRD data and by a Gaussian-like resonance in the NMR spectrum. The results indicate that the lower energy MCS-HG approach is effective in creating a single-phase MHP, with a binomial-like distribution similar to that obtained from a sample prepared by high-temperature solid-state synthesis.[53] Contrary to the case for the Cl/Br MHP system, we were unable to resolve multiple resonances for the Br/I system in the corresponding ^{207}Pb NMR spectra due to broadening, although spectra of the parent compounds indicate that substituting I with Br has the same effect as substituting Br with Cl: a shift to lower frequency.

Figures B.7 and B.8 show the powder XRD and DR data for the parent compounds and the final 50/50 Br/I MHP solid solution prepared by the MCS-HG technique. These data illustrate the benefit of side-stepping the thermodynamically driven solution process (i.e., avoiding the Br-rich phase)[53] with a stoichiometric MCS approach that yields an equal Br/I halide composition, based on XRD and $\delta_{cs}(^{207}Pb)$ data analysis.

3.3.2 MCS of FA-MHPs

Figure 3.4a,b shows pXRD and ^{207}Pb NMR results for the three parent perovskites and two MHPs, namely, $FAPb(Cl_{0.5}Br_{0.5})_3$ and $FAPb(Br_{0.5}I_{0.5})_3$ (see Figures B.13-B.18 for the complete data set for each series, along with the reflectance measurements). The

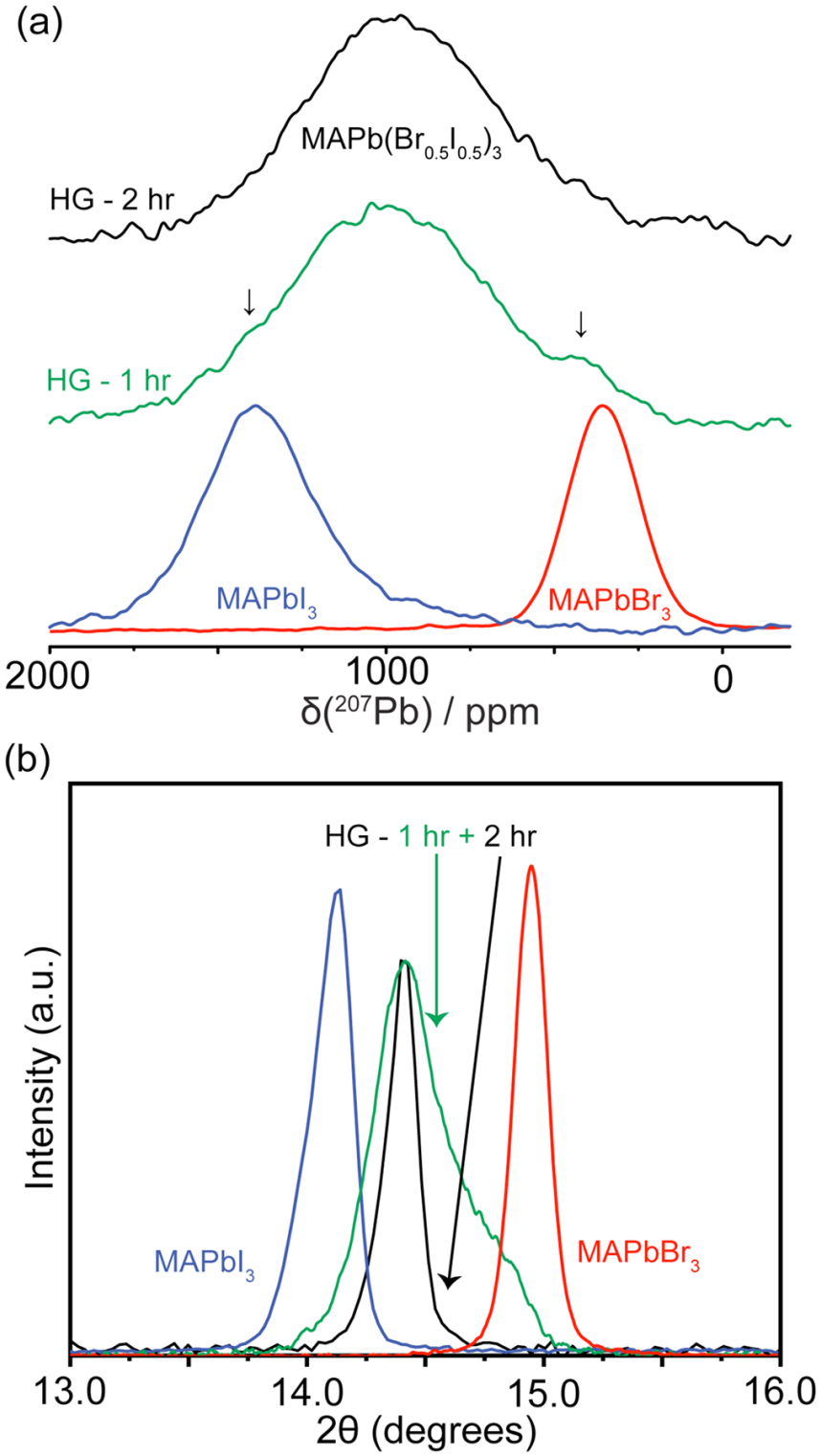

Figure 3.3: Nonspinning ^{207}Pb NMR (a, 7.05 T) and powder X-ray diffraction spectra (b) for $MAPbBr_3$ (red), $MAPbI_3$ (blue), and $MAPb(Br_{0.50}I_{0.50})_3$ (green 1 h, black 2 h). The MHP samples were prepared by the MCS-HG method for 1 and 2 h. The black arrows in the NMR spectra (a) indicate incomplete random halide mixing after 1 h (green trace), with small remnants of the parent compounds according to the NMR and XRD data (b, green arrow, 1 h). The black arrow in panel b indicates complete mixing of a single phase solid solution after 2 h.

^{207}Pb chemical shifts ($\delta_{cs}(^{207}\text{Pb})$) of the parent compounds shift to higher frequency as Cl is replaced by larger and less electronegative halides Br or I, spanning nearly 2000 ppm ($[PbCl_6]^{4-}$ to $[PbI_6]^{4-}$) as shown in Figure 3.4b. This observed behavior for $\delta_{cs}(^{207}\text{Pb})$ is similar to what has been previously reported for $MAPbX_3$ and other metal halides.[52,53,107,120]

Pure cubic phases are confirmed through pXRD for all MHPs prepared via MCS, and a Gaussian-like distribution of ^{207}Pb NMR resonances is observed, consistent with distinct local $[PbX_xX'_{6-x}]^{4-}$ chemical environments. ^{207}Pb NMR spectra at different fields for the HG-$FAPb(Cl_{0.5}Br_{0.5})_3$ mixture are shown in Figure B.19, revealing five resolved resonances that are assigned to $[PbCl_6]^{4-}$, $[PbCl_5Br]^{4-}$/$[PbCl_4Br_2]^{4-}$, $[PbCl_3Br_3]^{4-}$, $[PbCl_2Br_4]^{4-}$/$[PbClBr_5]^{4-}$, $[PbBr_6]^{4-}$; the assignment and fitting of experimental data acquired at 11.75 and 21.1 T are consistent with a binomial-like distribution for random Cl/Br mixing, as shown in Figure B.20b. Other mixtures in the series considered here also display binomial-like distributions based on their corresponding stoichiometric compositions (see Figure B.20).

Pb-207 NMR spectra for the BM-$FAPb(Br_{0.5}I_{0.5})_3$ sample acquired at 11.75 or 21.1 T were not resolved due to broadening; nevertheless, higher magnetic field strengths may improve the resolution and line shape as only slight evidence of multiple resonances begin to emerge at 21.1 T (Figure B.21).[121] The resonances for the I- and Br-rich MHPs lie between those for their respective parent perovskites and the 50/50 mixture (Figures B.18 and B.22), suggesting a statistical distribution of $[PbBr_xI_{6-x}]^{4-}$ populations. Thus, behavior similar to that observed for the HG Br/Cl MHP series is suggested, although in this case it was not possible to resolve individual sites.

Tracking the lattice constants and optical band gaps (extracted from pXRD and Tauc plots, respectively)[122] within these series of MCS-MHPs (Figure 3.5d,e) demonstrates a linear evolution with halide substitution from pure $FAPbCl_3$ to α- $FAPbI_3$, agreeing with Vegard's law.[116,123] The NMR spectroscopy and pXRD results (Figure 3.5) together indicate that the MCS route leads to homogeneous atomic-level solid solutions of FA-MHPs.

HG-MCS of $FAPbCl_3$ and $FAPbBr_3$ samples was sufficient to synthesize single pure

phases of $FAPb(Cl_xBr_{1-x})_3$ solid solutions, but for the $FAPb(Br_xI_{1-x})_3$ series, further treatment was required. A high temperature (200 °C, 1 h) annealing step was used to obtain the Br-rich (i.e., $FAPb(Br_{0.75}I_{0.25})_3$) composition (see Figures B.23 & B.24 for pXRD and ^{207}Pb NMR data taken at various steps of the HG process). This approach was unsuccessful for $FAPb(Br_{0.50}I_{0.50})_3$ and $FAPb(Br_{0.25}I_{0.75})_3$ and led to rapid decomposition of the materials or impure MHP products, or both (see Figure B.25). This is thought to be partially due to the decomposition of $FAPbI_3$ under thermal annealing[81] before a single MHP phase is formed, because pXRD indicates that PbI_2 was formed during the annealing process to form 50/50 Br/I or I-rich FA-MHPs. To avoid possible degradation or decomposition and to achieve single pure phases for $FAPb(Br_{0.50}I_{0.50})_3$ and $FAPb(Br_{0.25}I_{0.75})_3$ MHP solid solutions, a high-energy MCS method adopting BM was implemented (see Figures 3.2a and B.14). The BM method provides sufficient mechanical energy to form these phases within 30-60 min, at sample temperatures of approximately 50 °C, similar to that applied in other systems;[124] a detailed discussion of possible mechanisms of crystal formation through BM-MCS can be found elsewhere.[91,125–127] The success of BM near room temperature is mostly due to the high halide ion mobility in lead halide perovskite systems.[71,72,128] It has been shown previously that a solid-state synthesis method starting from parent compounds can be used to prepare a stoichiometric $MAPb(Br_{0.50}I_{0.50})_3$, but only after a heating protocol is applied, with partial sample decomposition observed at temperatures >250 °C.[53] The BM method described here may provide a versatile and highly adaptable approach for other hybrid perovskites, overcoming the need for any high temperature treatments.[88]

Figure 3.6 illustrates a comparison of pXRD, ^{207}Pb NMR, and reflectance data for $FAPb(Cl_{0.25}Br_{0.75})_3$ prepared using the MCS approach with those prepared using the SS method (see the Appendix B for experimental details). Both techniques yield nearly identical experimental results, with SS showing a slightly blue-shifted reflection edge. This observed shift is due to more Cl content (confirmed by EDX) versus the stoichiometric HG composition. Even though the synthetic loading for both samples is Br, 75% and Cl, 25%, the HG compound has an atomic % of Br/Cl of 3.06/1, while the SS compound is 2.4/1, demonstrating that fine control over composition is possible through MCS. The ^{207}Pb NMR spectra for both samples are similar, but the MCS

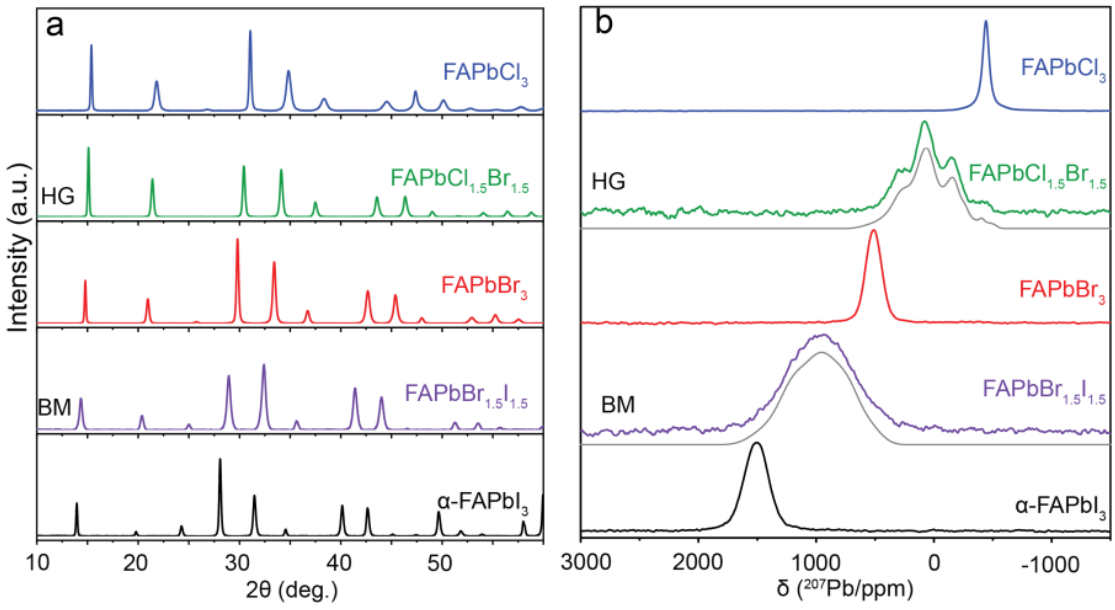

Figure 3.4: Powder XRD (a) and nonspinning ^{207}Pb NMR spectra (b, 11.75 T) structural characterization of parent ($FAPbX_3$) and mixed (HGFAPb($Cl_{0.5}Br_{0.5})_3$ and BM-FAPb$(Br_{0.5}I0._{0.5})_3$) perovskites (simulated spectra in gray).

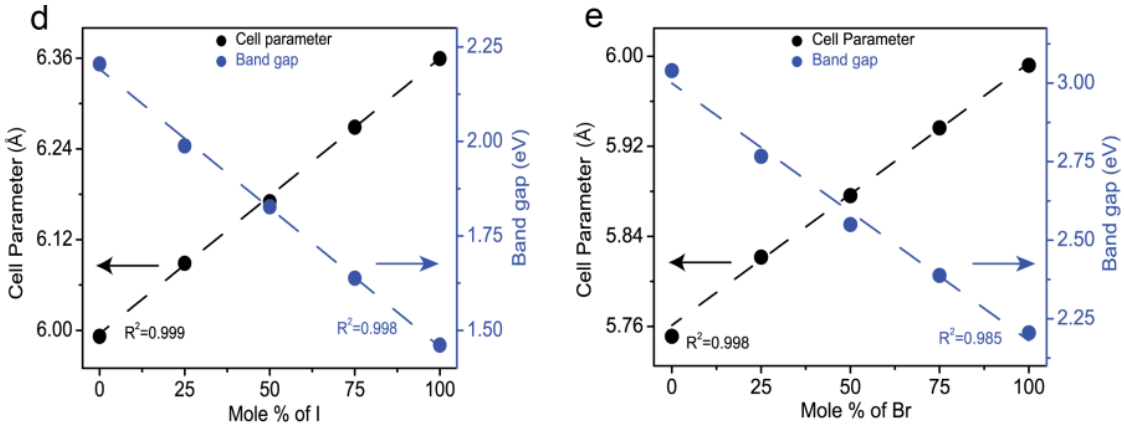

Figure 3.5: Unit cell and band gap (extracted from Tauc plots) properties follow a linear regression obeying Vegard's law (cell constants determined from XRD) with halide substitution for the BM-FAPb$(Br_xI_{1-x})_3$ series (d) and HG-FAPb$(Cl_xBr_{1-x})_3$ series (e).

approach provides spectra with higher resolution between different Pb coordination environments. In addition, the resonance centered at $\delta_{cs} \sim 100$ ppm (Figure 3.6c) is higher in intensity for the SS (vs MCS) sample corresponding to the higher Cl concentration, as confirmed by EDX.

Attempts to prepare a stoichiometric FAPb$(Br_{0.50}I_{0.50})_3$ using the SS route[?] as described for MAPb$(Br_{0.50}I_{0.50})_3$ were unsuccessful; pXRD and ^{207}Pb NMR data suggest that a Br-rich final product was obtained (Figure 3.7). Because of the distinct

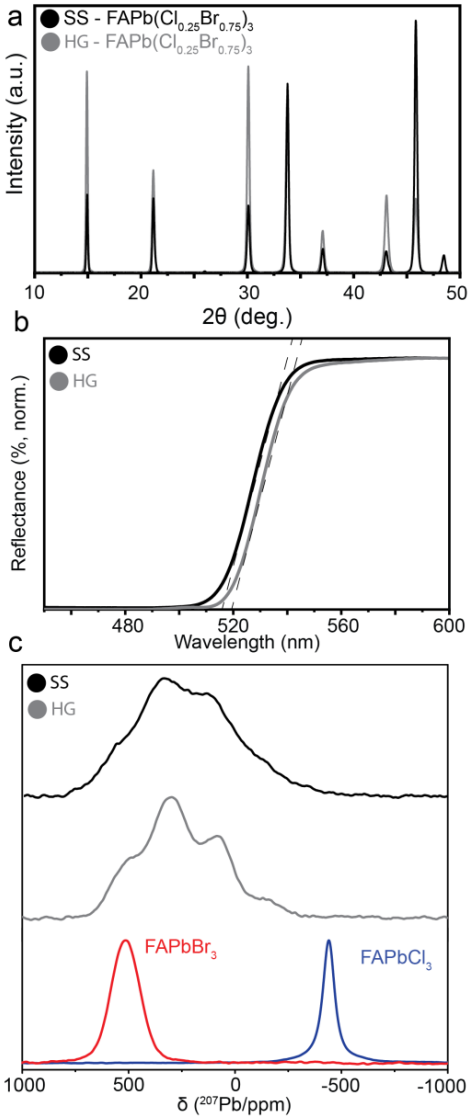

Figure 3.6: Structural characterization of $FAPb(Cl_{0.25}Br_{0.75})_3$ prepared by HG or SS approaches using pXRD (a), reflectance (b), and nonspinning ^{207}Pb NMR spectroscopy (c). NMR spectra were acquired at 11.75 T; the corresponding data for $FAPbCl_3$ and $FAPbBr_3$ are included for comparison.

thermodynamic and kinetic characteristic in forming MHPs through solvent synthesis versus MCS, the $FAPb(Br_{0.50}I_{0.50})_3$ mixture was achieved only using the latter (Figure 3.4), while the SS habitually led to a Br-rich phase.[?] In other words, preparing $FAPb(Br_{0.50}I_{0.50})_3$ by SS led to a product similar to the MCS of $FAPb(Br_{0.75}I_{0.25})_3$, as shown in Figure 3.7. Hence, the BM-MCS approach described above was developed to prepare these MHPs.

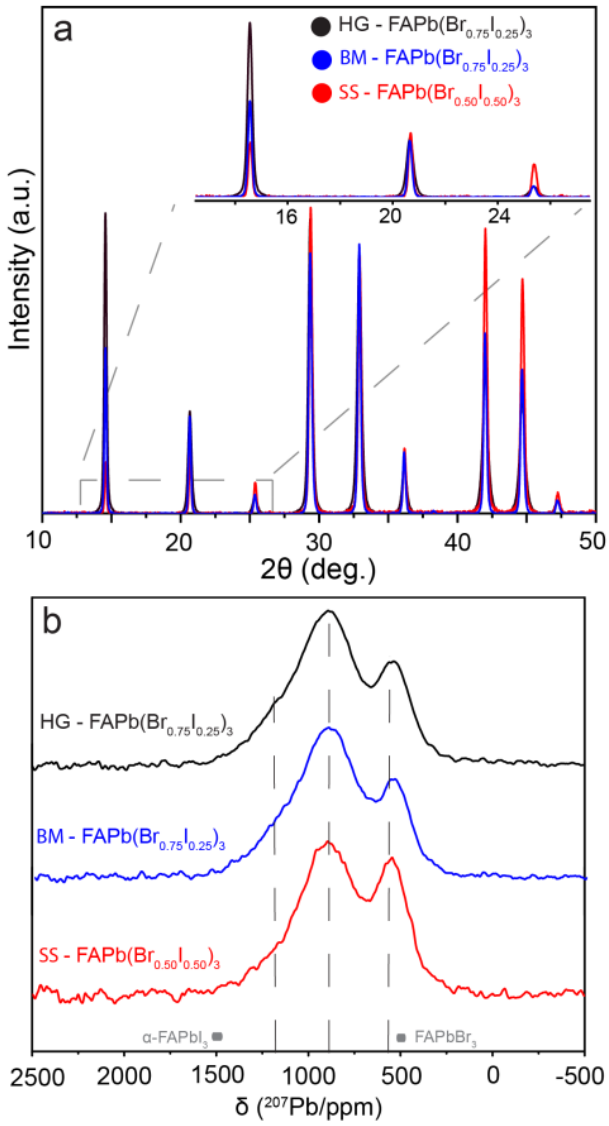

Figure 3.7: Comparison of the characteristics for HG-FAPb$(Br_{0.75}I_{0.25})_3$ (HG+1 h anneal), BM-FAPb$(Br_{0.75}I_{0.25})_3$, and SS attempt of FAPb$(Br_{0.50}I_{0.50})_3$ (by synthetic loading, see text). (a) pXRD pattern, (b) nonspinning ^{207}Pb NMR spectra (11.75 T).

3.4 Conclusions

For MA-based MHPs, we demonstrated the utility of the mechanochemical synthetic approach for the preparation of randomly ordered halides in single crystalline MA-MHP solid solutions with enhanced stoichiometric control compared to that achieved using traditional solvent synthesis protocols for the Br/Cl MA-MHPs. Increasing the grinding time and introducing a high-energy milling process maintains the long-range crystalline structure, but it can create a highly disordered local $[PbX_xX'_{6-x}]^{4-}$ octahedral environment due to rearrangements of bond lengths and angles about the

Pb center. Carefully tuning the compositions using the MCS-HG method, monitored by ^{207}Pb NMR spectroscopy, we identified seven distinct Pb octahedral chemical environments in the Br/Cl MA-MHPs, and demonstrated that the synthetic approach can be extended to other Pb-containing mixed-halide perovskites. The ^{207}Pb NMR spectra as well as the XRD results for the Cl/Br MHPs obtained using either solution synthesis or MCS of bulk samples indicate single-phase solid solutions with random halide distributions absent of amorphous or phase segregated domains. A stoichiometric $MAPb(Br_{0.50}I_{0.50})_3$ MHP, which has not been achieved previously using traditional room temperature solvent synthesis, was prepared at room temperature using the MCS-HG technique.

Similarly, we have presented a MCS approach for preparing FA-MHPs with fine control over halide compositions, including some not accessible by the traditional SS method. All MCS-MHPs show a solid solution behavior, with both crystal lattice constants and optical band gaps conforming to Vegard's law. Upon probing local Pb environments of the $[PbX_xX'_{6-x}]^{4-}$ octahedra in MHPs through ^{207}Pb NMR spectroscopy, distinct Pb chemical structures are identified, and their estimated populations adopt a binomial-like distribution, as expected for solid solutions. When SS results are compared to MCS for samples with similar final compositions, comparable structural and physical properties are determined; however, efficient control of stoichiometric synthesis for the MHPs studied here is better with the MCS method.

As recently reported for single halide perovskites prepared using a MCS approach, these materials lead to an improvement in device performance when compared to SS counterparts.[87,88,93] Hence, we hypothesize that the excellent compositional regulation in preparing FA-containing MHPs via MCS methods could provide superior control in optoelectronic properties leading to improved control in fabrication approaches.

This work paves the way to further understanding the underlying complex physical property behavior by providing atomic-level insights into these MHP solid solutions, targeting the development of highly efficient and stable devices. As perovskite materials continue to evolve for photovoltaic applications, careful characterization is essential. This study illustrates the importance of combining long-range diffraction based methods as well as probing the atomic-scale using NMR spectroscopy as key components

to unravel these intrinsically complex materials.

Chapter 4

Conclusion

In summary, there is no doubt that lead halide perovskite materials have proven real potential to be the next wave of low-cost and high-efficiency photovoltaics technology. Although most of the research efforts have been directed towards solar cell applications for LHPs, more work over recent years have been directed to almost all kinds of electronic and optoelectronic applications. Along with seeking breaking records of device performance especially of solar cells PCE, researchers continue to do fundamental studies to understand the reasons behind these intriguing intrinsic properties and how such material system is capable of delivering such outstanding performance records for various devices.

In this work, the original research conducted over the course of this thesis have resulted in solid results published already in respectful journals of materials chemistry and physical chemistry, contributing to the ever expanding span of knowledge for LHP materials.

Starting with LHP single crystals, solar cells have been realized on SCs for the first time through our collaborators at TUM. Despite the relatively poor performance for SC-based solar cells realized by the TUM group, it has been shown how in principle SCs used in many fundamental studies to understand the underlying physical properties in LHPs can also be used to fabricate devices and what are the predominant challenges and how they can be overcome in future research.

Next, we have shed light on one of the most concerning issues regarding LHPs which is the intrinsic stability of the workhorse compound of the LHP family, i.e., $MAPbI_3$. We started with single crystals of $MAPbI_3$ and exposed $MAPbI_3$ to various environmental conditions to simulate different circumstances of solar cell operations as well as other conditions to understand the exact degradation mechanisms of $MAPbI_3$, irrespective of the material (mainly films) preparation protocols, which are believed to be the main reasons behind various suggested degradation mechanisms reported in the literature. We have concluded that $MAPbI_3$ is intrinsically more stable than what was previously thought. We have identified all three possible degradation products, namely, $MAPbI_3$ monohydrate, dihydrate, and PbI_2. Comparing the products of the different experiments against the unique fingerprints of the four Pb-containing compounds, we identified with a great certainty the possible degradation pathways of $MAPbI_3$, with some routes being reversible (i.e., it is possible to recover $MAPbI_3$) and others which are not.

Next, we studied in detail two of the dominant systems in perovskite research, namely, $MAPbX_3$ and $FAPbX_3$. We introduced a simple, yet effective and scalable technique to prepare mixed halide perovskites through mechanochmeical synthesis with superior control over stoichiometry. Not only that, but we showed how mechanochemical synthesis enabled the access to some mixed halide stoichiometries not previously accessible through traditional solvent synthesis technique. Using a suite of characterization techniques including X-ray diffraction and solid state NMR spectroscopy (through our collaborators at the Department of Chemistry - University of Alberta) for studying long range as well as short/medium-range ordering in the materials of interest, respectively, we showed how mixed halide perovskite behave as a solid solution following Vegard's law with no evidence of phase segregation or persistent doping effects. Through ssNMR spectroscopy, advanced insights were inferred about these material systems, proving true atomic-scale halide mixing.

Future Research Directions

Despite the significance of the conclusions drawn from this work, we believe that there are still many directions to be explored in the exciting research field of halide perovskite materials.

In brief, we believe there is a considerable room for improvements in the area of SC-based PSCs. Developing techniques for growing single crystals with large diameters in the range of inches and with a few 100s of nm thickness is essential for enabling this technology. In addition, improving on the quality of metal contacts with SCs is vital for achieving the optimum performance out of these SCs.

We have shown how mechanochemically synthesized mixed halide perovskites are very comparable from the structure point of view to those prepared through traditional solvent synthesis routes. It remains to investigate how the quality of PSCs prepared using materials synthesized by MCS technique compare with respect to device performance and stability to those engineered following the solvent synthesis techniques.

Looking back, it is somehow mind-blowing how things rapidly progressed in the field of halide perovskites, especially when compared to other material systems which have been out there under research for decades, but never achieved what this exciting material system has accomplished in just a few years in terms of device performance, especially solar cell efficiency. It is certain that a brighter future is awaiting for the "Perovskite Era" as technology advances over the time with better in-depth understanding developing every day.

Bibliography

[1] Ansuman Halder, Devika Choudhury, Soham Ghosh, Anand S. Subbiah, and Shaibal K Sarkar. Exploring Thermochromic Behavior of Hydrated Hybrid Perovskites in Solar Cells. *The Journal of Physical Chemistry Letters*, 6(16):3180–3184, 2015.

[2] Abdelrahman M. Askar, Abhoy Karmakar, Guy M. Bernard, Michelle Ha, Victor V. Terskikh, Benjamin D. Wiltshire, Sahil Patel, Jonathan Fleet, Karthik Shankar, and Vladimir K. Michaelis. Composition-Tunable Formamidinium Lead Mixed Halide Perovskites via Solvent-Free Mechanochemical Synthesis: Decoding the Pb Environments Using Solid-State NMR Spectroscopy. *The Journal of Physical Chemistry Letters*, 9(0):2671–2677, 2018.

[3] G.A. Chamberlain. Organic solar cells: A review. *Solar Cells*, 8(1):47 – 83, 1983.

[4] Gordon J. Hedley, Arvydas Ruseckas, and Ifor D. W. Samuel. Light harvesting for organic photovoltaics. *Chemical Reviews*, 117(2):796–837, 2017.

[5] Jiawei Gong, K. Sumathy, Qiquan Qiao, and Zhengping Zhou. Review on dye-sensitized solar cells (dsscs): Advanced techniques and research trends. *Renewable and Sustainable Energy Reviews*, 68:234 – 246, 2017.

[6] Anders Hagfeldt, Gerrit Boschloo, Licheng Sun, Lars Kloo, and Henrik Pettersson. Dye-sensitized solar cells. *Chemical Reviews*, 110(11):6595–6663, 2010.

[7] Jiawei Gong, Jing Liang, and K. Sumathy. Review on dye-sensitized solar cells (DSSCs): Fundamental concepts and novel materials. *Renewable and Sustainable Energy Reviews*, 16(8):5848 – 5860, 2012.

[8] Hyekyoung Choi and Sohee Jeong. A review on eco-friendly quantum dot solar cells: Materials and manufacturing processes. *International Journal of Precision Engineering and Manufacturing-Green Technology*, 5(2):349–358, 2018.

[9] Graham H. Carey, Ahmed L. Abdelhady, Zhijun Ning, Susanna M. Thon, Osman M. Bakr, and Edward H. Sargent. Colloidal quantum dot solar cells. *Chemical Reviews*, 115(23):12732–12763, 2015.

[10] Green Martin A. The path to 25% silicon solar cell efficiency: History of silicon cell evolution. *Progress in Photovoltaics: Research and Applications*, 17(3):183–189, 2009.

[11] Tomas Leijtens, Giles E. Eperon, Nakita K. Noel, Severin N. Habisreutinger, Annamaria Petrozza, and Henry J. Snaith. Stability of metal halide perovskite solar cells. *Advanced Energy Materials*, 5(20):1500963, 2015.

[12] G Grancini, C Roldán-Carmona, I Zimmermann, E Mosconi, X Lee, D Martineau, S Narbey, F Oswald, F De Angelis, M Graetzel, and Mohammad Khaja Nazeeruddin. One-Year stable perovskite solar cells by 2D/3D interface engineering. *Nature Communications*, 8:15684, jun 2017.

[13] T. Stanley Cameron Osvald Knop Beverly R. Vincent, Katherine N. Robertson. Alkylammonium lead halides. Part 1. Isolated PbI_6^{4-} ions in $(CH_3NH_3)_4PbI_6{\cdot}2H_2O$. *Can. J. Chem*, (1042).

[14] Junichiro Mizusaki, Kimiyasu Arai, and Kazuo Fueki. Ionic conduction of the perovskite-type halides. *Solid State Ionics*, 11(3):203 – 211, 1983.

[15] J. W. Flocken, R. A. Guenther, J. R. Hardy, and L. L. Boyer. First-principles study of structural instabilities in halide-based perovskites: Competition between ferroelectricity and ferroelasticity. *Phys. Rev. B*, 31:7252–7260, 1985.

[16] Akihiro Kojima, Kenjiro Teshima, Yasuo Shirai, and Tsutomu Miyasaka. Organometal halide perovskites as visible-light sensitizers for photovoltaic cells. *Journal of the American Chemical Society*, 131(17):6050–6051, 2009. PMID: 19366264.

[17] S Ashhab, O Voznyy, S Hoogland, E H Sargent, and M E Madjet. Effect of disorder on transport properties in a tight-binding model for lead halide perovskites. *Scientific Reports*, 7(1):8902, 2017.

[18] Chi Kin Lo, Bhoj R. Gautam, Philipp Selter, Zilong Zheng, Stefan D. Oosterhout, Iordania Constantinou, Robert Knitsch, Rylan M. W. Wolfe, Xueping Yi, Jean-Luc Brédas, Franky So, Michael F. Toney, Veaceslav Coropceanu, Michael Ryan Hansen, Kenan Gundogdu, and John R. Reynolds. Every atom counts: Elucidating the fundamental impact of structural change in conjugated polymers for organic photovoltaics. *Chemistry of Materials*, 30(9):2995–3009, 2018.

[19] Koen Vandewal, Scott Himmelberger, and Alberto Salleo. Structural Factors That Affect the Performance of Organic Bulk Heterojunction Solar Cells. *Macromolecules*, 46(16):6379–6387, 2013.

[20] Nadja Giesbrecht, Johannes Schlipf, Irene Grill, Philipp Rieder, Vladimir Dyakonov, Thomas Bein, Achim Hartschuh, Peter Muller-Buschbaum, and Pablo Docampo. Single-crystal-like optoelectronic-properties of $MAPbI_3$ perovskite polycrystalline thin films. *J. Mater. Chem. A*, 6:4822–4828, 2018.

[21] Ramavath Babu, Lingamallu Giribabu, and Surya Prakash Singh. Recent advances in halide-based perovskite crystals and their optoelectronic applications. *Crystal Growth & Design*, 18(4):2645–2664, 2018.

[22] Jie Ding and Qingfeng Yan. Progress in organic-inorganic hybrid halide perovskite single crystal: growth techniques and applications. *Science China Materials*, 60(11):1063–1078, 2017.

[23] Yangyang Dang, Dianxing Ju, Lei Wang, and Xutang Tao. Recent progress in the synthesis of hybrid halide perovskite single crystals. *CrystEngComm*, 18:4476–4484, 2016.

[24] Makhsud I. Saidaminov, Ahmed L. Abdelhady, Giacomo Maculan, and Osman M. Bakr. Retrograde solubility of formamidinium and methylammonium lead halide perovskites enabling rapid single crystal growth. *Chem. Commun.*, 51:17658–17661, 2015.

[25] Makhsud I. Saidaminov, Ahmed L. Abdelhady, Banavoth Murali, Erkki Alarousu, Victor M. Burlakov, Wei Peng, Ibrahim Dursun, Lingfei Wang, Yao He, Giacomo Maculan, Alain Goriely, Tom Wu, Omar F. Mohammed, and Osman M. Bakr. High-quality bulk hybrid perovskite single crystals within minutes by inverse temperature crystallization. *Nature Communications*, 6(1):7586, 2015.

[26] Johannes Schlipf, Abdelrahman M Askar, Florian Pantle, Benjamin D Wiltshire, Anton Sura, Peter Schneider, Linus Huber, Karthik Shankar, and Peter Müller-Buschbaum. Top-Down Approaches Towards Single Crystal Perovskite Solar Cells. *Scientific Reports*, 8(1):4906, 2018.

[27] Aurélien M. A. Leguy, Yinghong Hu, Mariano Campoy-Quiles, M. Isabel Alonso, Oliver J. Weber, Pooya Azarhoosh, Mark van Schilfgaarde, Mark T. Weller, Thomas Bein, Jenny Nelson, Pablo Docampo, and Piers R. F. Barnes. Reversible Hydration of $CH_3NH_3PbI_3$ in Films, Single Crystals, and Solar Cells. *Chemistry of Materials*, 27(9):3397–3407, 2015.

[28] Mahesh K. Gangishetty, Robert W. J. Scott, and Timothy L. Kelly. Effect of relative humidity on crystal growth, device performance and hysteresis in planar heterojunction perovskite solar cells. *Nanoscale*, 8:6300–6307, 2016.

[29] Hao Gao, Chunxiong Bao, Faming Li, Tao Yu, Jie Yang, Weidong Zhu, Xiaoxin Zhou, Gao Fu, and Zhigang Zou. Nucleation and Crystal Growth of Organic Inorganic Lead Halide Perovskites under Different Relative Humidity. *ACS Applied Materials & Interfaces*, 7(17):9110–9117, 2015.

[30] Huanping Zhou, Qi Chen, Gang Li, Song Luo, Tze-bing Song, Hsin-Sheng Duan, Ziruo Hong, Jingbi You, Yongsheng Liu, and Yang Yang. Interface engineering of highly efficient perovskite solar cells. *Science*, 345(6196):542–546, 2014.

[31] Jingbi You, Yang (Michael) Yang, Ziruo Hong, Tze-Bin Song, Lei Meng, Yongsheng Liu, Chengyang Jiang, Huanping Zhou, Wei-Hsuan Chang, Gang Li, and Yang Yang. Moisture assisted perovskite film growth for high performance solar cells. *Applied Physics Letters*, 105(18):183902, 2014.

[32] Taame Abraha Berhe, Wei-Nien Su, Ching-Hsiang Chen, Chun-Jern Pan, Ju-Hsiang Cheng, Hung-Ming Chen, Meng-Che Tsai, Liang-Yih Chen, Amare Aregahegn

Dubale, and Bing-Joe Hwang. Organometal halide perovskite solar cells: degradation and stability. *Energy Environ. Sci.*, 9:323–356, 2016.

[33] Long Hu, Gang Shao, Tao Jiang, Dengbing Li, Xinlin Lv, Hongya Wang, Xinsheng Liu, Haisheng Song, Jiang Tang, and Huan Liu. Investigation of the Interaction between Perovskite Films with Moisture via in Situ Electrical Resistance Measurement. *ACS Applied Materials & Interfaces*, 7(45):25113–25120, 2015.

[34] Dan Li, Simon A. Bretschneider, Victor W. Bergmann, Ilka M. Hermes, Julian Mars, Alexander Klasen, Hao Lu, Wolfgang Tremel, Markus Mezger, Hans-Jürgen Butt, Stefan A. L. Weber, and Rüdiger Berger. Humidity-Induced Grain Boundaries in $MAPbI_3$ Perovskite Films. *The Journal of Physical Chemistry C*, 120(12):6363–6368, 2016.

[35] Youzhen Li, Xuemei Xu, Chenggong Wang, Congcong Wang, Fangyan Xie, Junliang Yang, and Yongli Gao. Degradation by exposure of coevaporated $CH_3NH_3PbI_3$ thin films. *The Journal of Physical Chemistry C*, 119(42):23996–24002, 2015.

[36] Chuan-Jia Tong, Wei Geng, Zhen-Kun Tang, Chi-Yung Yam, Xiao-Li Fan, Jiang Liu, Woon-Ming Lau, and Li-Min Liu. Uncovering the veil of the degradation in perovskite $CH_3NH_3PbI_3$ upon humidity exposure: A first-principles study. *The Journal of Physical Chemistry Letters*, 6(16):3289–3295, 2015.

[37] Jinli Yang, Braden D. Siempelkamp, Dianyi Liu, and Timothy L. Kelly. Investigation of $CH_3NH_3PbI_3$ degradation rates and mechanisms in controlled humidity environments using in situ techniques. *ACS Nano*, 9(2):1955–1963, 2015.

[38] Joseph S. Manser, Makhsud I. Saidaminov, Jeffrey A. Christians, Osman M. Bakr, and Prashant V. Kamat. Making and breaking of lead halide perovskites. *Accounts of Chemical Research*, 49(2):330–338, 2016.

[39] Nam-Gyu Park. Perovskite solar cells: An emerging photovoltaic technology. *Materials Today*, 18(2):65 – 72, 2015.

[40] Jun Hong Noh, Sang Hyuk Im, Jin Hyuck Heo, Tarak N. Mandal, and Sang Il Seok. Chemical Management for Colorful, Efficient, and Stable Inorganic–Organic Hybrid Nanostructured Solar Cells. *Nano Letters*, 13(4):1764–1769, 2013.

[41] Alla Arakcheeva, Dmitry Chernyshov, Massimo Spina, László Forró, and Endre Horváth. $CH_3NH_3PbI_3$: precise structural consequences of water absorption at ambient conditions. *Acta Crystallographica Section B*, 72(5):716–722, 2016.

[42] Masaki Shirayama, Masato Kato, Tetsuhiko Miyadera, Takeshi Sugita, Takemasa Fujiseki, Shota Hara, Hideyuki Kadowaki, Daisuke Murata, Masayuki Chikamatsu, and Hiroyuki Fujiwara. Degradation mechanism of $CH_3NH_3PbI_3$ perovskite materials upon exposure to humid air. *Journal of Applied Physics*, 119(11):115501, 2016.

[43] Yu Han, Steffen Meyer, Yasmina Dkhissi, Karl Weber, Jennifer M. Pringle, Udo Bach, Leone Spiccia, and Yi-Bing Cheng. Degradation observations of encapsulated planar $CH_3NH_3PbI_3$ perovskite solar cells at high temperatures and humidity. *J. Mater. Chem. A*, 3:8139–8147, 2015.

[44] Guangda Niu, Wenzhe Li, Fanqi Meng, Liduo Wang, Haopeng Dong, and Yong Qiu. Study on the stability of $CH_3NH_3PbI_3$ films and the effect of post-modification by aluminum oxide in all-solid-state hybrid solar cells. *J. Mater. Chem. A*, 2:705–710, 2014.

[45] Xu Dong, Xiang Fang, Minghang Lv, Bencai Lin, Shuai Zhang, Jianning Ding, and Ningyi Yuan. Improvement of the humidity stability of organic-inorganic perovskite solar cells using ultrathin Al_2O_3 layers prepared by atomic layer deposition. *J. Mater. Chem. A*, 3:5360–5367, 2015.

[46] Bekele Hailegnaw, Saar Kirmayer, Eran Edri, Gary Hodes, and David Cahen. Rain on methylammonium lead iodide based perovskites: Possible environmental effects of perovskite solar cells. *The Journal of Physical Chemistry Letters*, 6(9):1543–1547, 2015.

[47] Jeffrey A. Christians, Pierre A. Miranda Herrera, and Prashant V. Kamat. Transformation of the excited state and photovoltaic efficiency of $CH_3NH_3PbI_3$ perovskite upon controlled exposure to humidified air. *Journal of the American Chemical Society*, 137(4):1530–1538, 2015.

[48] Klaus Horchler Bernd Wrackmeyer. ^{207}Pb-NMR Parameters. volume 22 of *Annual Reports on NMR Spectroscopy*, pages 249 – 306. Academic Press, 1990.

[49] A. E. Aliev and R. V. Law. Solid-state NMR spectroscopy. In *Nuclear Magnetic Resonance: Volume 38*, volume 38, pages 271–321. The Royal Society of Chemistry, 2009.

[50] Brandon J. Greer, Vladimir K. Michaelis, Michael J. Katz, Daniel B. Leznoff, Georg Schreckenbach, and Scott Kroeker. Characterising Lone-Pair Activity of Lead(II) by ^{207}Pb. *Chemistry – A European Journal*, 17(13):3609–3618, 2011.

[51] R. E. Taylor, Peter A. Beckmann, Shi Bai, and C. Dybowski. ^{127}I and ^{207}Pb Solid-State NMR Spectroscopy and Nuclear Spin Relaxation in PbI_2: A Preliminary Study. *The Journal of Physical Chemistry C*, 118(17):9143–9153, 2014.

[52] Claire Roiland, Gaelle Trippe-Allard, Khaoula Jemli, Bruno Alonso, Jean-Claude Ameline, Regis Gautier, Thierry Bataille, Laurent Le Polles, Emmanuelle Deleporte, Jacky Even, and Claudine Katan. Multinuclear nmr as a tool for studying local order and dynamics in $CH_3NH_3PbI_3$ (X = Cl, Br, I) hybrid perovskites. *Phys. Chem. Chem. Phys.*, 18:27133–27142, 2016.

[53] Bryan A. Rosales, Long Men, Sarah D. Cady, Michael P. Hanrahan, Aaron J. Rossini, and Javier Vela. Persistent Dopants and Phase Segregation in Organolead Mixed-Halide Perovskites. *Chemistry of Materials*, 28(19):6848–6859, 2016.

[54] Mark T. Weller, Oliver J. Weber, Paul F. Henry, Antonietta M. Di Pumpo, and Thomas C. Hansen. Complete structure and cation orientation in the perovskite photovoltaic methylammonium lead iodide between 100 and 352 K. *Chem. Commun.*, 51:4180–4183, 2015.

[55] Gregory H. Imler, Xia Li, Bolei Xu, Graham E. Dobereiner, Hai-Lung Dai, Yi Rao, and Bradford B. Wayland. Solid state transformation of the crystalline monohydrate $(CH_3NH_3)PbI_3(H_2O)$ to the $(CH_3NH_3)PbI_3$ perovskite. *Chem. Commun.*, 51:11290–11292, 2015.

[56] Atsushi Wakamiya, Masaru Endo, Takahiro Sasamori, Norihiro Tokitoh, Yuhei Ogomi, Shuzi Hayase, and Yasujiro Murata. Reproducible Fabrication of Efficient Perovskite-based Solar Cells: X-ray Crystallographic Studies on the Formation of $CH_3NH_3PbI_3$ Layers. *Chemistry Letters*, 43(5):711–713, 2014.

[57] Jiangtao Zhao, Bing Cai, Zhenlin Luo, Yongqi Dong, Yi Zhang, Han Xu, Bin Hong, Yuanjun Yang, Liangbin Li, Wenhua Zhang, and Chen Gao. Investigation of the Hydrolysis of Perovskite Organometallic Halide $CH_3NH_3PbI_3$ in Humidity Environment. *Scientific Reports*, 6:21976, 2016.

[58] Noriko Onoda-Yamamuro, Takasuke Matsuo, and Hiroshi Suga. Calorimetric and IR spectroscopic studies of phase transitions in methylammonium trihalogenoplumbates (II)†". *Journal of Physics and Chemistry of Solids*, 51(12):1383 – 1395, 1990.

[59] Federico Brivio, Jarvist M. Frost, Jonathan M. Skelton, Adam J. Jackson, Oliver J. Weber, Mark T. Weller, Alejandro R. Goñi, Aurélien M. A. Leguy, Piers R. F. Barnes, and Aron Walsh. Lattice dynamics and vibrational spectra of the orthorhombic, tetragonal, and cubic phases of methylammonium lead iodide. *Phys. Rev. B*, 92:144308, 2015.

[60] Stranks Samuel D., Nayak Pabitra K., Zhang Wei, Stergiopoulos Thomas, and Snaith Henry J. Formation of Thin Films of Organic–Inorganic Perovskites for High-Efficiency Solar Cells. *Angewandte Chemie International Edition*, 54(11):3240–3248, 2015.

[61] Andrew Barnabas Wong, Minliang Lai, Samuel Wilson Eaton, Yi Yu, Elbert Lin, Letian Dou, Anthony Fu, and Peidong Yang. Growth and Anion Exchange Conversion of $CH_3NH_3PbX_3$ Nanorod Arrays for Light-Emitting Diodes. *Nano Letters*, 15(8):5519–5524, 2015.

[62] Hairen Tan, Ankit Jain, Oleksandr Voznyy, Xinzheng Lan, F. Pelayo García de Arquer, James Z. Fan, Rafael Quintero-Bermudez, Mingjian Yuan, Bo Zhang, Yicheng Zhao, Fengjia Fan, Peicheng Li, Li Na Quan, Yongbiao Zhao, Zheng-Hong Lu, Zhenyu Yang, Sjoerd Hoogland, and Edward H. Sargent. Efficient and stable solution-processed planar perovskite solar cells via contact passivation. *Science*, 2017.

[63] Giles E. Eperon, Tomas Leijtens, Kevin A. Bush, Rohit Prasanna, Thomas Green, Jacob Tse-Wei Wang, David P. McMeekin, George Volonakis, Rebecca L. Milot, Richard May, Axel Palmstrom, Daniel J. Slotcavage, Rebecca A. Belisle, Jay B.

Patel, Elizabeth S. Parrott, Rebecca J. Sutton, Wen Ma, Farhad Moghadam, Bert Conings, Aslihan Babayigit, Hans-Gerd Boyen, Stacey Bent, Feliciano Giustino, Laura M. Herz, Michael B. Johnston, Michael D. McGehee, and Henry J. Snaith. Perovskite-perovskite tandem photovoltaics with optimized bandgaps. *Science*, 2016.

[64] Dong Myung Jang, Kidong Park, Duk Hwan Kim, Jeunghee Park, Fazel Shojaei, Hong Seok Kang, Jae-Pyung Ahn, Jong Woon Lee, and Jae Kyu Song. Reversible halide exchange reaction of organometal trihalide perovskite colloidal nanocrystals for full-range band gap tuning. *Nano Letters*, 15(8):5191–5199, 2015.

[65] Norman Pellet, Joël Teuscher, Joachim Maier, and Michael Grätzel. Transforming hybrid organic inorganic perovskites by rapid halide exchange. *Chemistry of Materials*, 27(6):2181–2188, 2015.

[66] Silvia Colella, Edoardo Mosconi, Paolo Fedeli, Andrea Listorti, Francesco Gazza, Fabio Orlandi, Patrizia Ferro, Tullo Besagni, Aurora Rizzo, Gianluca Calestani, Giuseppe Gigli, Filippo De Angelis, and Roberto Mosca. $MAPbI_{3-x}Cl_x$ Mixed Halide Perovskite for Hybrid Solar Cells: The Role of Chloride as Dopant on the Transport and Structural Properties. *Chemistry of Materials*, 25(22):4613–4618, 2013.

[67] Edoardo Mosconi and Filippo De Angelis. Mobile ions in organohalide perovskites: Interplay of electronic structure and dynamics. *ACS Energy Letters*, 1(1):182–188, 2016.

[68] Federico Brivio, Clovis Caetano, and Aron Walsh. Thermodynamic Origin of Photoinstability in the $CH_3NH_3Pb(I_{1-x}Br_x)_3$ Hybrid Halide Perovskite Alloy. *The Journal of Physical Chemistry Letters*, 7(6):1083–1087, 2016.

[69] Olivia Hentz, Zhibo Zhao, and Silvija Gradečak. Impacts of ion segregation on local optical properties in mixed halide perovskite films. *Nano Letters*, 16(2):1485–1490, 2016.

[70] Eric T. Hoke, Daniel J. Slotcavage, Emma R. Dohner, Andrea R. Bowring, Hemamala I. Karunadasa, and Michael D. McGehee. Reversible photo-induced trap for-

mation in mixed-halide hybrid perovskites for photovoltaics. *Chem. Sci.*, 6:613–617, 2015.

[71] Seog Joon Yoon, Sergiu Draguta, Joseph S. Manser, Onise Sharia, William F. Schneider, Masaru Kuno, and Prashant V. Kamat. Tracking iodide and bromide ion segregation in mixed halide lead perovskites during photoirradiation. *ACS Energy Letters*, 1(1):290–296, 2016.

[72] Seog Joon Yoon, Masaru Kuno, and Prashant V. Kamat. Shift Happens. How Halide Ion Defects Influence Photoinduced Segregation in Mixed Halide Perovskites. *ACS Energy Letters*, 2(7):1507–1514, 2017.

[73] Fabian C. Hanusch, Erwin Wiesenmayer, Eric Mankel, Andreas Binek, Philipp Angloher, Christina Fraunhofer, Nadja Giesbrecht, Johann M. Feckl, Wolfram Jaegermann, Dirk Johrendt, Thomas Bein, and Pablo Docampo. Efficient planar heterojunction perovskite solar cells based on formamidinium lead bromide. *The Journal of Physical Chemistry Letters*, 5(16):2791–2795, 2014.

[74] Pellet Norman, Gao Peng, Gregori Giuliano, Yang Tae-Youl, Nazeeruddin Mohammad K., Maier Joachim, and Grätzel Michael. Mixed-Organic-Cation Perovskite Photovoltaics for Enhanced Solar-Light Harvesting. *Angewandte Chemie International Edition*, 53(12):3151–3157, 2014.

[75] Rehman Waqaas, Milot Rebecca L., Eperon Giles E., Wehrenfennig Christian, Boland Jessica L., Snaith Henry J., Johnston Michael B., and Herz Laura M. Charge-Carrier Dynamics and Mobilities in Formamidinium Lead Mixed-Halide Perovskites. *Advanced Materials*, 27(48):7938–7944, 2015.

[76] Ayan A. Zhumekenov, Makhsud I. Saidaminov, Md Azimul Haque, Erkki Alarousu, Smritakshi Phukan Sarmah, Banavoth Murali, Ibrahim Dursun, Xiao-He Miao, Ahmed L. Abdelhady, Tom Wu, Omar F. Mohammed, and Osman M. Bakr. Formamidinium lead halide perovskite crystals with unprecedented long carrier dynamics and diffusion length. *ACS Energy Letters*, 1(1):32–37, 2016.

[77] Giles E. Eperon, Samuel D. Stranks, Christopher Menelaou, Michael B. Johnston, Laura M. Herz, and Henry J. Snaith. Formamidinium lead trihalide: a broadly

tunable perovskite for efficient planar heterojunction solar cells. *Energy Environ. Sci.*, 7:982–988, 2014.

[78] David P. McMeekin, Golnaz Sadoughi, Waqaas Rehman, Giles E. Eperon, Michael Saliba, Maximilian T. Hörantner, Amir Haghighirad, Nobuya Sakai, Lars Korte, Bernd Rech, Michael B. Johnston, Laura M. Herz, and Henry J. Snaith. A mixed-cation lead mixed-halide perovskite absorber for tandem solar cells. *Science*, 351(6269):151–155, 2016.

[79] Mark T. Weller, Oliver J. Weber, Jarvist M. Frost, and Aron Walsh. Cubic Perovskite Structure of Black Formamidinium Lead Iodide, α-$[HC(NH_2)_2]PbI_3$, at 298 K. *The Journal of Physical Chemistry Letters*, 6(16):3209–3212, 2015.

[80] Andreas Binek, Fabian C. Hanusch, Pablo Docampo, and Thomas Bein. Stabilization of the trigonal high-temperature phase of formamidinium lead iodide. *The Journal of Physical Chemistry Letters*, 6(7):1249–1253, 2015.

[81] Vanessa L Pool, Benjia Dou, Douglas G Van Campen, Talysa R Klein-Stockert, Frank S Barnes, Sean E Shaheen, Md I Ahmad, Maikel F A M van Hest, and Michael F Toney. Thermal engineering of $FAPbI_3$ perovskite material via radiative thermal annealing and in situ XRD. *Nature Communications*, 8:14075, 2017.

[82] Dong Myung Jang, Duk Hwan Kim, Kidong Park, Jeunghee Park, Jong Woon Lee, and Jae Kyu Song. Ultrasound synthesis of lead halide perovskite nanocrystals. *J. Mater. Chem. C*, 4:10625–10629, 2016.

[83] Mark C. Weidman, Michael Seitz, Samuel D. Stranks, and William A. Tisdale. Highly tunable colloidal perovskite nanoplatelets through variable cation, metal, and halide composition. *ACS Nano*, 10(8):7830–7839, 2016.

[84] Wang Jialin, Peng Jiajun, Sun Yong, Liu Xiaoyu, Chen Yani, and Liang Ziqi. $FAPbCl_3$ Perovskite as Alternative Interfacial Layer for Highly Efficient and Stable Polymer Solar Cells. *Advanced Electronic Materials*, 2(11):1600329, 2016.

[85] K. Hills-Kimball, Y. Nagaoka, C. Cao, E. Chaykovsky, and O. Chen. Synthesis of formamidinium lead halide perovskite nanocrystals through solid-liquid-solid cation exchange. *J. Mater. Chem. C*, 5:5680–5684, 2017.

[86] Duong Nguyen Minh, Juwon Kim, Jinho Hyon, Jae Hyun Sim, Haneen H. Sowlih, Chunhee Seo, Jihye Nam, Sangwon Eom, Soyeon Suk, Sangheon Lee, Eunjoo Kim, and Youngjong Kang. Room-temperature synthesis of widely tunable formamidinium lead halide perovskite nanocrystals. *Chemistry of Materials*, 29(13):5713–5719, 2017.

[87] D. Prochowicz, M. Franckevicius, A. M. Cieslak, S. M. Zakeeruddin, M. Gratzel, and J. Lewinski. Mechanosynthesis of the hybrid perovskite $CH_3NH_3PbI_3$: characterization and the corresponding solar cell efficiency. *J. Mater. Chem. A*, 3:20772–20777, 2015.

[88] D. Prochowicz, P. Yadav, M. Saliba, M. Saski, S. M. Zakeeruddin, J. Lewinski, and M. Gratzel. Mechanosynthesis of pure phase mixed-cation $MA_xFA_{1-x}PbI_3$ hybrid perovskites: photovoltaic performance and electrochemical properties. *Sustainable Energy Fuels*, 1:689–693, 2017.

[89] Ahmed Mourtada Elseman, Mohamed M. Rashad, and Ali M. Hassan. Easily attainable, efficient solar cell with mass yield of nanorod single-crystalline organo-metal halide perovskite based on a ball milling technique. *ACS Sustainable Chemistry & Engineering*, 4(9):4875–4886, 2016.

[90] Atanu Jana, Mona Mittal, Aayushi Singla, and Sameer Sapra. Solvent-free, mechanochemical syntheses of bulk trihalide perovskites and their nanoparticles. *Chem. Commun.*, 53:3046–3049, 2017.

[91] Zhi-Yuan Zhu, Qi-Qi Yang, Lin-Feng Gao, Lei Zhang, An-Ye Shi, Chun-Lin Sun, Qiang Wang, and Hao-Li Zhang. Solvent-free mechanosynthesis of composition-tunable cesium lead halide perovskite quantum dots. *The Journal of Physical Chemistry Letters*, 8(7):1610–1614, 2017.

[92] Pal Provas, Saha Sujoy, Banik Ananya, Sarkar Arka, and Biswas Kanishka. All-Solid-State Mechanochemical Synthesis and Post-Synthetic Transformation of Inorganic Perovskite-type Halides. *Chemistry – A European Journal*, 24(8):1811–1815, 2018.

[93] Daniel Prochowicz, Pankaj Yadav, Michael Saliba, Marcin Saski, Shaik M. Zakeeruddin, Janusz Lewiński, and Michael Grätzel. Reduction in the Interfacial

Trap Density of Mechanochemically Synthesized $MAPbI_3$. *ACS Applied Materials & Interfaces*, 9(34):28418–28425, 2017.

[94] Dominik J. Kubicki, Daniel Prochowicz, Albert Hofstetter, Shaik M. Zakeeruddin, Michael Grätzel, and Lyndon Emsley. Phase Segregation in Cs-, Rb- and K-Doped Mixed-Cation $(MA)_x(FA)_{1-x}PbI_3$ Hybrid Perovskites from Solid-State NMR. *Journal of the American Chemical Society*, 139(40):14173–14180, 2017.

[95] Maria Klimakow, Peter Klobes, Andreas F. Thünemann, Klaus Rademann, and Franziska Emmerling. Mechanochemical synthesis of metal-organic frameworks: A fast and facile approach toward quantitative yields and high specific surface areas. *Chemistry of Materials*, 22(18):5216–5221, 2010.

[96] Friščić Tomislav. *Metal-Organic Frameworks: Mechanochemical Synthesis Strategies*, pages 1–19. American Cancer Society, 2014.

[97] Niraj K. Singh, Meenakshi Hardi, and Viktor P. Balema. Mechanochemical synthesis of an yttrium based metal-organic framework. *Chem. Commun.*, 49:972–974, 2013.

[98] Yating Zhou, Fang Guo, Colan E. Hughes, Duncan L. Browne, Thomas R. Peskett, and Kenneth D. M. Harris. Discovery of New Metastable Polymorphs in a Family of Urea Co-Crystals by Solid-State Mechanochemistry. *Crystal Growth & Design*, 15(6):2901–2907, 2015.

[99] Dritan Hasa, Eugenia Miniussi, and William Jones. Mechanochemical Synthesis of Multicomponent Crystals: One Liquid for One Polymorph? A Myth to Dispel. *Crystal Growth & Design*, 16(8):4582–4588, 2016.

[100] Franziska Fischer, Adrian Heidrich, Sebastian Greiser, Sigrid Benemann, Klaus Rademann, and Franziska Emmerling. Polymorphism of mechanochemically synthesized cocrystals: A case study. *Crystal Growth & Design*, 16(3):1701–1707, 2016.

[101] Chunping Xu, Sudipta De, Alina M. Balu, Manuel Ojeda, and Rafael Luque. Mechanochemical synthesis of advanced nanomaterials for catalytic applications. *Chem. Commun.*, 51:6698–6713, 2015.

[102] Hao Wu and Qiang Li. Application of mechanochemical synthesis of advanced materials. *Journal of Advanced Ceramics*, 1(2):130–137, 2012.

[103] Cecil Dybowski, Matthew L. Smith, Mark A. Hepp, Edward J. Gaffney, Guenther Neue, and Dale L. Perry. ^{207}Pb NMR Chemical-Shift Tensors of the Lead (II) Halides and the Lead (II) Hydroxyhalides. *Appl. Spectrosc.*, 52(3):426–429, 1998.

[104] Abdelrahman M. Askar, Guy M. Bernard, Benjamin Wiltshire, Karthik Shankar, and Vladimir K. Michaelis. Multinuclear Magnetic Resonance Tracking of Hydro, Thermal, and Hydrothermal Decomposition of $CH_3NH_3PbI_3$. *The Journal of Physical Chemistry C*, 121(2):1013–1024, 2017.

[105] Application of ^{207}Pb NMR parameters. volume 47 of *Annual Reports on NMR Spectroscopy*, pages 1 – 37. Academic Press, 2002.

[106] A. E. Aliev and R. V. Law. Chapter 7 Solid state NMR spectroscopy. In *Nuclear Magnetic Resonance: Volume 43*, volume 43, pages 286–344. The Royal Society of Chemistry, 2014.

[107] Bryan A. Rosales, Michael P. Hanrahan, Brett W. Boote, Aaron J. Rossini, Emily A. Smith, and Javier Vela. Lead Halide Perovskites: Challenges and Opportunities in Advanced Synthesis and Spectroscopy. *ACS Energy Letters*, 2(4):906–914, 2017.

[108] Ioannis Lignos, Loredana Protesescu, Dilara Börte Emiroglu, Richard Maceiczyk, Simon Schneider, Maksym V. Kovalenko, and Andrew J. deMello. Unveiling the Shape Evolution and Halide-Ion-Segregation in Blue-Emitting Formamidinium Lead Halide Perovskite Nanocrystals Using an Automated Microfluidic Platform. *Nano Letters*, 18(2):1246–1252, 2018.

[109] Tom Baikie, Nathan S. Barrow, Yanan Fang, Philip J. Keenan, Peter R. Slater, Ross O. Piltz, Matthias Gutmann, Subodh G. Mhaisalkar, and Tim J. White. A combined single crystal neutron/X-ray diffraction and solid-state nuclear magnetic resonance study of the hybrid perovskites $CH_3NH_3PbX_3$ (X = I, Br and Cl). *J. Mater. Chem. A*, 3:9298–9307, 2015.

[110] Misra Ravi K., Ciammaruchi Laura, Aharon Sigalit, Mogilyansky Dmitry, Etgar Lioz, Visoly-Fisher Iris, and Katz Eugene A. Effect of halide composition on

the photochemical stability of perovskite photovoltaic materials. *ChemSusChem*, 9(18):2572–2577, 2016.

[111] Waqaas Rehman, David P. McMeekin, Jay B. Patel, Rebecca L. Milot, Michael B. Johnston, Henry J. Snaith, and Laura M. Herz. Photovoltaic mixed-cation lead mixed-halide perovskites: links between crystallinity, photo-stability and electronic properties. *Energy Environ. Sci.*, 10:361–369, 2017.

[112] Guy M. Bernard, Atul Goyal, Mark Miskolzie, Ryan McKay, Qichao Wu, Roderick E. Wasylishen, and Vladimir K. Michaelis. Methylammonium lead chloride: A sensitive sample for an accurate NMR thermometer. *Journal of Magnetic Resonance*, 283:14 – 21, 2017.

[113] Senocrate Alessandro, Moudrakovski Igor, Kim Gee Yeong, Yang Tae-Youl, Gregori Giuliano, Grätzel Michael, and Maier Joachim. The Nature of Ion Conduction in Methylammonium Lead Iodide: A Multimethod Approach. *Angewandte Chemie International Edition*, 56(27):7755–7759, 2017.

[114] Giacomo Maculan, Arif D. Sheikh, Ahmed L. Abdelhady, Makhsud I. Saidaminov, Md Azimul Haque, Banavoth Murali, Erkki Alarousu, Omar F. Mohammed, Tom Wu, and Osman M. Bakr. $CH_3NH_3PbCl_3$ Single Crystals: Inverse Temperature Crystallization and Visible-Blind UV-Photodetector. *The Journal of Physical Chemistry Letters*, 6(19):3781–3786, 2015.

[115] Cecil Dybowski and Guenther Neue. Solid state ^{207}Pb NMR spectroscopy. *Progress in Nuclear Magnetic Resonance Spectroscopy*, 41(3):153 – 170, 2002.

[116] L. Vegard. Die konstitution der mischkristalle und die raumfüllung der atome. *Zeitschrift für Physik*, 5(1):17–26, 1921.

[117] Liang Po-Wei, Liao Chien-Yi, Chueh Chu-Chen, Zuo Fan, Williams Spencer T., Xin Xu-Kai, Lin Jiangjen, and Jen Alex K.-Y. Additive Enhanced Crystallization of Solution-Processed Perovskite for Highly Efficient Planar-Heterojunction Solar Cells. *Advanced Materials*, 26(22):3748–3754, 2014.

[118] Yaron Tidhar, Eran Edri, Haim Weissman, Dorin Zohar, Gary Hodes, David Cahen, Boris Rybtchinski, and Saar Kirmayer. Crystallization of methylammonium

lead halide perovskites: Implications for photovoltaic applications. *Journal of the American Chemical Society*, 136(38):13249–13256, 2014.

[119] Tauc J., Grigorovici R., and Vancu A. Optical properties and electronic structure of amorphous germanium. *Physica Status Solidi (b)*, 15(2):627–637, 1966.

[120] Guy M Bernard, Roderick E Wasylishen, Christopher I Ratcliffe, Victor Terskikh, Qichao Wu, Jillian M Buriak, and Tate Hauger. Methylammonium Cation Dynamics in Methylammonium Lead Halide Perovskites: A Solid-State NMR Perspective. *The Journal of Physical Chemistry A*, 122(6):1560–1573, 2018.

[121] Eric G. Keeler, Vladimir K. Michaelis, Michael T. Colvin, Ivan Hung, Peter L. Gor'kov, Timothy A. Cross, Zhehong Gan, and Robert G. Griffin. ^{17}O MAS NMR Correlation Spectroscopy at High Magnetic Fields. *Journal of the American Chemical Society*, 139(49):17953–17963, 2017.

[122] Zhiguo Xia, Yuanyuan Zhang, Maxim S. Molokeev, and Victor V. Atuchin. Structural and Luminescence Properties of Yellow-Emitting $NaScSi_2O_6$:Eu^{2+} Phosphors: Eu^{2+} Site Preference Analysis and Generation of Red Emission by Codoping Mn^{2+} for White-Light-Emitting Diode Applications. *The Journal of Physical Chemistry C*, 117(40):20847–20854, 2013.

[123] A. R. Denton and N. W. Ashcroft. Vegard's law. *Phys. Rev. A*, 43:3161–3164, 1991.

[124] Shalabh Gupta, Ihor Z. Hlova, Takeshi Kobayashi, Roman V. Denys, Fu Chen, Ihor Y. Zavaliy, Marek Pruski, and Vitalij K. Pecharsky. Facile synthesis and regeneration of $Mg(BH_4)_2$ by high energy reactive ball milling of MgB_2. *Chem. Commun.*, 49:828–830, 2013.

[125] Tomislav Friščić, Ivan Halasz, Patrick J Beldon, Ana M Belenguer, Frank Adams, Simon A J Kimber, Veijo Honkimäki, and Robert E Dinnebier. Real-time and in situ monitoring of mechanochemical milling reactions. *Nature Chemistry*, 5:66, 2012.

[126] Jean-Louis Do and Tomislav Friščić. Mechanochemistry: A force of synthesis. *ACS Central Science*, 3(1):13–19, 2017.

[127] Gerd Kaupp. Solid-state molecular syntheses: complete reactions without auxiliaries based on the new solid-state mechanism. *CrystEngComm*, 5:117–133, 2003.

[128] Gergely F. Samu, Csaba Janáky, and Prashant V. Kamat. A Victim of Halide Ion Segregation. How Light Soaking Affects Solar Cell Performance of Mixed Halide Lead Perovskites. *ACS Energy Letters*, 2(8):1860–1861, 2017.

[129] Charles F. Forney and David G. Brandl. Control of humidity in small controlled-environment chambers using glycerol-water solutions. *HortTechnology*, 2(1):52–54, 1992.

Appendix A

Experimental Section & Additional Data for Chapter 2

A.1 Chemicals and Reagents

Starting materials were obtained from commercial sources; lead(II) iodide (99%) from Acros Organics (Morris Plains, NJ, USA); methylammonium iodide from Dyesol Limited (Australia); γ-butyrolactone (GBL) (>99%) from Sigma-Aldrich (St. Louis, MO, USA); lead(II) nitrate (>99%) from Fisher Scientific (Pittsburgh, PA, USA); and used as received without any further purification.

A.2 Syntheses

A.2.1 Methylammonium Lead Iodide, $CH_3NH_3PbI_3$ ($MAPbI_3$)

Single crystals of $MAPbI_3$ were prepared by the inverse-temperature solubility method developed by Saidaminov.[25] A 1.0 M solution of methylammonium iodide (MAI) and PbI_2 in GBL was dissolved at 333 K, filtered, and then heated to 389 K where crystallization of $MAPbI_3$ occurs. After 2 h, the crystals, which were 4-5 mm across, were removed from the solution, rinsed quickly with GBL, and dried with nitrogen

gas. The crystals were kept in a desiccator to inhibit hydration.

A.2.2 Methylammonium Lead Iodide Monohydrate, $CH_3NH_3PbI_3 \cdot H_2O$ (Monohydrate)

The perovskite-monohydrate powder was synthesized as reported by Christians et al.[47] A 0.2 M aqueous solution of $Pb(NO_3)_2$ was added dropwise at room temperature to a 1.2 M aqueous solution of MAI. The solution was left for 18 h until a pale yellow precipitate formed. The precipitate was filtered, vacuum dried, and sealed, protecting it from dehydrating to $MAPbI_3$.

A.2.3 Methylammonium Lead Iodide Dihydrate, $(CH_3NH_3)_4PbI_6 \cdot 2H_2O$ (Dihydrate)

Methylammonium lead iodide dihydrate was synthesized in films using a spin-coating method developed by Halder et al.[1] A 1:4 (M/M) solution of PbI_2:MAI was dissolved in DMF and spin-coated at 2000 rpm. The films were then heated at 263 K for 5 min and then cooled in a humid atmosphere (RH = 85%). After 20 min, the dihydrate films were a slightly transparent gray color.

A.3 Powder X-ray Diffraction

Powder X-ray diffraction (pXRD) was used to verify that the desired products had been synthesized. Powder patterns were obtained on a Bruker AXS D8 diffractometer using a Cu Kα radiation source. A 2D detector was used for scanning of the 2θ angles. For $MAPbI_3$, the monohydrate, and PbI_2, a fine powder was prepared and XRD was carried out with Omega = 5°. Due to its sensitivity to air and humidity, the monohydrate was sealed in a 1 mm diameter capillary prior to acquisition of XRD data. The XRD measurements for the dihydrate were carried out on thin films spin-coated on a glass substrate. All humidity- and heat- treated samples were handled as

described for the monohydrate.

A.4 Relative Humidity Control

The humidity experiments were conducted in a humidity-controlled, home-built flow cell (see Figure A.1); the RH was measured continuously through a sensor placed inside the cell, which was placed in the dark. Reported RH values are accurate to within ±5%. In humidity-only experiments, the temperature inside the cell was maintained at room temperature (293 ± 1 K). The humidity control technique is that reported previously;[129] to ensure that no liquid water entered the flow cell, an additional empty flask was added between the humidity source and the cell to serve as a water trap (Figure A.1). In mixed humidity-heat experiments, a hot plate was placed inside the cell at a fixed temperature. In all experiments, the perovskite was ground using an agate mortar and pestle to a fine powder (50 µm grains) and spread into an even thin layer on a borosilicate glass (Pyrex) Petri dish within the cell. The cell was only opened to collect the samples after specific time points; the humidity within the cell returned quickly to the desired value (≤20 min after opening it).

A.5 Supporting Information - Figures

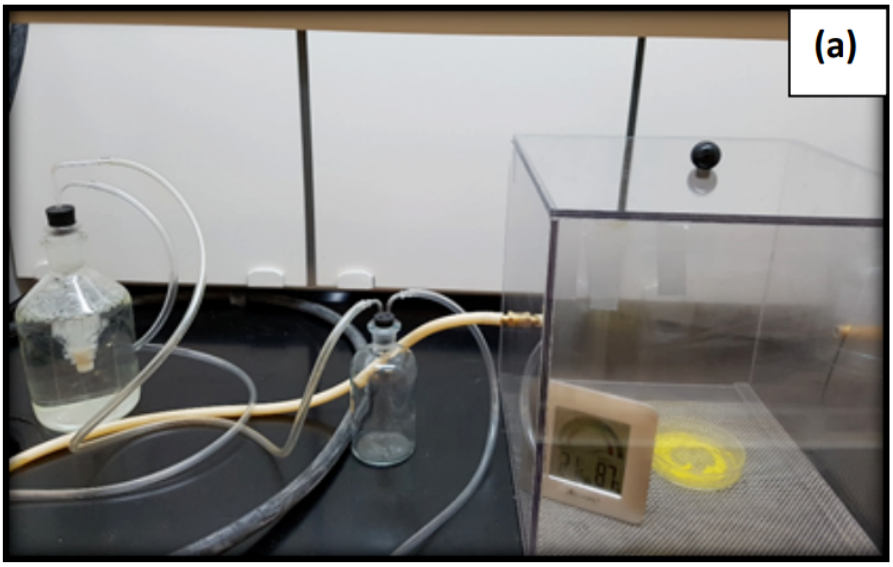

Figure A.1: Flow cell apparatus used to control the relative humidity for the various treatments with $MAPbI_3$.

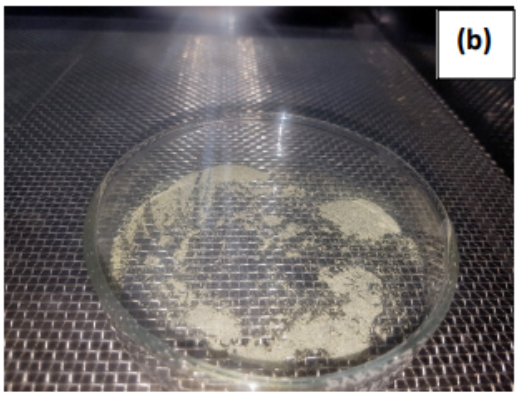

Figure A.2: Image of $MAPbI_3$ powder sample after seven days in the humidity cell (RH = 80%, T = 294 K)

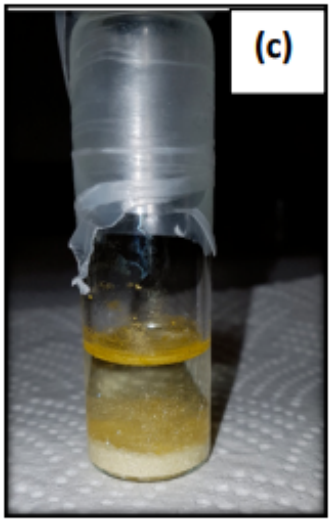

Figure A.3: Image of as-prepared monohydrate sample prior to vacuum drying step

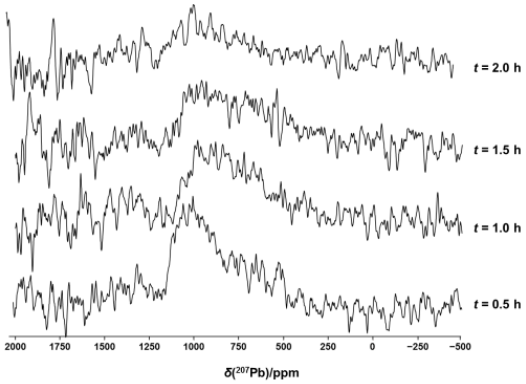

Figure A.4: ^{207}Pb NMR spectra of $MAPbI_3 \cdot H_2O$, acquired at 11.75 T at 324 K. The times on the right indicate the time after the temperature was initially achieved.

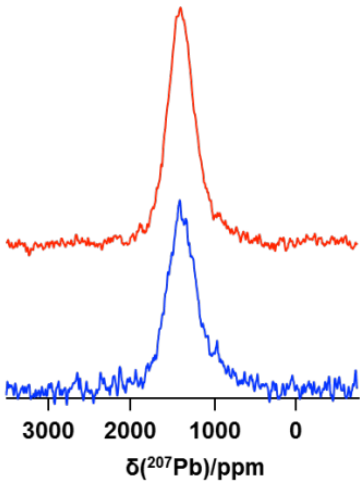

Figure A.5: ^{207}Pb NMR spectra for $MAPbI_3$ (upper traces, red) and of the sample after it was subjected to 7 days at 80% RH, then heated to 341 K (lower traces, blue).

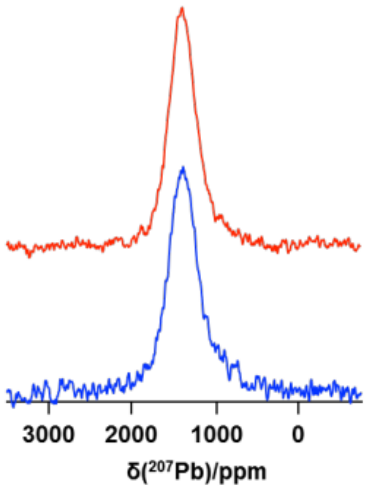

Figure A.6: ^{207}Pb NMR spectra for $MAPbI_3$ (upper traces, red) and of the sample after it was subjected to 11 days at 40 % RH (lower traces, blue). Spectra were acquired at 7.05 T at 294 K

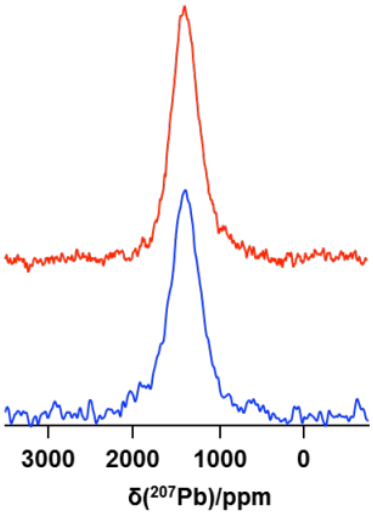

Figure A.7: Comparison of ^{207}Pb NMR spectra for $MAPbI_3$ (upper traces, red) and of the sample after it was left in a furnace for 4 days at 378 K (lower traces, blue).

Appendix B

Experimental Section & Additional Data for Chapter 3

B.1 Synthesis of MHPs

B.1.1 Synthesis of MAPb($X_xX'_{1-x}$)$_3$ MHPs

To synthesize MHPs using the MCS-HG approach, $MAPbX_3$ and $MAPbX'_3$ were loaded with molar ratios set to achieve the desired mixed-halide composition. For example, to prepare $MAPb(Cl_{0.5}Br_{0.5})_3$, 159.66 mg of $MAPbBr_3$ was loaded in a mortar with 115.21 mg of $MAPbCl_3$, and hand grinding was applied for 1-2 h. For MCS-BM techniques, the same ratios of precursors as for the MCS-HG approach were loaded into either a planetary (RETSCH Planetary Ball Mill PM 100) or shaker ball mill (SPEX SamplePrep 8000M Mixer/Mill). We note that, by adjusting the time, ball size, and speed of impacts, one can utilize a planetary mill to obtain similar results to HG within a fraction of the time (i.e., 5-60 min) with good reproducibility. All synthetic procedures were carried out under ambient lab conditions in air. All results presented here for the MCS-BM method were obtained from parent compounds processed by the shaker ball mill for 1 h.

B.1.2 Synthesis of MHPs - $FAPb(X_x\ X'_{1-x})_3$ Using MCS Route.

To synthesize MHPs using MCS-HG, appropriate amounts of $FAPbX_3$ and $FAPbX'_3$ were loaded with molar ratios calculated to achieve the desired mixed halide composition. For example, to prepare $FAPb(Br_{0.75}Cl_{0.25})_3$, 245.99 mg of $FAPbBr_3$ was mixed with 59.77 mg of $FAPbCl_3$. The mixing process by hand grinding continued until a fine powder with uniform colour was achieved. The product was examined by XRD to make sure a single pure phase of MHP was obtained. Similarly, for the MCS-BM route, a RETSCH PM100 planetary ball-milling instrument was used with 250 ml ZrO_2 container and different sized ZrO_2 beads. The rotation speed was 400 rpm, with 1 minute/2 sec on/off ratio and the rotation reversed after each cycle. All the synthesis experiments were undertaken under ambient lab conditions. We note that during the MCS-BM process, the temperature within the container was approximately 50 °C after the BM synthesis procedure due to friction.

B.1.3 Synthesis of MHPs - $FAPb(X_xX'_{1-x})_3$ Using Solvent Synthesis Route

To synthesis $FAPb(Cl_xBr_{1-x})_3$ MHPs using solvent synthesis route, the drop-casting method was used. To prepare $FAPb(Br_{0.75}Cl_{0.25})_3$, stoichiometric amounts of FABr (62.49 mg), FACl (120.78 mg), and $PbBr_2$ (734.02 mg) were dissolved at room temperature in 2 ml of DMF to yield a 1 M solution, then drop casted on a pre-heated clean glass substrates at 60 °C and left for drying in an ambient air for 0.5 to 1 h. The formed film was collected and examined by XRD and a single crystallographic pure phase was obtained. For the solvent synthesis of $FAPb(Br_{0.5}I_{0.5})_3$, a precipitation technique was followed, which is a similar procedure to that used elsewhere[53] to prepare $MAPb(Br_{0.5}I_{0.5})_3$. Briefly, a mixture of PbI_2 (0.072 mmol), FAI (0.216 mmol), $PbBr_2$ (0.072 mmol), and FABr (0.216 mmol) were dissolved in a mixture of acetonitrile (20 mL) and DMF (200 µL), followed by precipitation via the addition of excess toluene. The product was then collected and dried under vacuum.

B.2 Measurements

B.2.1 Diffuse Reflectance (DR) Spectroscopy of MHP Perovskites.

A Varian Cary 400 UV-visible spectrophotometer, equipped for the analysis of small-quantity fine powdered samples, was used to obtain DR data. Each sample was packed into a black boat (loaded with ∼100 mg/sample), with each measurement acquired between wavelengths of 300 and 900 nm.

B.2.2 Powder X-ray Diffraction (XRD) Measurements.

Fine powder samples were mounted on a glass slide and analysed using a Bruker D8 Advance Diffractometer equipped with a Cu Kα source and a VANTEC-500 2D detector. All data were acquired at room temperature with a 2θ range of 10°-60° and 0.005° resolution.

B.3 Supporting Information - Figures (MCS of MA-MHPs)

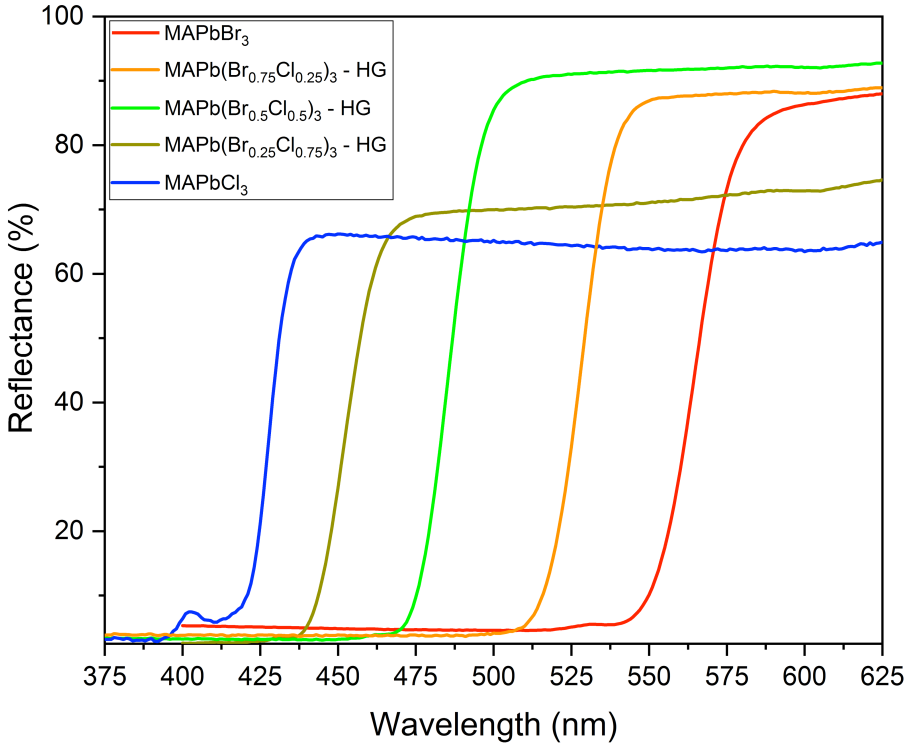

Figure B.1: Diffuse reflectance spectra for MCS-HG MAPb(Cl_xBr_{1-x})$_3$, with x = 0.75, 0.50, and 0.25, along with those for their parent compounds, $MAPbBr_3$ and $MAPbCl_3$.

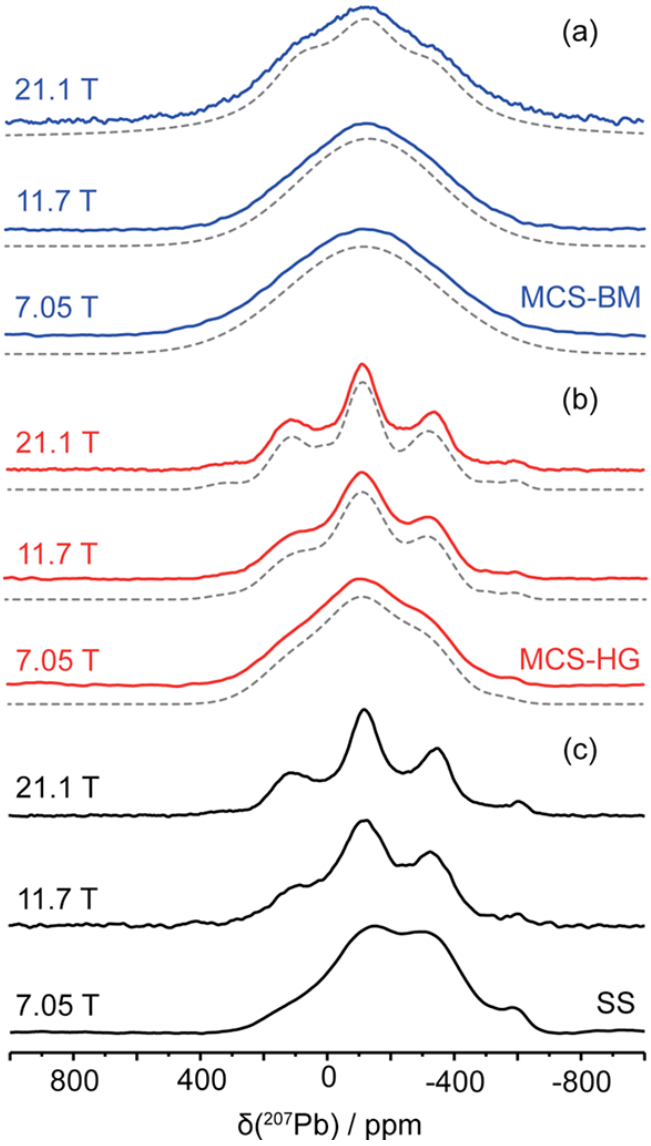

Figure B.2: ^{207}Pb NMR spectra of non-spinning MCS-BM (a, blue), MCS-HG (b, red), and SS (c, black) samples of $MAPb(Cl_{0.5}Br_{0.5})_3$, acquired at 7.05 T, 11.7 T, and 21.1 T. The gray dotted lines are the best fits for the spectra obtained for the samples prepared with the mechanochemical synthesis methods.

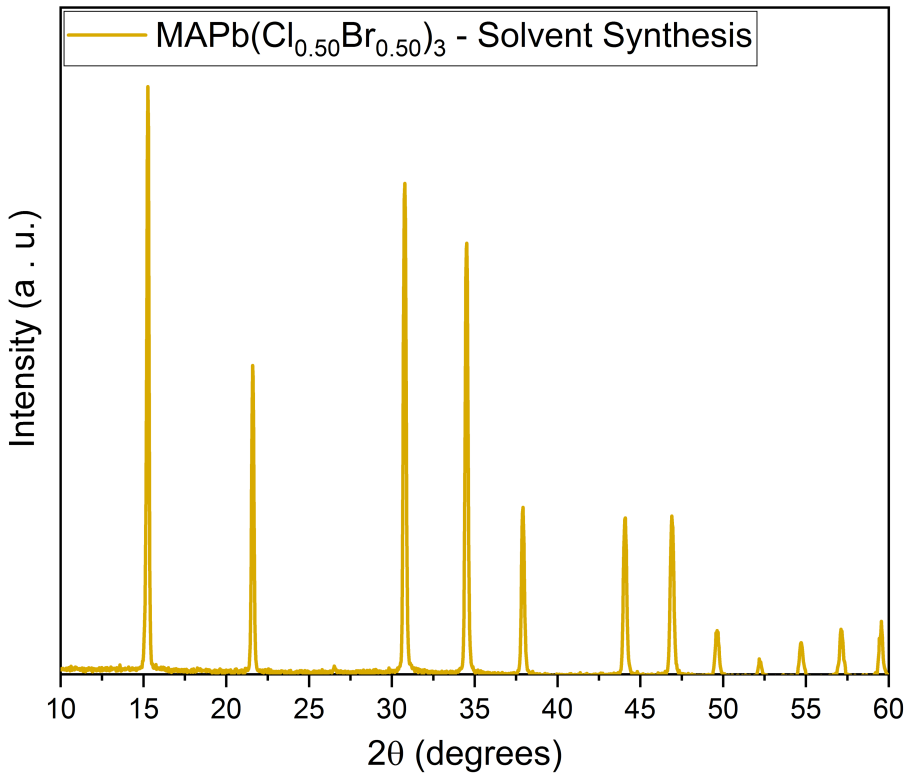

Figure B.3: Powder XRD pattern for $MAPb(Cl_{0.5}Br_{0.5})_3$ prepared using the SS method.

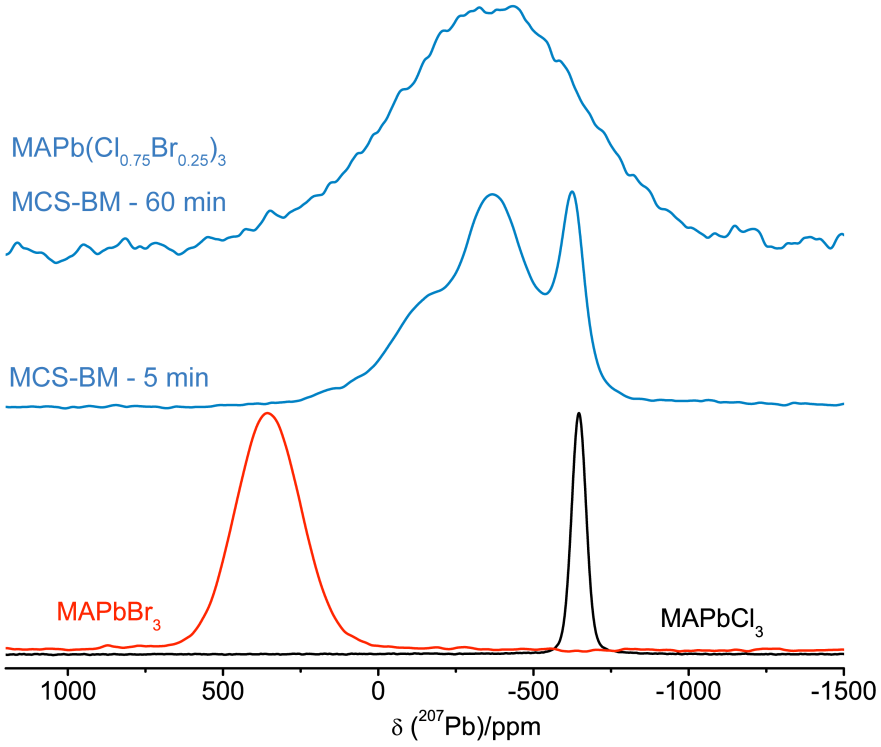

Figure B.4: ^{207}Pb NMR spectra of non-spinning $MAPb(Cl_{0.75}Br_{0.25})_3$, prepared by using the MCS-BM method for 5 min and 1 hr.

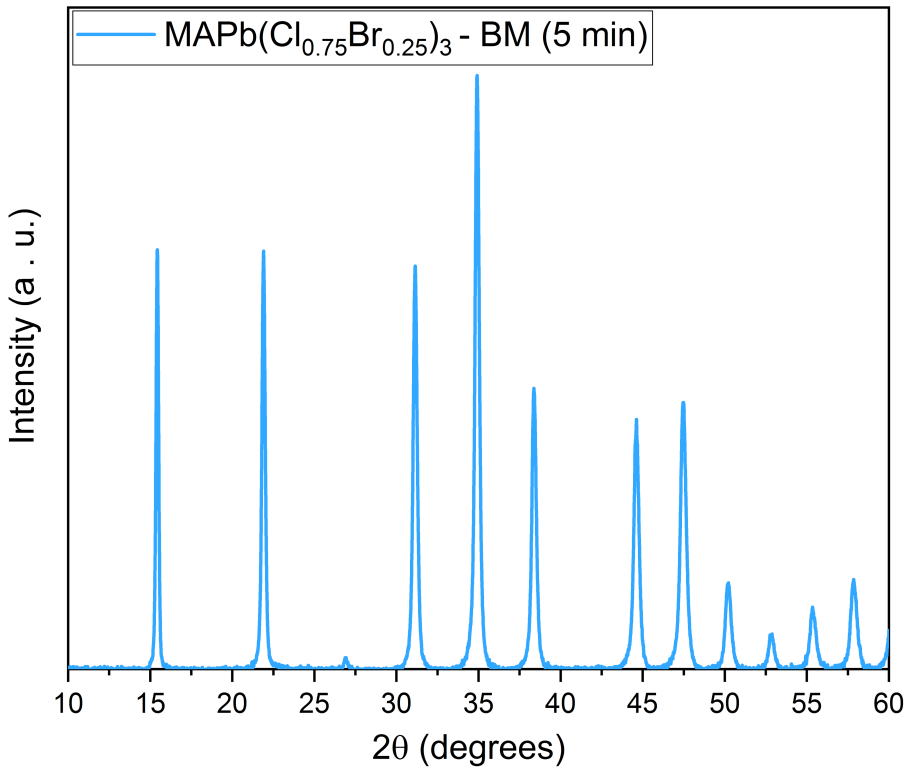

Figure B.5: XRD pattern obtained after using the MCS-BM method for 5 min for $MAPb(Cl_{0.75}Br_{0.25})_3$.

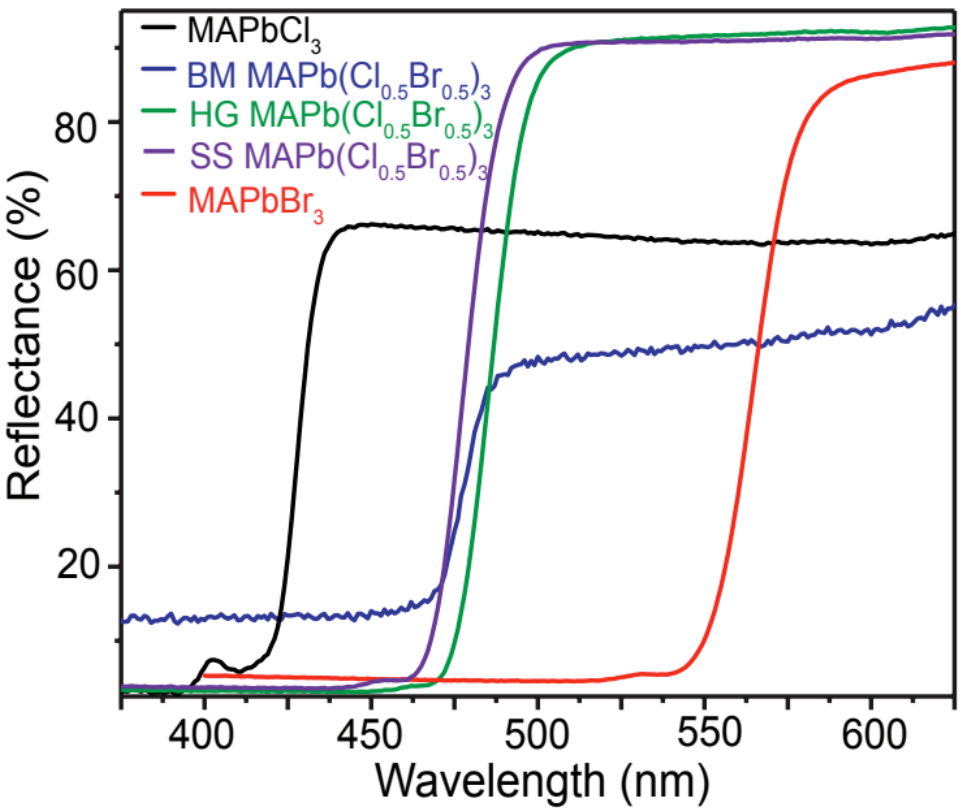

Figure B.6: Diffuse reflectance spectra for $MAPb(Cl_{0.5}Br_{0.5})_3$, prepared by BM, HG, and SS, along with those for the parent compounds, $MAPbBr_3$ and $MAPbCl_3$

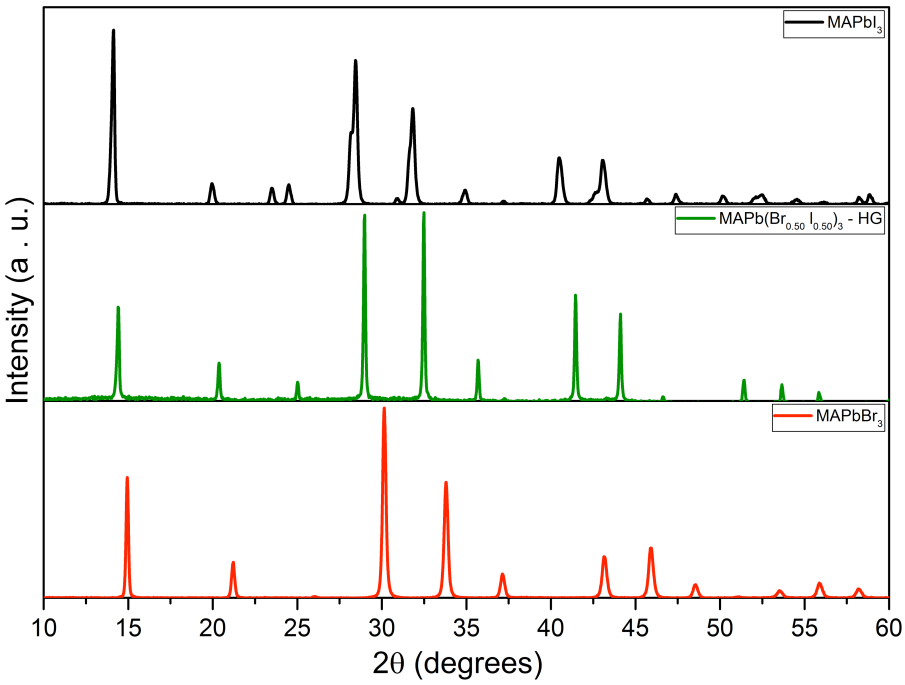

Figure B.7: Comparison between XRD patterns of $MAPb(Br_{0.5}I_{0.5})_3$ prepared by MCS-HG (2 hr) and those for the parent compounds, $MAPbI_3$ (tetragonal) and $MAPbBr_3$ (cubic).

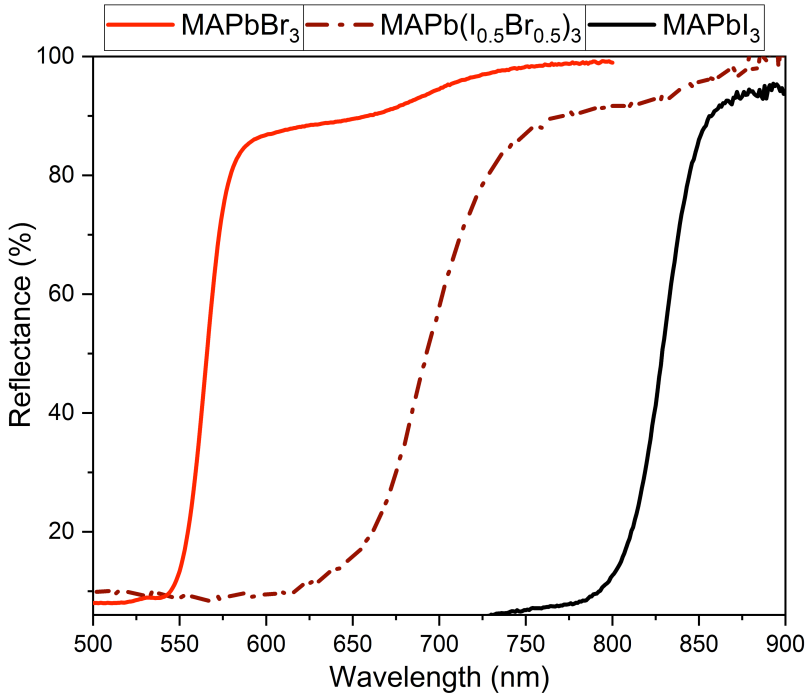

Figure B.8: Diffuse reflectance spectra of the $MAPb(Br_{0.5}I_{0.5})_3$ sample prepared by MCS-HG, along with those for the parent compounds, $MAPbBr_3$ and $MAPbI_3$.

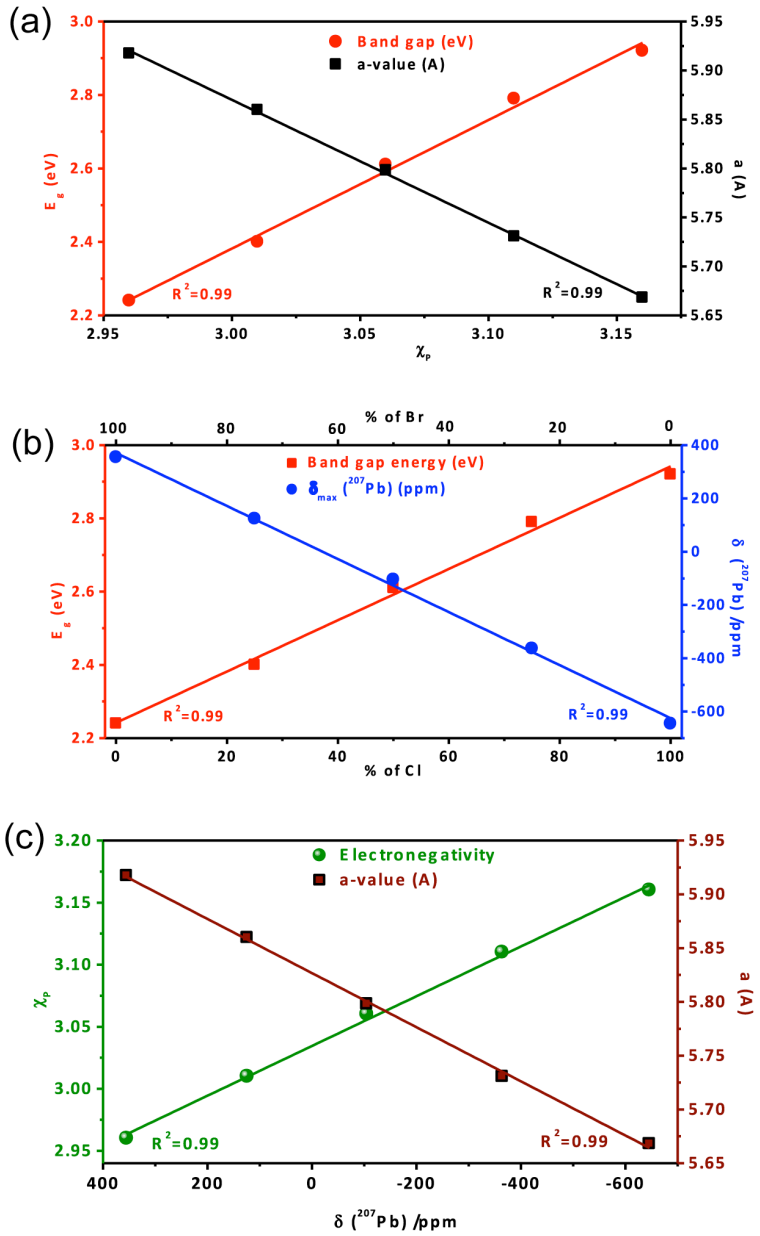

Figure B.9: Relationship between MHP physical properties (Band gap (E_g)) and electronegativity (χ) with atomic structure from X-ray diffraction (unit cell parameter, a (Å)) and NMR spectroscopy (chemical shift, $\delta(^{207}\text{Pb})$/ppm).

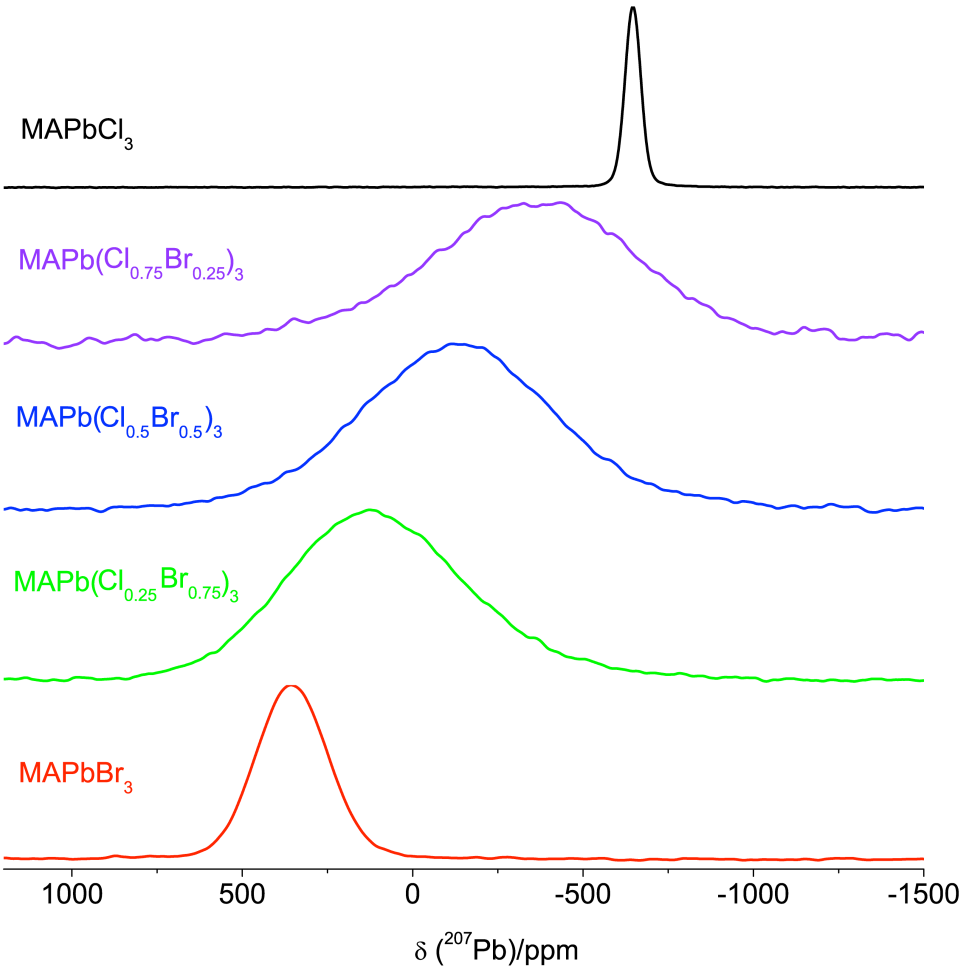

Figure B.10: ^{207}Pb NMR spectra for nonspinning MAPb(Cl_xBr_{1-x})$_3$, where x = 0, 0.25, 0.50, 0.75 and 1. MCS-BM method was used to prepare MHPs (purple, blue and green). Samples were ball milled for a period of 1 hr. All spectra were acquired at 7.05 T.

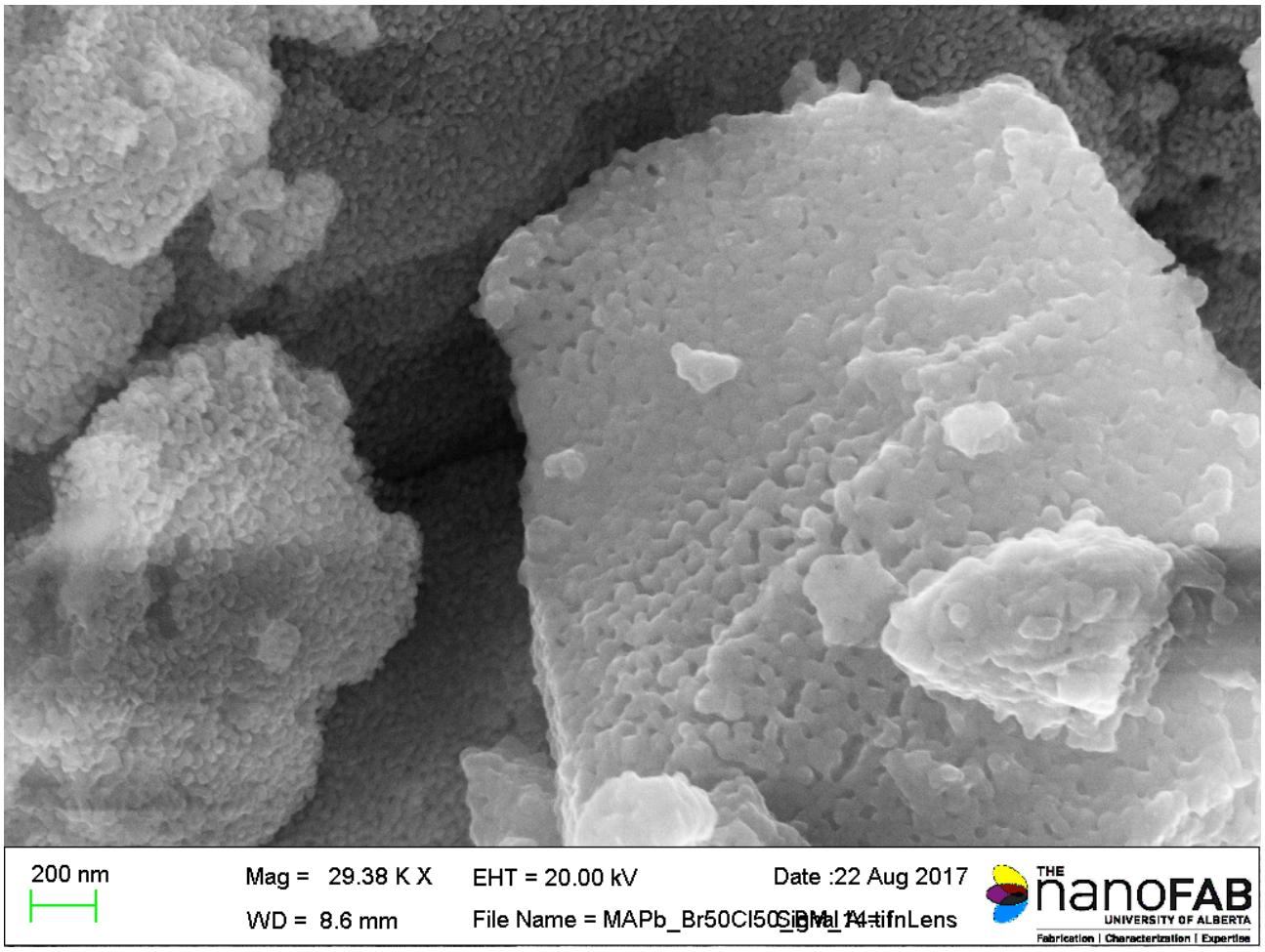

Figure B.11: FESEM image for MCS-BM MHP sample MAPb($Cl_{0.5}Br_{0.5}$) with high (200 nm) magnification.

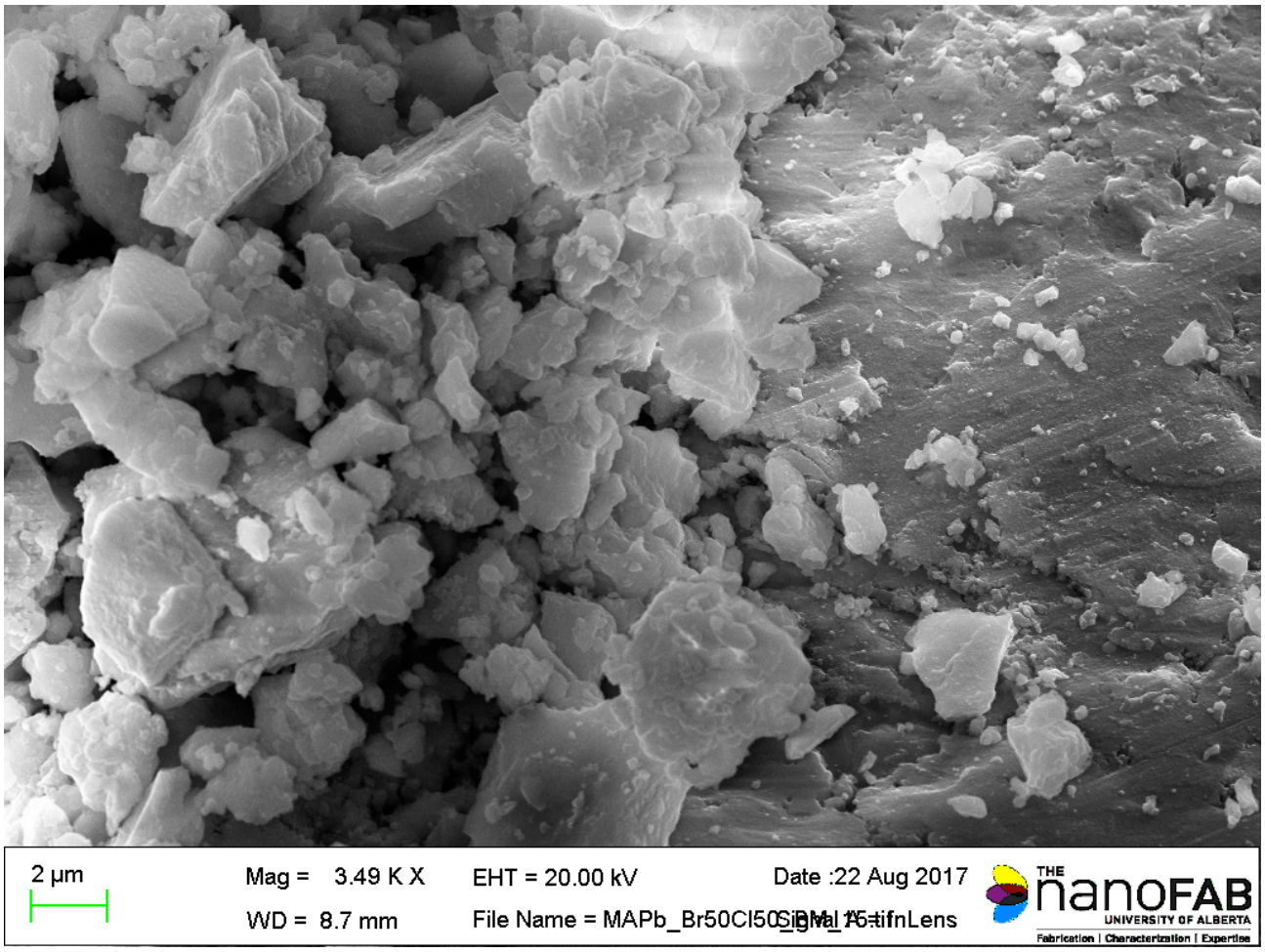

Figure B.12: FESEM image for MCS-BM MHP sample $MAPb(Cl_{0.5}Br_{0.5})$ with low (2 µm) magnification.

B.4 Supporting Information - Figures (MCS of FA-MHPs)

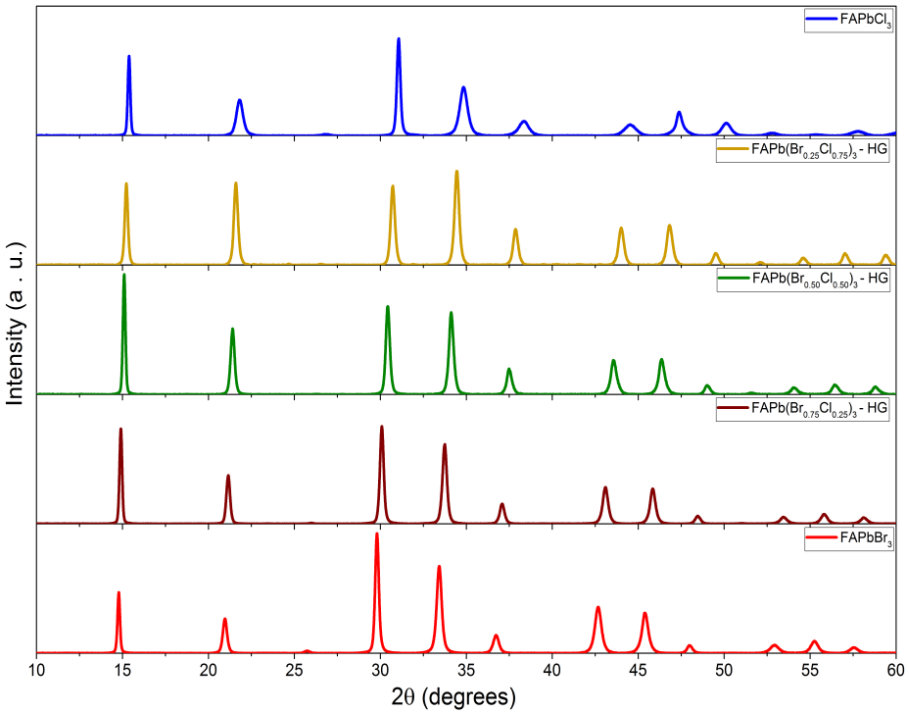

Figure B.13: Powder XRD patterns for the MCS-HG FAPb$(Cl_xBr_{1-x})_3$ series of samples.

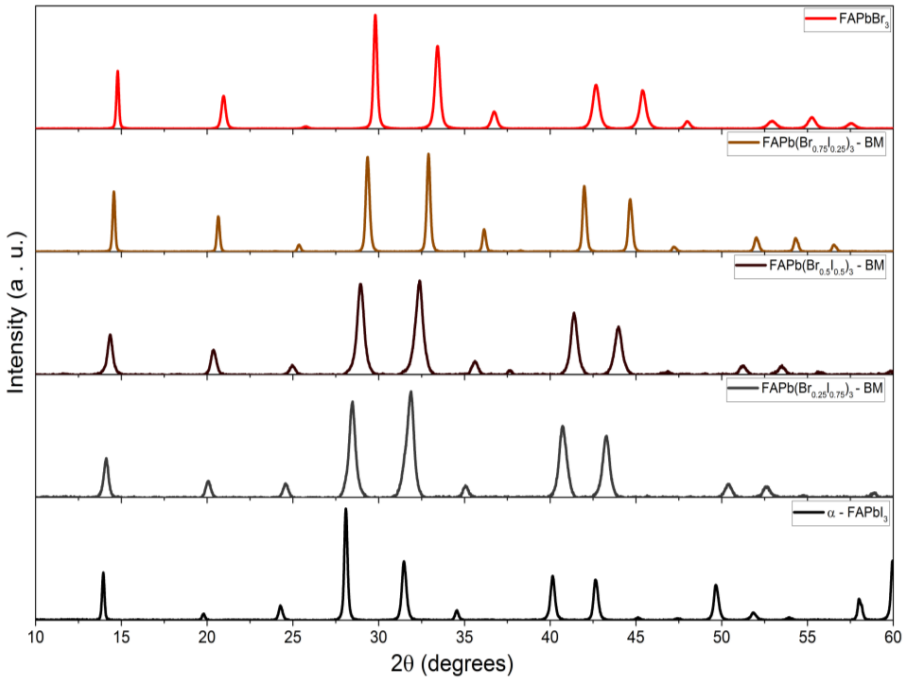

Figure B.14: Powder XRD patterns for the MCS-BM FAPb$(Br_xI_{1-x})_3$ series of samples.

Table B.1: Elemental atomic ratios for the MHP samples determined using the EDX technique.

Sample	***Cl (atomic %)***	***Br (atomic %)***	***Ratio***	***Cl+Br (X) (atomic %)***	***Pb (atomic %)***	***X:Pb***
$MAPb(Cl_{0.25}Br_{0.75})_3$ - HG	5.8	19.2	1:3.3	25	8.8	2.8:1
$MAPb(Cl_{0.50}Br_{0.50})_3$ - HG	10.8	10.4	1.03:1	21.2	7.7	2.8:1
$MAPb(Cl_{0.75}Br_{0.25})_3$ - HG	5.9	1.9	3.01:1	7.8	2.7	2.8:1
$MAPb(Cl_{0.50}Br_{0.50})_3$ - BM	7.3	8.0	1:1.09	15.3	5.5	2.8:1
$MAPb(Cl_{0.50}Br_{0.50})_3$ - SS	6.94	5.0	1.38:1	11.9	5.12	2.3:1

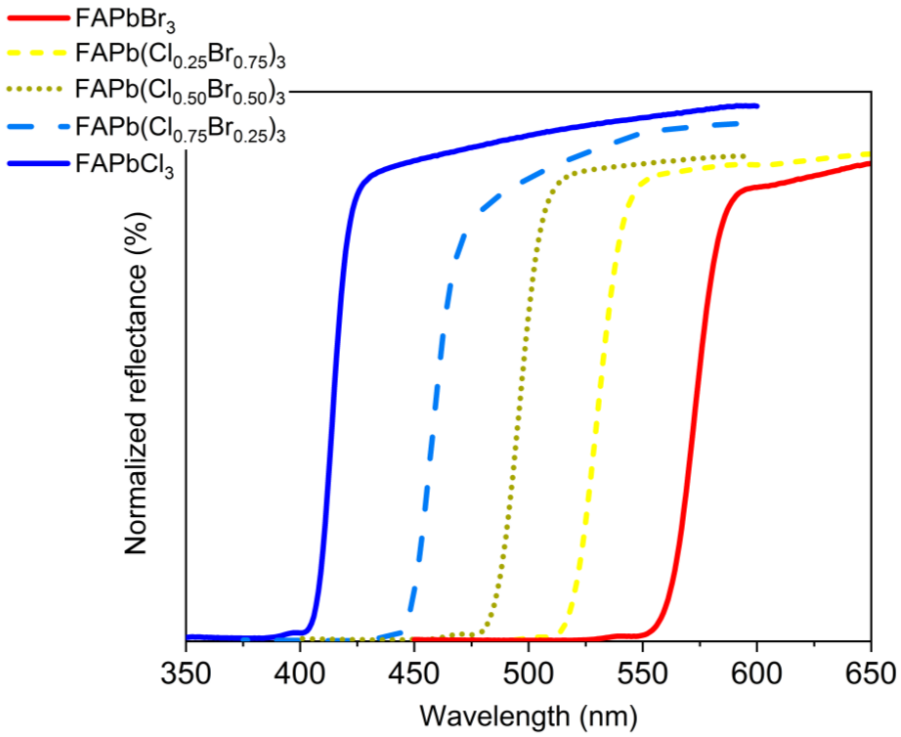

Figure B.15: Reflectance spectra for $FAPb(Cl_xBr_{1-x})_3$ prepared by HG, where x:0.75, 0.50, and 0.25, along with those for the parent compounds, $FAPbCl_3$ and $FAPbBr_3$.

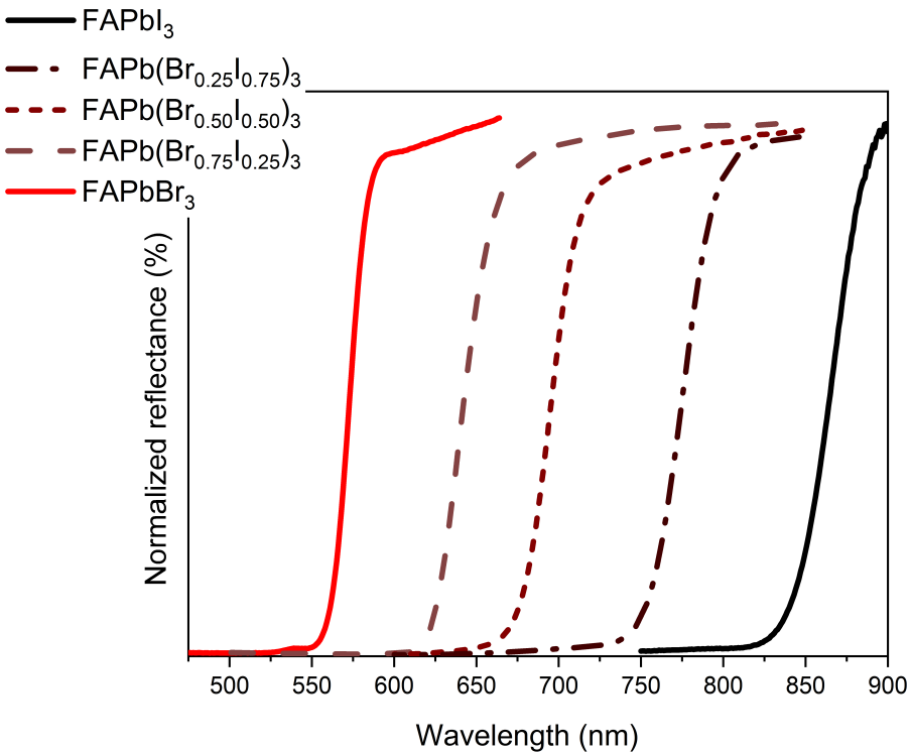

Figure B.16: Reflectance spectra for $FAPb(Br_xI_{1-x})_3$ prepared by BM, where x:0.75, 0.50, and 0.25, along with those for the parent compounds, $FAPbBr_3$ and α-$FAPbI_3$.

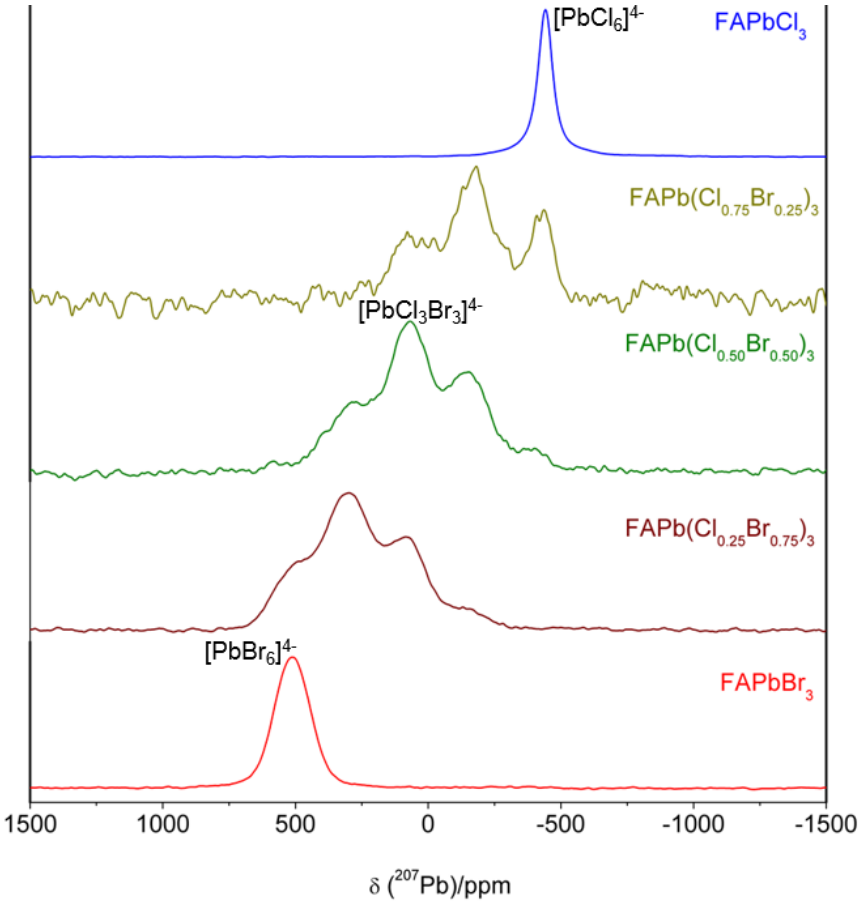

Figure B.17: ^{207}Pb NMR spectra for nonspinning FAPb(Cl_xBr_{1-x})$_3$ prepared by HG, where x = 0.75, 0.50, and 0.25, along with those for the parent compounds, $FAPbCl_3$ and $FAPbBr_3$, acquired at 11.75 T.

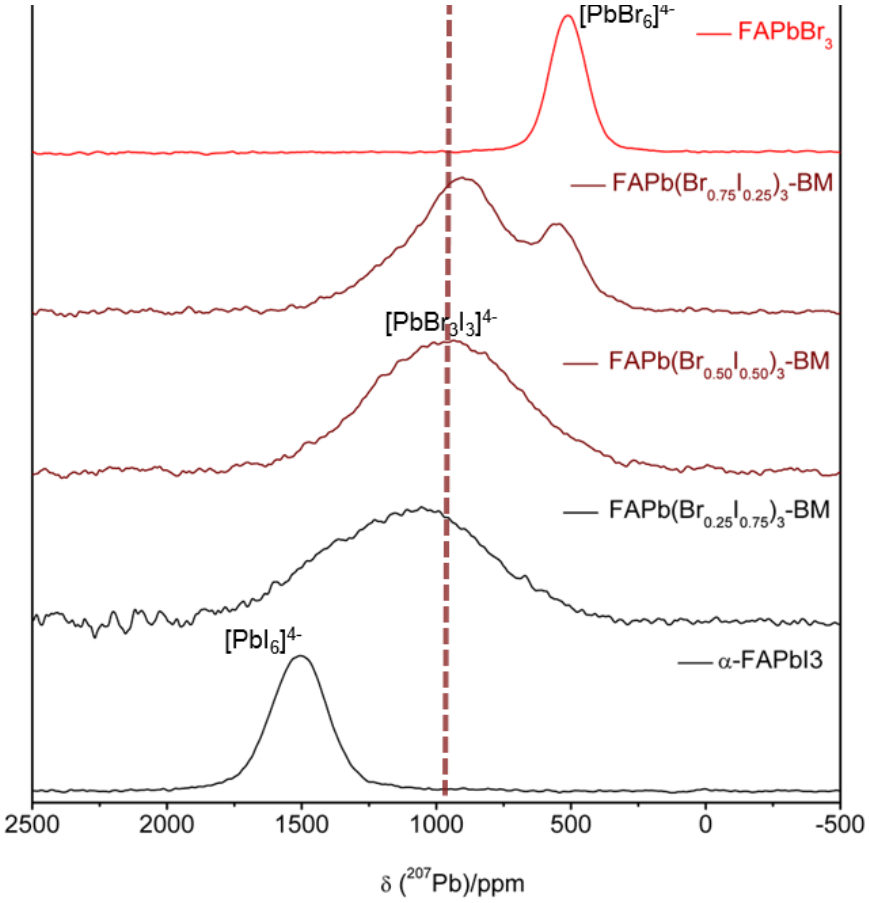

Figure B.18: ^{207}Pb NMR spectra for nonspinning FAPb(Br_xI_{1-x})$_3$ prepared by BM, where x = 0.75, 0.50, and 0.25, along with those for the parent compounds, FAPbBr$_3$ and α-FAPbI$_3$ acquired at 11.75 T.

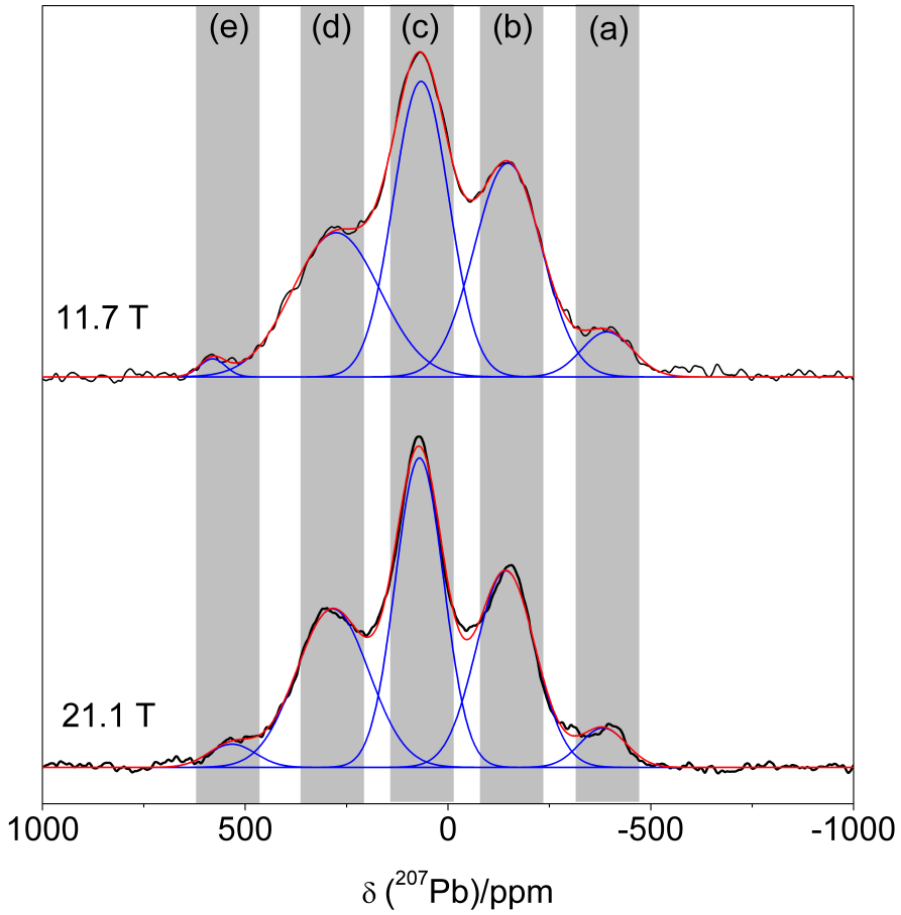

Figure B.19: ^{207}Pb NMR spectra for nonspinning HG-FAPb($Cl_{0.5}Br_{0.5}$)$_3$ acquired at 11.75 and 21.1 T, with peak fitting assuming a simple Gaussian lineshape. $[PbCl_6]^{4-}$ (a); $[PbCl_5Br]^{4-}$/$[PbCl_4Br_2]^{4-}$ (b); $[PbCl_3Br_3]^{4-}$ (c); $[PbCl_2Br_4]^{4-}$/$[PbClBr_5]^{4-}$ (d); $[PbBr_6]^{4-}$ (e).

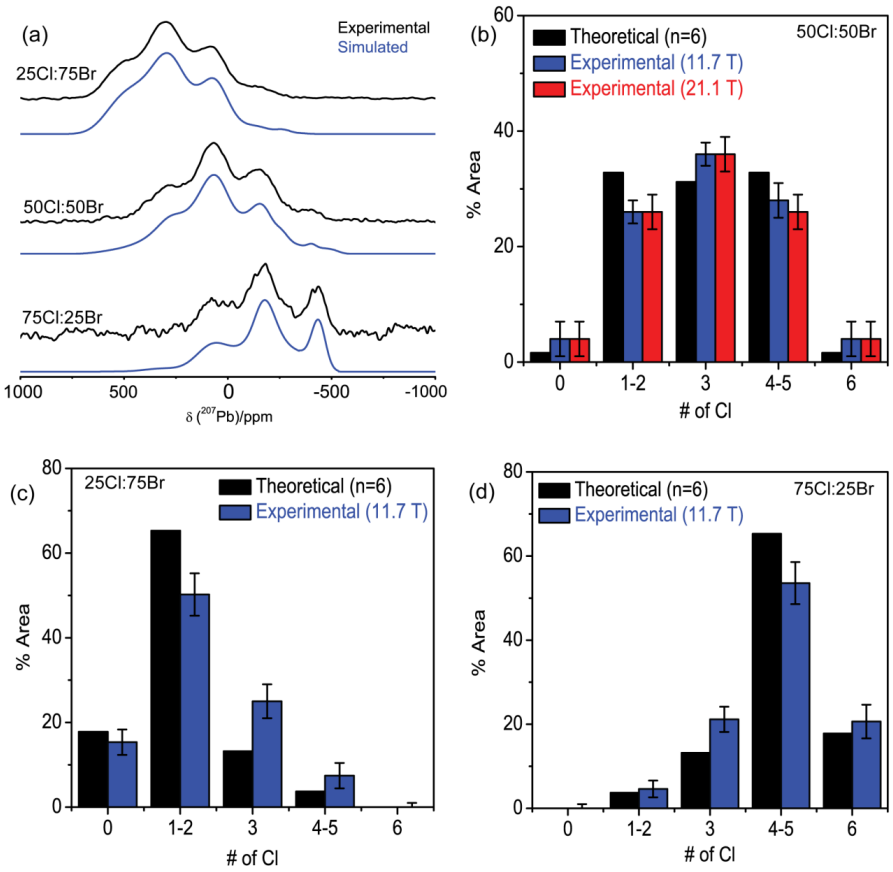

Figure B.20: ^{207}Pb NMR spectra and the binomial distribution for nonspinning HG-FAPb(Cl_xBr_{1-x})$_3$ based on the curve fitting of the ^{207}Pb NMR acquired at 11.75 and 21.1 T. Error bars shown here are based on a comparison of the simulated and experimental spectra. (a) ^{207}Pb NMR spectra at 11.75 T for HG-FAPb(Cl_xBr_{1-x})$_3$ with fitted curves using insight from the DFT data (not included here).[2] (b) Comparison between theoretical binomial distributions based on 7 different sites (n = 6) and the population distribution for HG-FAPb($Cl_{0.5}Br_{0.5}$)$_3$ extracted from area under curve for 207Pb NMR spectra acquired at 11.75 and 21.1 T. (c and d) As for (b), but for HG-FAPb($Cl_{0.25}Br_{0.75}$)$_3$ and HG-FAPb($Cl_{0.75}Br_{0.25}$)$_3$, respectively with data obtained at 11.75 T.

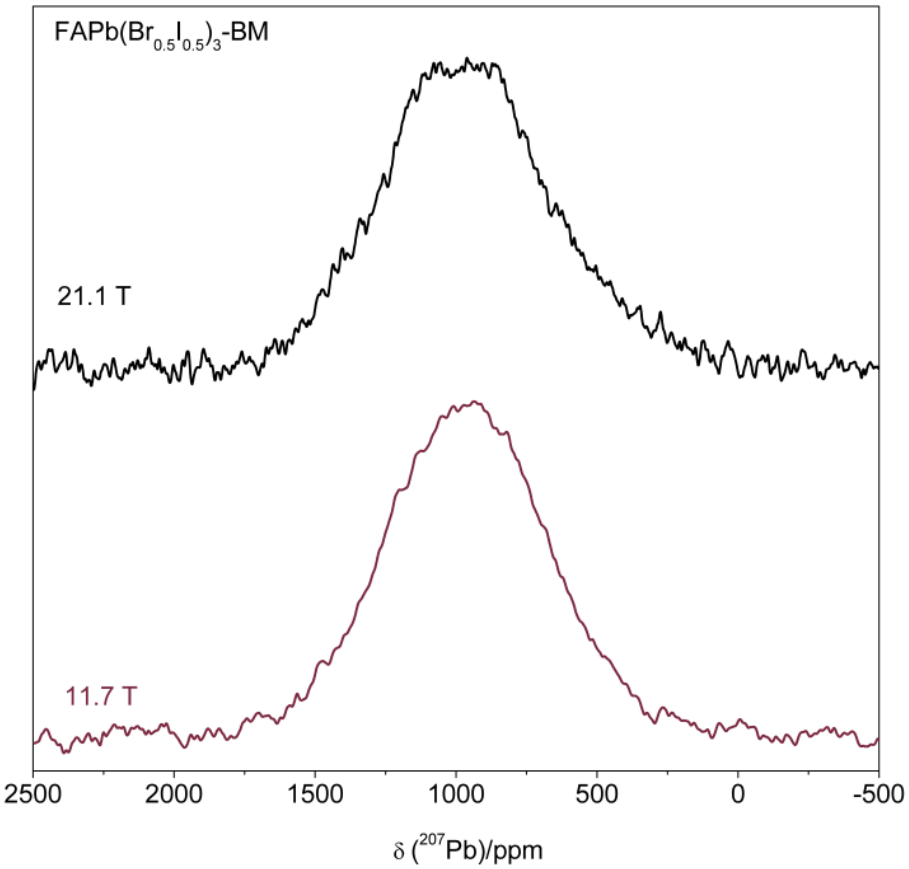

Figure B.21: Comparison between ^{207}Pb NMR spectra for nonspinning MCS-BM of $FAPb(Br_{0.5}I_{0.5})_3$ acquired at 11.75 and 21.1 T.

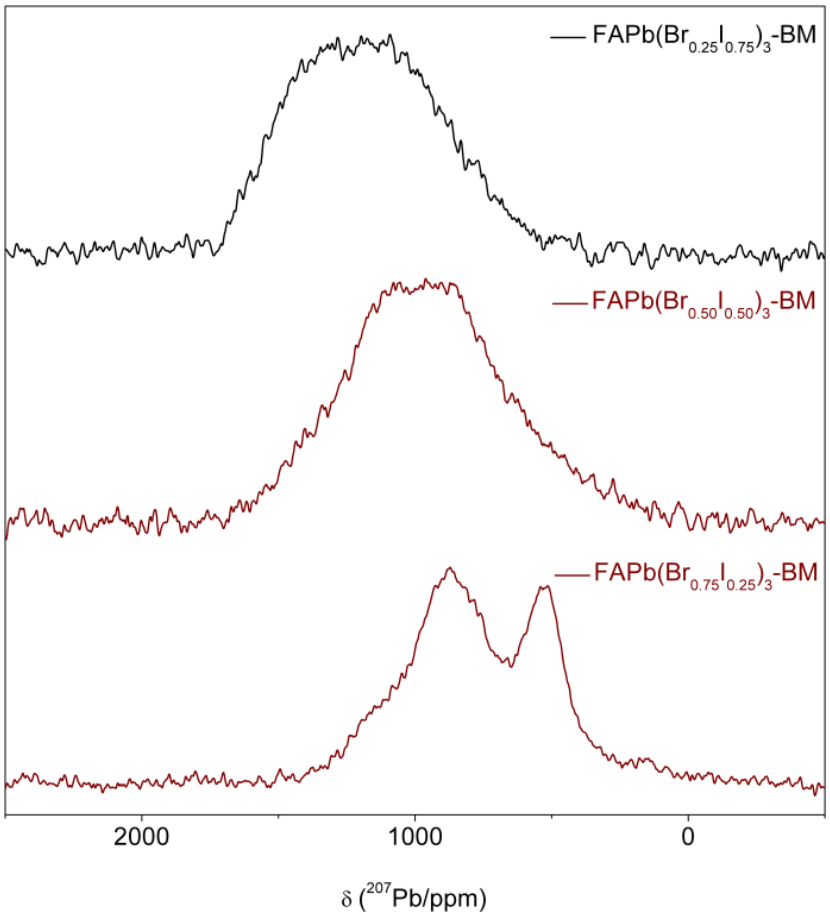

Figure B.22: ^{207}Pb NMR spectra for the non-spinning MCS-BM FAPb(Br_xI_{1-x})$_3$ series of samples acquired at 21.1 T.

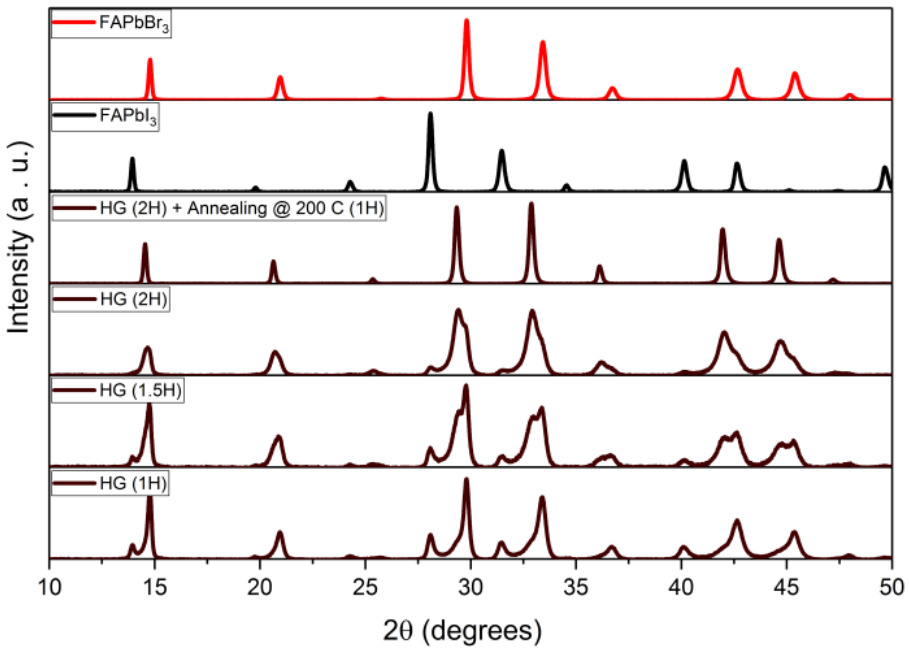

Figure B.23: Powder XRD comparison of FAPb($Br_{0.75}I_{0.25}$)$_3$ prepared by HG at different time stamps and after an additional 1 hr of annealing at 200 °C, along with those for the parent compounds, $FAPbBr_3$ and α-$FAPbI_3$.

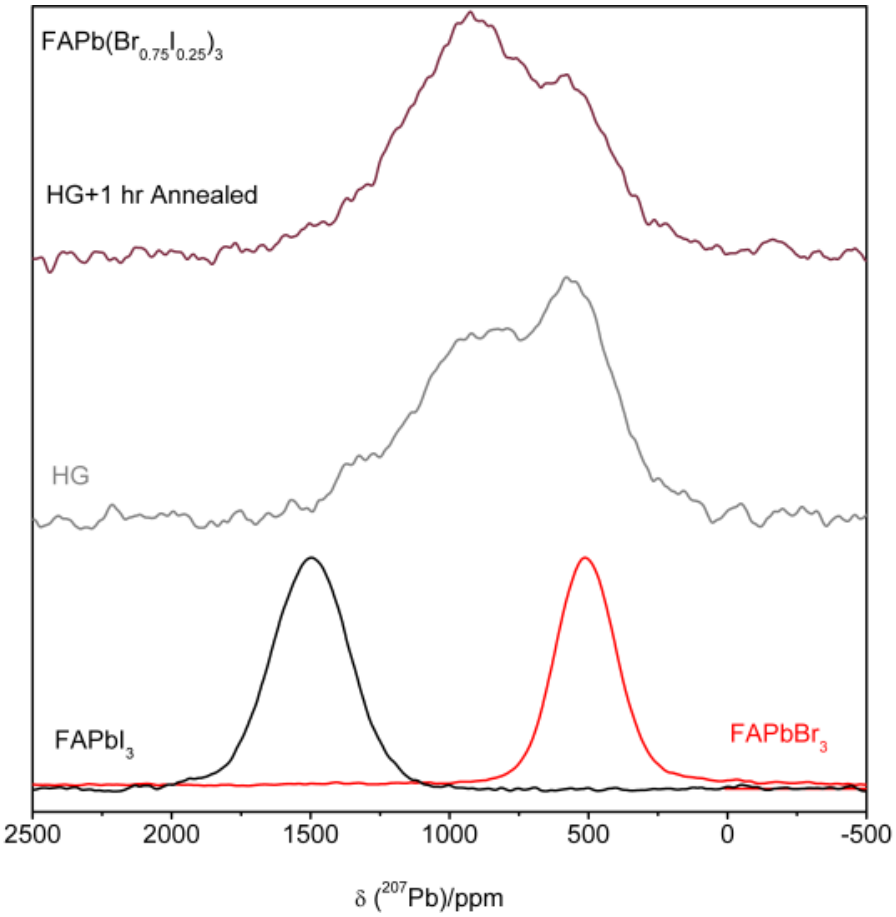

Figure B.24: Comparison between the ^{207}Pb NMR spectra of non-spinning FAPb($Br_{0.75}I_{0.25}$)$_3$ prepared by HG before and after 1 h of annealing, along with those for the parent compounds, FAPbBr$_3$ and α-FAPbI$_3$.

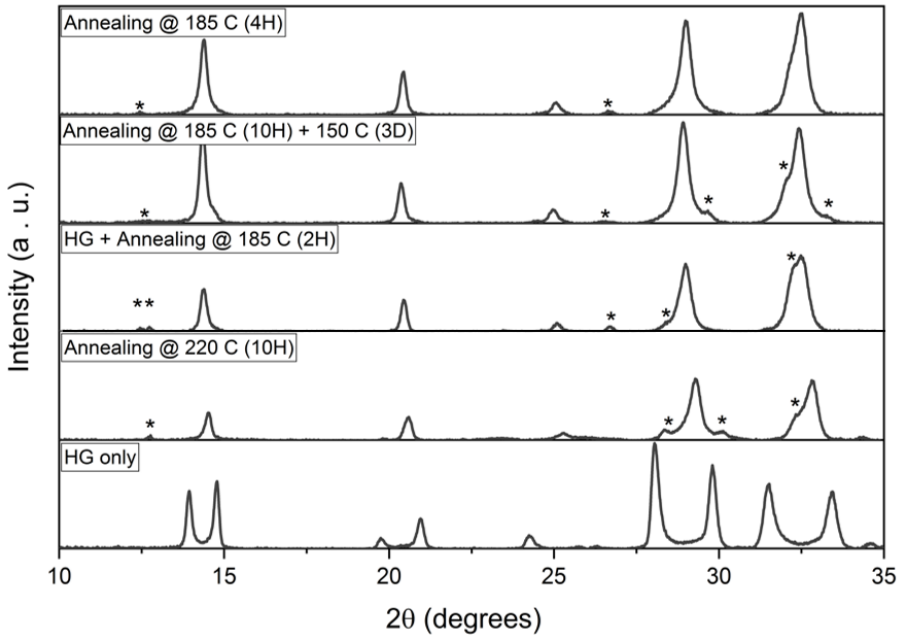

Figure B.25: Powder XRD spectra for various attempts to prepare $FAPb(Br_{0.5}I_{0.5})_3$ by HG and solid-state synthesis at elevated temperatures. Asterisks indicate peaks for either decomposition products, such as PbI_2 or for phases other than $FAPb(Br_{0.5}I_{0.5})_3$.